FEASIBILITY STUDY OF A PULSED SOLENOID FOR BNL-E951 TARGETRY PROGRAM

K. McDonald[a], J. Minervini[b], R. Titus[b], R. Fernow[c], J. Gallardo[c],
M. Iarocci[c], S Kahn[c], H. Kirk[c], I. Marneris[c], R. Samulyak[c],
N. Simos[c], P. Thieberger[c], R. Weggel[c],
[a]Princeton University, Princeton, NJ 08544
[b]MIT, Cambridge, MA 02139
[c]BNL, Upton, NY 11973

April 19, 2002

Contents

fact
Muon Collaboration

List of Figures

fact
Muon Collaboration

List of Tables

Chapter 1

Executive Summary

1.1 Acknowledgment

fact
Muon Collaboration

Chapter 2

Introduction and Overview

fact
Muon Collaboration

Chapter 3

Previous Experiments

3.1 Target Studies

3.1.1 Introduction

A successful Muon Collider or Neutrino Factory based on a muon storage ring requires the production of copious pions which are then conducted into a decay channel where the muon decay products are collected.

Current scenarios require intense protons beams, suitable target material and a high-field solenoidal field which surrounds the target. Modeling studies point to high-Z materials being more efficient at producing pions of both signs, whereas low-Z materials are better in avoiding the absorption of the produced pions. Carbon has the advantage of permitting larger target cross-sections and therefore larger beam spot sizes with a corresponding decrease in shock heating due to high peak energy depositions.

The Muon Collider Collaboration is considering another approach, however, which is to retain the pion production advantage from high-Z materials by utilizing a free liquid mercury jet. In this case, the jet can be conveniently replaced so that target integrity after exposure to the proton beam is not an issue. However, the dynamics of a mercury jet moving in a high-field solenoid field followed by its dispersion after the interaction with the intense proton beam, remains to be studied.

For this reason, E951 [1] has been proposed and approved for running at the Brookhaven Alternating Gradient Synchrotron (AGS).

3.1.2 Experimental layout

The A3 beam line [2] (See Fig. 3.1) in the experimental hall has been configured for the transport of primary 24 GeV protons extracted from the AGS. All targets have been mounted inside a stainless steel vessel which prevents the potential dispersal of activated fragments which could be ejected from the tested target. This target system is placed on a translation table (Fig. 3.2) which has a target flag mounted to one side to facilitate the tuning of the proton beam prior to the target being moved into position.

Beam spot sizes were subsequently measured by placing unexposed film emulsion on beam windows which were placed interior to one of the secondary containment vessel in order to test the integrity of the beam windows before the subsequent exposure of our targets. Measured beam rms spot sizes are σ_x= 1.0 mm and σ_y= 0.3 mm (See Fig. 3.3).

A3 Beamline End Station

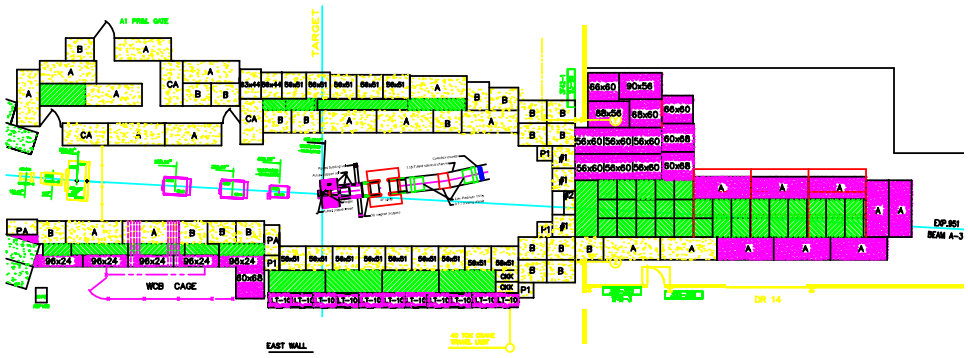

Figure 3.1: The AGS A3 beam line

Beam intensities were monitored by a series of beam transformers extending from the AGS extraction point to immediately preceding the target table. Intensities were adjustable from 0.5 to 4.0 $\times 10^{12}$ protons/pulse with full bunch beam lengths typically 150 ns.

The dispersal of the mercury was recorded with the use of two independent camera systems: 1) an Olympus Industrial, Encore PCI 8000S camera system capable of recording at a rate of 4 kHz with shutter settings for each frame set to 25 μs; and 2) an SMD 64K1M camera capable of taking 16 frames at speeds of up to 1 MHz. The exposure time for the latter camera is 150 ns per frame.

Strain measurements were based on miniaturized Fabry-Perot interferometers provided by Fiso Technologies. Signals from the interferometers were then processed through a Veloce multi-channel system.

3.1.3 Carbon Targets

Two forms of solid carbon rods were exposed to the primary proton beam: 1) two ATJ carbon rods each 30 cm long by 16 mm diameter; and 2) two 12 cm long by 16 mm diameter rods made from an anisotropic carbon-carbon composite.

The carbon composite is particularly interesting because its elastic modulus is unusually high while its coefficient of thermal expansion is nearly zero

Layout of the Target Station

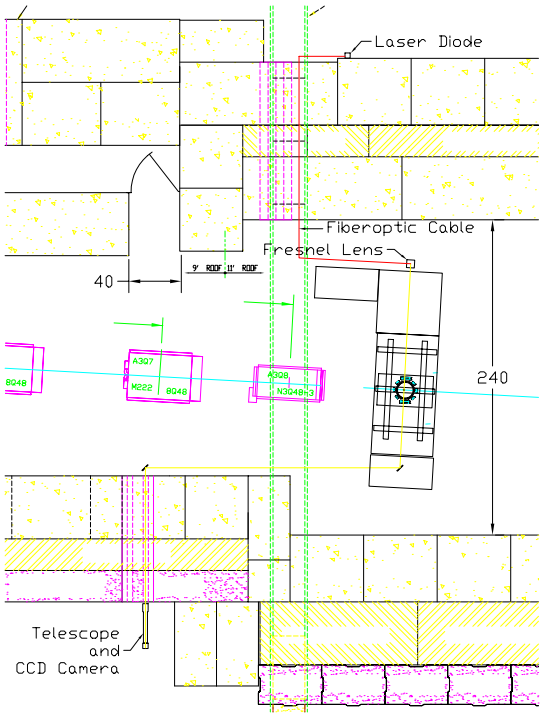

Figure 3.2: The A3 beam line target station

over a large temperature range. See Table 3.1 for the relevant properties.

In Fig. 3.4, results of two strain measurements for both materials are

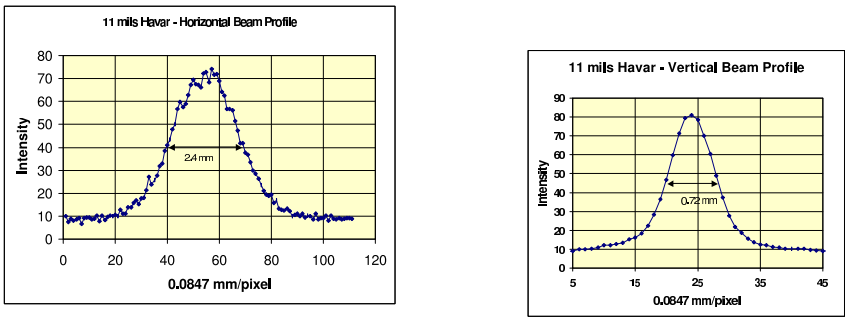

Figure 3.3: The A3 beam spot size projections

shown. From the ATJ strain waveform we see clear evidence of a 100 kHz signal superimposed on a 4.5 kHz signal which has an initial peak-to-peak amplitude of 30 μstrains. Also clearly seen, before the arrival of the proton pulse, is the background noise level of the strain gauge which is σ_{rms}= 0.7 μstrains. The 4.5 kHz signal corresponds well to the expected longitudinal propagation of reflected pressure waves. The 100 kHz signal is appropriate for radial reflections. For the carbon-carbon composite we observe a 34 kHz signal but with a much lower amplitude. This signal's initial peak-to-peak level is 3 μstrains while the background noise level for this strain gauge is σ_{rms}= 0.3 μstrains.

3.1.4 Mercury Targets

Two separate mercury targets were exposed to the AGS proton beam. An initial test was made with a passive system in which a small well loaded with 1.9 cm^3 of mercury was placed into a container in which the dispersed mercury droplets could be collected and channeled back into the well. Five shots

fact
Muon Collaboration

Table 3.1: Properties of carbon targets

	ATJ	Carbon-Carbon Composite	
		Z	(U,V)
Elastic Modulus (GPa)	9.6	117	48
Exp. coefficient (1/°C)	2.46×10^{-6}	∼0	∼0

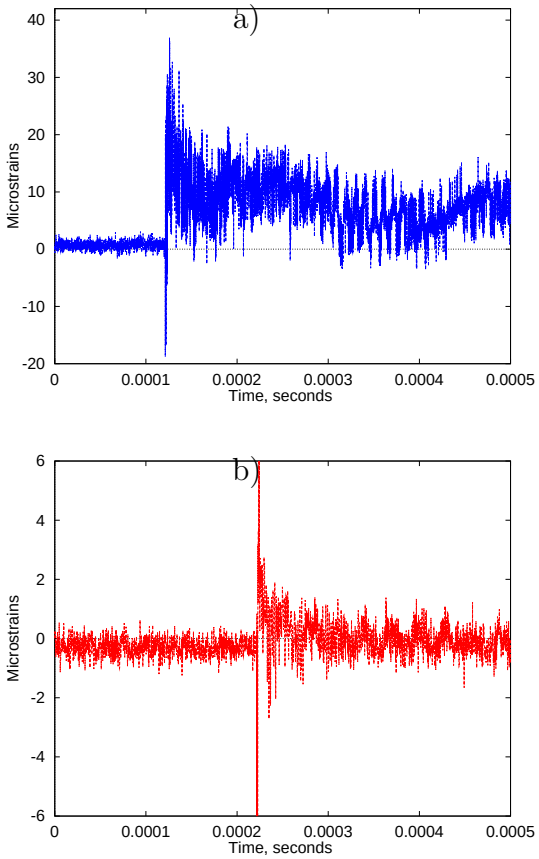

Figure 3.4: Strain gauge data from carbon targets: a) 3×10^{12} proton beam on ATJ carbon; b) 2×10^{12} proton beam on carbon-carbon composite

were delivered and the mercury dispersion recorded. The beam intensity for

these shots varied from 0.65 to 4 $\times 10^{12}$. In Fig. 3.5 we see three frames taken with the SMD 16K1M camera. The initial velocity of the ejected mercury was 70 m/s, however, this velocity was reduced to 40 m/s by the time the cloud of mercury has traveled 4 cm. This effect could be due to the presence of 1 atmosphere of air inside the chamber.

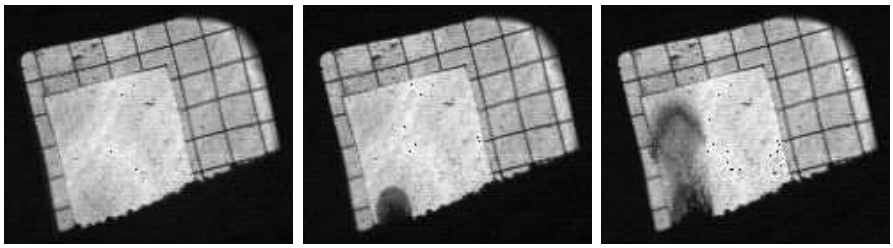

a) b) c)

Figure 3.5: Hg interaction with 24 GeV, 4×10^{12} protons; $t =$ a) 0 μs; b) 300 μs; c) 800 μs. The grid is 1 cm x 1 cm.

The mercury jet (Fig. 3.6) was formed by supplying a pneumatic pressure of 26 psi which forced the mercury out of a 1 cm diameter nozzle inclined at 18.5°. The resulting mercury stream travels 20 cm to its maximum height at which point the trajectory of the Hg jet overlaps with the proton beam for 19 cm. The average velocity of the jet was 2.5 m/s. The diameter of the jet at the interaction point fluctuated between 0.7 and 1.7 cm.

Dispersal of the mercury by energy deposition due to the interacting proton beam was observed directly by viewing prominences as they left the bulk of the mercury jet. We were also able to indirectly measure the velocity of Hg droplets, since their arrival at the quartz viewing ports was signaled by distinctive splashes. Directly measured bulk velocities range from 5 to 50 m/s while the velocities of the Hg droplets arriving at the quartz window varied from 1 to 10 m/s. In both cases we observe that the maximum velocities increase roughly proportionally to the intensity of the impinging proton beam.

Also of interest is the extent of the disruption of the mercury, and in particular whether this disruption extends forward and backward from the interaction region. It was observed that the region of disruption was confined largely to the volume of overlap with the proton beam with no evidence of jet dispersal propagating back to the nozzle. The maximum disruption length

observed was 14 cm.

Finally, by utilizing the SMD 64K1M camera set in a fast frame mode (1 frame/10 μs), we observed that the breakup of the mercury jet commenced after an elapsed time of $\sim$40 μs. Observations with the camera set as fast as 18 frames per 18 μs showed no discernible disruptive motion in the jet.

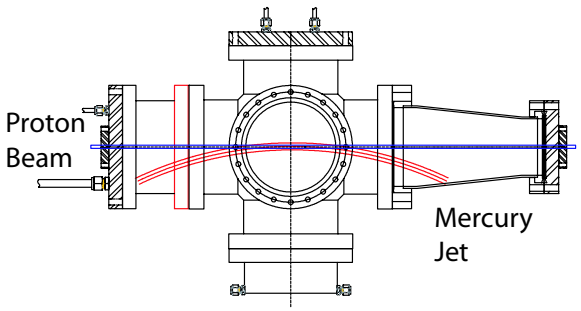

Figure 3.6: Elevation view of the Hg jet overlapping with the 24 GeV proton beam.

3.1.5 Summary

The E951 collaboration has begun a series of measurements with the goal of providing observations needed to clarify the best technological path for the Neutrino Factory and Muon Collider Collaboration to proceed in order to provide a future machine with a source of muons more intense than presently achievable.

Among the initial results:

- The strain amplitudes for a cylinder made from an anisotropic carbon-carbon composite are substantially less (a factor of $\sim$10) than those for ATJ carbon.
- Hg jet dispersal is mostly transversal. The jet disruption is confined mostly to the proton beam-Hg jet interception volume.
- For a 4×10^{12} proton beam, dispersed Hg droplet velocities are $<$ 10 m/s.
- Hg jet dispersal is delayed for $\sim$40 μs.

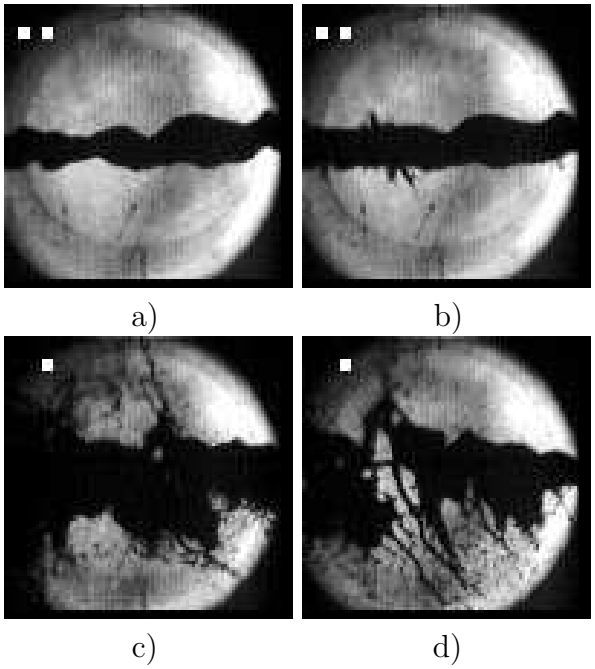

Figure 3.7: Hg jet interaction with 24 GeV 3.8×10^{12} protons; $t =$ a) 0 ms; b) 0.75 ms; c) 10 ms; d) 18 ms

Goals for subsequent runs include increasing the single pulse proton beam intensity to the level of 16×10^{12} (16 TP) and the addition of an high-field solenoidal field surrounding the target in order to ascertain the influence of the magnetic field on the incident Hg jet and the subsequent dispersal of the mercury.

Bibliography

[1] James Alessi, et al., *An R&D Program for Targetry and Capture at a Muon-Collider Source*, Proposal submitted to Brookhaven National Laboratory, (Sept. 28, 1998).

[2] K. Brown, *First Beam Tests of the Muon Collider Target Test Beam Line at the AGS*, Proceedings of the 2001 Particle Accelerator Conference, Chicago, IL, June 18-22, 2001.

3.2 E951 R and D Effort

3.2.1 Introduction

A muon collider/neutrino factory based on a muon storage ring requires a tightly focused, high intensity beam on target. Specifically, up to 16 TP per pulse of a 24 GeV proton beam need to be delivered on a target. While a mercury jet is the primary target consideration (high-Z material and more efficient in producing pions of both signs), other options using graphite as target material (low-Z and better in avoiding the absorption of produced pions) are also being explored. The broad goal of E951 is to provide a facility that can test all the major components of a liquid or solid targets in intense proton pulses and in a high field solenoid.

The first phase of E951 has focused on the interaction of intense proton pulses with targets and beam windows in zero magnetic field. A series of different experiments were designed and conducted in an effort to understand and evaluate a variety of issues that ranged from target material response to tightly focused proton beams, to estimates of mercury dispersion velocities. Specifically, the experimental matrix included:

(a) the study of window materials

(b) the evaluation of graphite and carbon-carbon composite as alternative low-Z target materials

(c) the behavior of a mercury pool intercepting the proton beam and the correlation of the energy deposited to ejection velocities

(d) the interaction of the proton beam with a mercury jet and the subsequent destruction of the jet including measurements of velocities of material dispersion.

Figure 3.8 depicts the layout of the A3 beam line near the target station that has been configured for the transport of primary 24 GeV protons extracted from the AGS. All targets are mounted inside a stainless steel vessel preventing any dispersal of activated fragments that can potentially be ejected from the tested target. The details of each arrangement will be presented in later sections. Figure 3.9 represents the measured beam spot size in the two planes at the end of the A3 line that may be achieved through fine-tuning of the various quadrupoles.

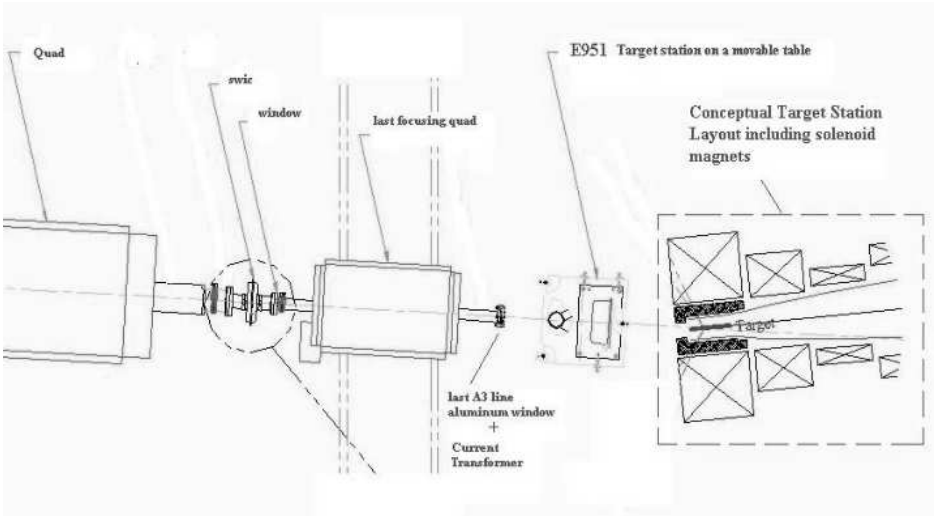

Figure 3.8: Comparison of measured strains between a 100 KHz and a 500 KHz processed strain signal in the vicinity of the arrival of the initial shock wave at mid-radius of the aluminum window

Window Study

The window material study focuses on the thermo-mechanical response of the selected materials and their ability to survive the tightly focused beam for multiple pulses. Based on the required muon collider beam parameters, it was concluded early on that very few materials will be able to survive the thermal shock induced by even a single pulse, let alone multiple pulses. While in the actual muon collider target configuration the beam window location may be optimized (achieve bigger beam spot based on the beam beta function), in the E951 experiment it is required for the beam window to be close to the target. In order to select the right window material that will survive under such conditions, an extensive effort was undertaken to evaluate different materials that show promise based on their mechanical strength.

The window study was two-fold. It included the prediction phase and the experimental verification. In the prediction phase, the energy deposition on the different window materials and for the anticipated AGS beam parameters were estimated using the hadron interaction code MARS [1]. This was followed by a transient thermal analysis resulting from the deposited energy

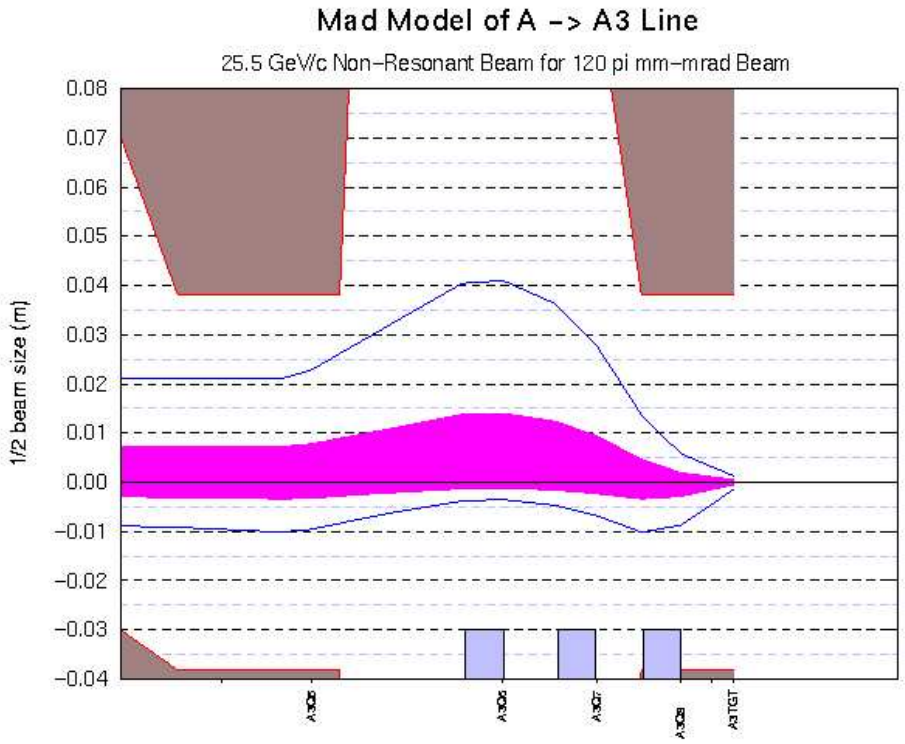

Figure 3.9: Strain measured in aluminum window in back-to-back pulses of similar intensity

and finally by a thermal stress analysis that included the generation and propagation of stress waves. The thermal response of the window structure and the subsequent stress wave generation and propagation were computed using the finite element code ANSYS [2]. In the experimental verification, the recorded transient strain in the actual windows was compared to the predicted strain levels and wave shapes. The primary goal in such comparison was to verify that the prediction at this lower intensity level is "trustworthy" and can safely be used to extrapolate to the higher intensities required and address the material failure potential. Additionally, and as part of the experimental verification study, the impact of irradiation on the mechanical/strength properties of the selected materials is examined closely. The latter is an on-going effort.

Carbon Targets

The experimental effort on low-Z solid targets included the study of ATJ graphite and carbon-carbon composite by exposing them to the tightly focused 24 GeV AGS beam. The primary goals of this task was to (a) assess the survivability of the graphite target to the anticipated high intensity beam, and (b) to experimentally verify the promise of the carbon-carbon composite of having a very small thermal expansion coefficient that, in turn, implies small generated stress waves. Verification of the latter will be significant in that a beam power of the order of 1 MW could be envisioned using such target.

CERN Mercury Trough Target

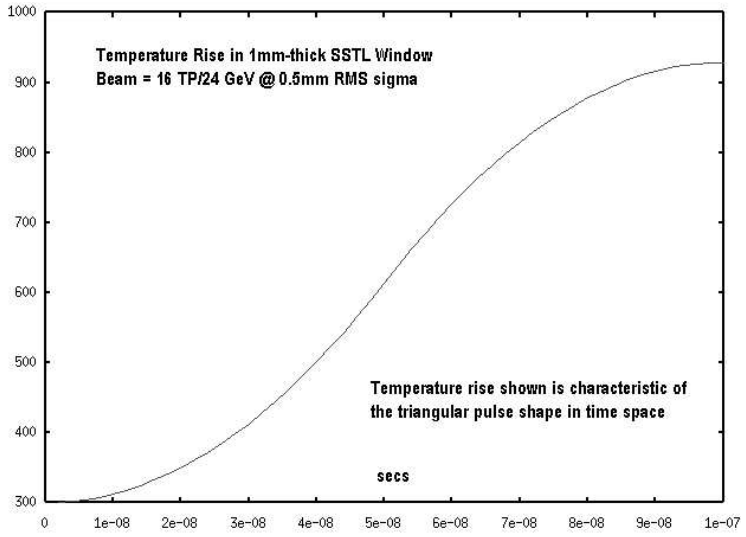

Figure 3.10: Cross Correlation of signals in different gauges of the same window to assess the position of the pulse relative to the gauges based on the lag time of stress pulse arrival

Part of the experimental matrix of E951 was the CERN mercury target configuration. This passive target arrangement, shown in Fig. 3.10, consisted of a pool of mercury in a well engraved into a stainless steel block. The target

is inside a special container that allowed for the anticipated dispersed mercury to collect back into the well while permitting the capturing of the event by fast cameras through a side viewing window. The primary goal of this passive mercury target experiment was to measure with the fast cameras the velocity of the mercury ejected from the free surface of the pool and correlate it with the analytical predictions. Peak ejection velocities of 70 m/s were observed during the experiment generally following the theoretical predictions. Such low velocity values, compared to the velocities that pressure waves in the mercury propagate with, confirm that the potential for destruction of the target enclosure by the mercury projectiles is nonexistent.

3.2.2 Mercury Jet Target

The active mercury target of E951 consisted of a mercury jet intercepting the AGS proton beam as shown in Fig. 3.11. In this first phase of the experiment, no magnetic solenoid field was integrated with the experiment.

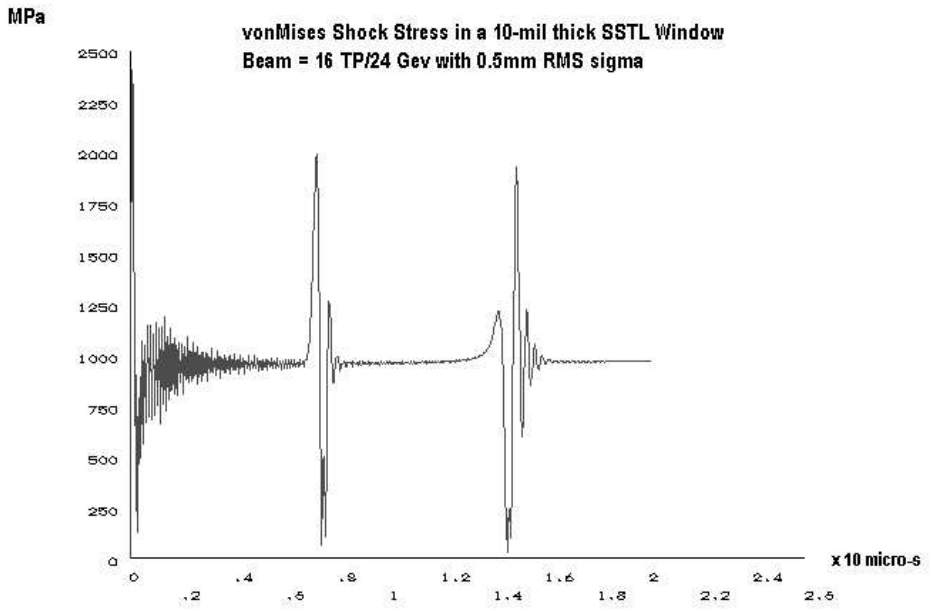

Figure 3.11: Recorded strain in 1mm Inconel window

The potential use of a mercury jet target for the muon collider/neutrino factory has raised several novel issues that needed clarification through experimental means. These include dispersion of the jet due to rapid energy deposition, destruction of the jet by magnetic forces, and ejection of high velocity droplets that can damage the confining envelope. The latter was also addressed in the CERN mercury target configuration. Additionally, a potentially challenging design issue associated with the target configuration is the possibility of shock wave impact and consequently potential damage on the jet nozzle that sends the jet into the solenoid. To address this design issue an attempt was made to record the dynamic strains in the vicinity of the nozzle. The appearance of strain waves, following the beam/jet interaction, will signal the arrival of pressure waves at the nozzle location.

E951 verified that the indeed the jet will destruct by interacting with a single proton pulse that has even much lower intensity than the 16 TP anticipated in the actual muon collider/neutrino factory. The good news is that the destruction process, as predicted by calculations, was proven to be slower than the pressure waves generated in the jet and that the dispersed mercury ejects with velocities that are a fraction of the sound speed in mercury.

Preliminary assessment of pressure wave travel back to the nozzle shows that, while small given the much lower intensity achieved during E951, there is evidence of such travel back toward the nozzle. It is difficult, however, based on these findings, to extrapolate to the actual target and assess the susceptibility of the nozzle to repeated loading from these waves.

3.2.3 E951 Beam Window Study

Issues

Given the set of beam parameters required for the muon collider/neutrino factory, i.e. 16 TP intensity and 0.5mm rms sigma radius, the resulting energy density within the one sigma radius of the beam will induce a stress field that for many materials will exceed the yield strength limit.

Figure 3.11 is a clear example of that. It depicts peak thermal stresses in a 10-mil thick stainless steel window induced by a beam with such parameters (24 GeV, 16 TP, 0.5 mm sigma and 100 ns pulse length). Specifically, the peak von Mises stresses in the window material, occurring at beam center and mid-thickness, approaches 2500 MPa that is more that twice the yield and ultimate strength of the material.

Since such severe conditions will result after a single proton pulse for some materials and after several pulses for the better materials, depending on the spacing between the pulses in the train, it is very important to obtain a better understanding of the way these materials respond to such severe exposure, and of the way their properties degrade with radiation exposure. The latter needs to be combined with fatigue failure properties to establish the criteria for the amount of "beating" a good window material can take before it reaches its failure limits. Thus, the beam window issues that E951 was set to address may be summarized in the following:

1. Survivability of windows based on a single beam pulse
2. Survivability of windows to a series of pulses
3. Assessment of the effects of irradiation on the mechanical properties of the candidate materials

Detailed dynamic analysis that capture the window structure response helped guide the selection of materials to be tested. These analysis also provided the basis needed for quantitative comparison with the experimental results. Confidence in the methodology used to make the predictions will allow for the extrapolation of the data to conditions required in the real muon collider target. These conditions were not anticipated to be achieved in the first phase of E951, simultaneously at least. The material matrix that was finally selected included a 10-mil thick 3000 series aluminum window, a 9-mil thick titanium alloy, an 11-mil thick havar, and two inconel-718 alloy windows in two thicknesses (1 mm and 6 mm).

3.2.4 Goals of Experimental Effort

The goals of the first phase of the window experiment effort are summarized below:

1. Verification of the predictions to form the basis for extrapolation of results for the more intense beam as well as the design of the "real thing"
2. "Real" environment exposure of the selected materials as window structures and understanding of their response based on measurable quantities that can be directly connected to the failure mechanism, i.e. stress and strain

3. Assessment of "thin" vs. "thick" in windows. Given that the ability of a beam window structure to "diffuse" an undiluted beam is a function of a number of parameters (sound velocity, beam structure and thickness), the controllable parameter of thickness and its effect is addressed in the experiment

4. Address "failure" in the window material. Given that failure means different things to different people, the goals of E951 were to (a) qualitatively assess the potential that the window materials failed by monitoring the breach of vacuum in the enclosed space of a double window arrangement, and (b) to examine the affected zone window that intercepted the beam for possible degradation of its overall mechanical properties or changes in the micro-structure.

3.3 Theoretical Predictions on Beam Window Response – Background

Consider a thin window structure of radius **R** and thickness **h** intercepting an energetic, focused proton beam of Gaussian profile. Energy is deposited in the material with radial symmetry about the window center while some variation of energy deposited is expected to be present, no matter how thin the window, through the thickness h.

Figure 3.12: Predicted strain in 1mm Inconel window

In evaluating the thermoelastic equation of motion in the beam window it is assumed that the thermal expansivity is isotropic and the effects of heat conduction on the dynamics are neglected. Further, as first approximation, no attenuation of the acoustic pulse is accounted for even though some fraction of the energy is dissipated in the material. It is also assumed throughout that the energy deposited in the window material is immediately converted to thermal energy. As noted in [6] this is a very good approximation given that the acoustic relaxation time is of the order of nsec whereas "thermalization" times, at least in metals are of the order of 10^{-11} s.

Based on the above considerations, the issue to address is how does a thin window structure respond as it intercepts a fast and intense proton pulse. While "thermalization" is assumed to take place instantly, thus generating a

fact
Muon Collaboration

quasi-static state of stress in the affected zone, the acoustic relaxation time still plays a role in defining both the generation and the level of thermal shock stresses. Specifically, the amplitude of the stress waves emanating from the "heated" zone depends on the relation between the rate of energy deposition (pulse length) and the acoustic relaxation time (time required for an acoustic wave to traverse the region of energy deposition). If the time of energy deposition is smaller than the acoustic relaxation, the amplitude of the stress wave will be maximum. If acoustic relaxation is smaller then the amplitude will be reduced by the ratio of the two characteristic times.

While the above considerations define the response of the thin window in the radial sense of stress wave generation and propagation, the most important consideration in assessing its survivability is the thermoelastic response through the window thickness. As the affected zone is thermalized in the cylindrical volume between the two surfaces, stress waves initiate at each of the surfaces and travel toward the opposite surface. The governing principle is basically a 1-D response similar to the response of a heated 1-D rod with free edges. Figure [] graphically demonstrates the response of the heated zone by capturing the propagation and reflection of elastic waves through the thickness and out of the zone in a series of snap shots. Since energy is moving out of the region in the radial direction, the amplitude of the stress "ringing" through the thickness reduces in time. The impact on the window material, however, could dramatic since a significant number of stress cycles of considerable amplitude can accumulate following a proton pulse.

To demonstrate the severity of the beam-window interaction under such tight focusing, the thermal stress induced in a 10-mil thick stainless steel window by the beam of the required parameters (24 GeV, 16 TP, 0.5 mm sigma and 100 ns pulse length) is shown in Fig. 3.13. Specifically, the peak von Mises stresses in the window material, occurring at beam center and mid-thickness, approaches 2500 MPa that is more that twice the yield and ultimate strength of the material. According to this prediction such window will not be able to survive a single pulse let alone multiple pulses. Figure 3.10 shows the temperature rise in the stainless steel window as a result of a single pulse.

Also depicted in Figure 3.10 is the "ringing" regime that follows the energy deposition. The peak von Mises stress occurs within the window thickness some time between the initiation of the pulse and the time required for the sound to traverse the thickness for the first time.

Initial estimates of energy deposition in various materials for a 24 GeV

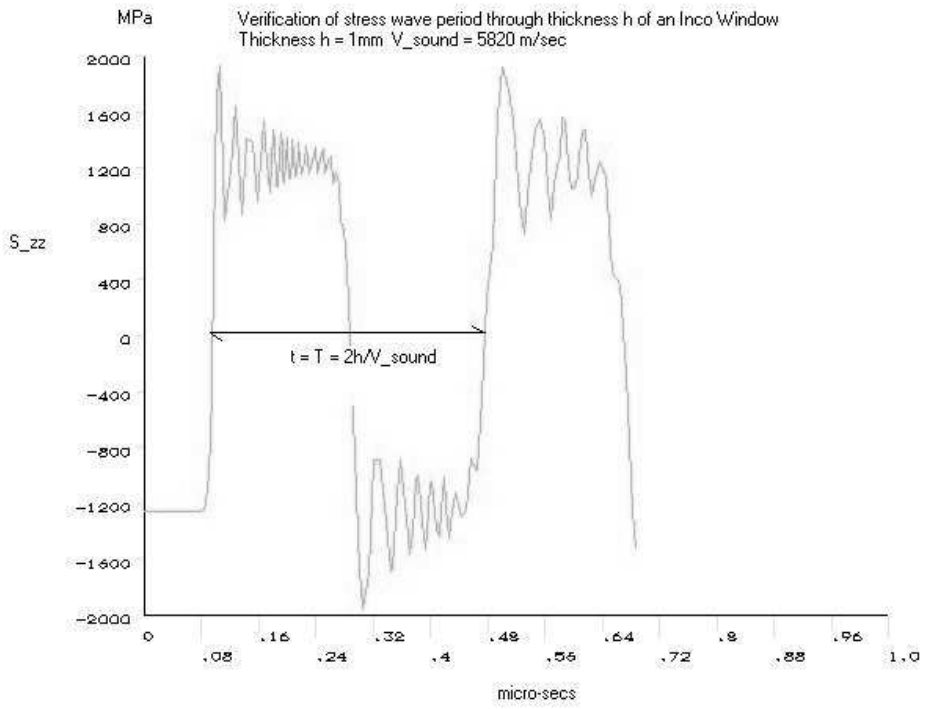

Figure 3.13: Recorded strain in a 6-mm Inconel window by two strain gauges 180 deg apart. Also shown is the recorded signal by the 100 KHz bandwidth.

proton beam, 16 TP intensity, a beam spot down to 0.5 mm rms and a pulse length of approximately 100 ns painted a very bleak picture for most commonly used materials for beam windows. An additional concern in bringing beam on the AGS A3 line was the ability of existing aluminum windows to survive even though there were expected to see a larger spot (based on the beta function of the beam). Given the severity of the problem, an experimental set-up to study the response of window materials as part of the E951 muon targetry experiment was introduced. Four (4) different window materials were selected for testing in the beam line at AGS. Three of the materials, Inconel-718, Havar and Titanium alloy, showed promise of surviving the proton beam pulses. Their selection was based on material properties and extensive thermal shock predictions. Figure 3.14 shows von Mises stresses generated in a titanium alloy (6 Al–6 V). Under the required parameters of

24 GeV, 16 TP intensity and 0.5 mm rms spot, the stresses are below yield, thus making it a favorable candidate. Figure 3.15 presents similar results in a Havar window and shows that under such beam parameters the peak stresses are approaching the yield stress limit.

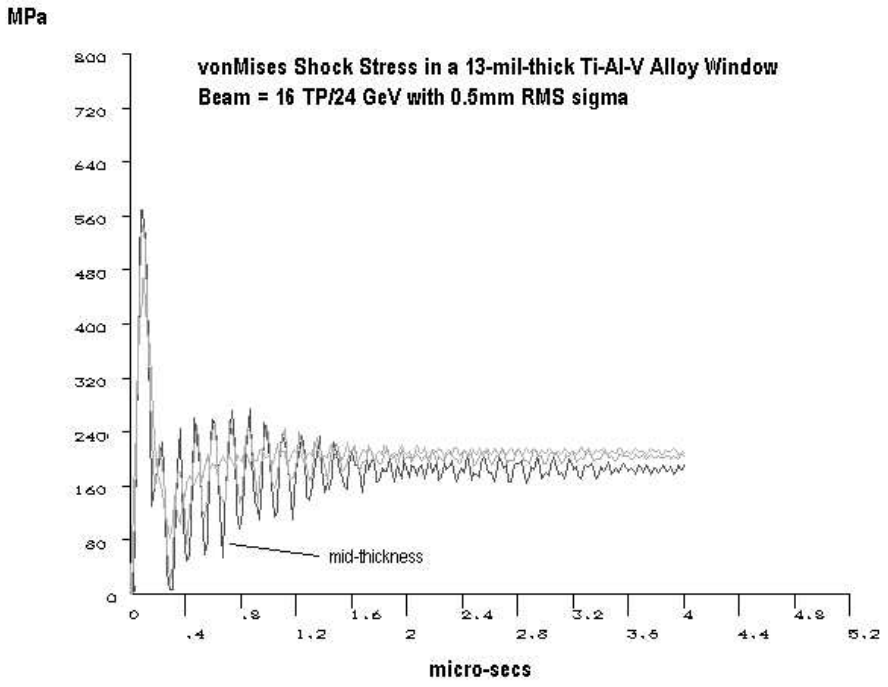

Figure 3.14: Predicted strains in the 6mm-thick Inconel window

Figure 3.15: Recorded strains in back-to-back pulses in a 11mil-thick Havar window

The fourth material selected is Aluminum (3000-Series). Based on the theoretical predictions, this window material could fail even if 6 TP are delivered on target. Given that at initial stages of E951 6 TP beam is more likely to be delivered and because of the proximity of this window material to the failure condition, experimental data associated with this material and its potential failure, would be very useful in benchmarking failure prediction.

Since the calculations show that the window thickness, in conjunction with the material acoustic velocity and the pulse structure and duration, has a dramatic effect on the peak stresses generated in the material, two (2) thicknesses (1-mm and 6-mm) of the Inconel-718 material were selected for study.

3.4 E951 Experiment

Figure 3.16: AGS A3 Line layout at E951 target station

Figure [] depicts the layout of the window test experiment. There are two parallel beam lines within the target enclosure. It all rests on a moving table such that both lines can be exposed to the proton beam. Shown in Figure [] and in one of the lines is a set of double windows with vacuum in the space between the two plates. Each window is made of one of the selected experiment materials. The main goal is to make a qualitative assessment of window failure when it intercepts the proton beam. In other words, any loss of vacuum, which is continuously monitored, in the space between the double windows will indicate mechanical failure.

Along the second beam line a set of single windows instrumented with fiber-optic strain gauges are placed.

Window Strain Measurement Set-Up

The goal of the strain experiment is to capture the radial strain at a specified distance from the beam spot location. While the governing shock stress in determining the safety of the window material is the von Mises stress at the center of the spot and through the material thickness, there is no measurable quantity in that orientation. However, by predicting the radial strain at a safe distance from the beam (minimize the radiation damage on the strain gauges), the whole stress tensor can be estimated. Figure [] depicts the arrangement of four (4) fiber-optic strain gauges that were placed on the front surface of each of the tested windows. The strain gauges are designed around an interferometer by FISO Technologies Inc. The basic active element (cavity) consists of two mirrors facing each other. The acquired signal goes

through custom-made filtering and at the end of the process a 500 KHz strain signal is deduced.

The wavelength of the shock front (uncorrupted in nature) and the ability of recording system to capture it is vital to the analysis of strain amplitude and time structure.

Window Strain Measurements: Comparison

During the window tests of the E951 experiment a beam intensity of approximately 2.5 TP was delivered on target. The beam spot size (originally estimated at 1 mm rms sigma radius), and which closely fits an ellipse rather than the circle that was assumed in the theoretical predictions thus far, is currently being re-evaluated using radiation exposure techniques.

While the combination of beam intensity and spot was far from being critical for any of the windows, strain measurements that can be used to verify the predictions have been generated. Shown in Figure [] is the radial strain in one of the four gauges of the 10-mil aluminum window. The very first part of the record is the noise in the fiber-optic system. The arrival of the proton beam is indicated by the high frequency noise corruption of the signal. The arrival of the compressive wave at the active element of the gauge (approximately at 0.5-inch from center) is shown by the first dip. What follows is the arrival of the tensile wave phase at precisely the time that is expected.

Following the rapid thermalization of the affected material (within the beam spot) two waves are generated at the edge of the heated zone. One travels outward as a compressive wave and arrives at the strain gauge first (dip). The second wave travels toward the center of the beam spot as compressive, reflects at the center by changing sign, and travels outward as a tensile wave.

The remaining cycles represent reflections at the edge of the window and its center.

Figure [] depicts the calculated strains for the same beam parameters but with a "true" round Gaussian profile. The agreement between experiment and theory is very good both in terms of amplitude and time structure.

Figure [] depicts the recorded strain of the same gauge as seen from two bandwidths of the acquisition system. The stain record shows the arrival of the initial shock wave and some reflections of the pulse between the edge and the center of the window disk. Based on the AGS pulse structure, spot size

and pulse length, it was assessed that the 100 KHz bandwidth was insufficient to record the stress pulse arrival at the strain gauge location. Indeed, Figure [] clearly demonstrates that no signal was recorded by the acquisition system operating at this bandwidth. Not shown here is the complete record (up to 0.1 sec) which shows that overall response of the window dominated by lower frequencies is captured by both bandwidths.

Figure [] shows the strain measurements at the same gauge in two back-to-back pulses with approximately the same beam intensity. The duplication of the response is a sign of stability in the measurements. However, it should be noted that fiber-optic strain signal is very sensitive to the beam arrival and the ensuing flux of photons (shown as high frequency bunch at the start of the record and sharp peaks in the transient response). A filtering effort is under way to "clean" the records from the inherent and induced noise.

An additional source of discrepancy is the actual position of the beam with regard to the four gauges. A beam shift toward one of them will alter the strain measurements by inducing higher strains in the closest gauge. To estimate the "true" position of the beam, a cross-correlation process (typical results shown in Figure []) of the gauge signals has been introduced that, in first order, indicates the relative arrival of the signal.

In Figures [] & [] the measured and predicted strains in the 1mm-thick Inconel–718 window are shown. It should be noted that based on the "preliminary" analysis and comparison of experimental to theoretical results, it has been observed that the thicker the window gets the higher the deviation between the two.

In Figure [] the strain recorded in the 6mm-thick window are shown. As expected, the "thickness" effect becomes more prominent in that there is presence of surface waves that have been enabled to form and propagate as well as delayed reflections from the opposite surfaces. Figure [] depicts the theoretical predictions in the same window but with a Gaussian spot at the center of the window. It is evident that general characteristics of the response are predicted quite well. Lastly, in Figure [] the recorded strains from back-to-back pulses are shown for the thin Havar window demonstrating the stability of the acquisition system.

3.4.1 Summary–Beam Window Study

The first phase of the window study of experiment E951 provided the opportunity to test, in addition to targets, window structures that are integral

part of any target system and normally experience similar shock conditions. Despite the fact that the pulse intensity that was delivered to the windows was much lower than was hoped for, still important conclusions could be drawn. Specifically, from the overall experimental/theoretical study thus far the following is assessed:

1. Predictions are generally in agreement with the results of the actual experiment. This implies that the energy deposition estimated by the neutronic code calculations agrees with the energy left in the material by the beam. It should be noted that in this first phase of data post-processing and comparison, influential material properties such as damping have been accounted for in the theoretical predictions. Subsequent analysis with energy dissipation considerations would help the agreement both in terms of amplitude and pulse shape and dispersion even further. In addition, as noted earlier, a re-evaluation of the actual beam spot is under way which is expected to provide a picture closest to the "real thing". In light of this information, the theoretical model used to calculate the predictions will be modified accordingly and the predicted strains will also be re-evaluated.

2. Because of the lower than anticipated intensity and possibly larger beam spot, the failure conditions for the weakest window (aluminum) were never approached.

3. The thicker the window, the more difficult to predict amplitudes and structure of the signal due to multiple wave phases and reflection. A key piece of information, however, that was deduced is that higher levels of strain were observed in the thicker window.

4. Given the nature of shock waves in the materials, a further increase in the measuring system bandwidth is desirable.

3.4.2 Proposed New Studies

To shed more light in this critical aspect of window material selection and its long-term survival in the proposed muon collider target space, it is important that the experimental studies continue. Specifically, in the next experimental phase the following should be considered:

1. Close examination of the exposed windows and especially of the directly affected area for possible micro-structural failure

2. Properties of materials having the most promise of long-term survival should be evaluated from the point of view of radiation exposure and degradation

3. Expose the windows already tested to proton pulses with higher intensity. Reaching intensities that will cause mechanical failure in the "weakest" window and calibrating the prediction model to that condition, will provide a very important tool to be used in predicting failure for other materials that will be considered in the muon collider/neutrino factory target system.

3.4.3 E951 Mercury Jet Target Study

3.4.4 Background–Issues/Goals

The use of a mercury jet target raises a number of issues that need considerable attention. These issues are associated with the presence of a strong magnetic field, the rapid heating of the mercury by the proton beam and the subsequent dispersion. As the mercury jet enters the field eddy currents are induced in the jet and the Lorentz force on these currents could lead to the distortion of the jet. An important point to be made is the generated magnetic pressure on the mercury jet that, in turn, is expected to damp mechanical perturbations and also add inward radial pressure. Figure [] is an overall schematic of the target space including the solenoid.

Preliminary estimates have shown that the mercury jet will disperse after it interacts with a single proton pulse. What is key, however, is estimating the time scale of jet destruction. For one scenario in particular that requires six (6) 2-ns micro-pulses to be delivered within 2μs, the time of destruction is important given that one needs to have all six micro-pulses see an intact jet. A consequence of the jet's dispersion is the ejection of droplets that, if ejected at very high velocities, can cause serious damage to the target space.

As noted earlier, a concern related to the survivability of the jet nozzle experiencing a pressure wave traveling upstream potentially exists. For a continuous jet with the interaction zone starting at some distance downstream of the nozzle, pressure waves are expected to travel through the undisturbed

jet and reach the nozzle. While pressure amplitudes are expected to attenuate by the time the front reaches the nozzle, the many cycles over the life of the target enclosure could lead to nozzle fatigue failure. Within the scope of E951 experiment, an attempt was made to address the issue and preliminary experimental results are shown.

For all scenarios of beam delivery, the energy deposited in the mercury jet has been calculated using the MARS code. In the co-linear interaction scenario of proton beam and jet, peak energies of approximately 130 Joules/gm have been estimated. This peak energy is observed about 5 cm into the jet from the start of the interaction region. In the latest scheme, however, with the mercury jet tilted by 100 mrad and the proton beam by 67 mrad the peak energy deposition is approximately 49 Joules/g and it occurs about 25 cm downstream from the start of the interaction region. Table 3.2, lists some of the physical properties of mercury that were used in the various estimations

Table 3.2: Physical Properties of Mercury

Density, ρ	13.5 g/cm^3
Compressibility, κ	0.4510^{-10} m^2/N
Volumetric Thermal expansion, α_v	18.110^{-5} K^{-1}
Specific Heat, c_v	140 J/Kg K
Velocity of Sound	1300 m/s
Critical Point Temperature, T_{cr}	1593^o C
Critical Point Pressure, P_{cr}	185 MPa

Predictions of Pressure Wave Generation

Estimates of pressure wave generation and propagation were made using the capabilities of the ANSYS [] code, the equation of state for mercury provided by the SESAME [ ] library and the energy deposition calculations of the MARS [] code.

The outward velocity of mercury was estimated prior to the experiment by considering the volumetric change of an infinitesimal volume of mercury dV experiencing a change of temperature ΔT and pressure ΔP that result from the fast proton beam. Relations below lead to the estimate the outward velocity U_r as function of sound velocity c of material in the jet

$$
\begin{aligned}
K.E. &= \frac{1}{2}\rho dV U_r^2 \Delta P \delta(dV) \\
\Delta P &\approx \alpha_v \Delta T/k \\
\alpha_v &= (\partial V/\partial T)_P \\
\delta(dV) &= \alpha_v dV \Delta T \\
\mathbf{U}_r^2\mathbf{c}^2 &= 2\alpha_v^2 \Delta T^2 \\
\mathbf{U}_r^2 &= \sqrt{2}[\alpha_v \Delta T]\mathbf{c}
\end{aligned} \tag{3.1}
$$

It is apparent from the above relations that the movement of bulk material as a result of thermal gradients is just a percentage of the velocity of sound that generated pressure waves travel. So, while the pressure field is experiencing the passage of the generated pressure waves (superimposed onto the thermodynamic pressure) the exchange of heat, as well as bulk material movement, is governed by a much slower processes. The verification of this significant relation was one of the goals of E951 in proving that the projectile velocity is much smaller than the velocity of sound and thus the potential for damage to the surrounding target space greatly reduced.

Pressure Wave-Jet Nozzle Interaction

While it is anticipated that the interaction zone of the jet may be broken up several microseconds after the proton beam arrival, the upstream section of the jet is still intact and will allow for the propagation of pressure waves toward the nozzle. At issue is the amplitude of the pressure wave front when it arrives at the nozzle and impacts on the walls. The estimated time of the arrival of the front is approximately 100μs based on a 15-cm distance between the beginning of the interaction zone and the nozzle.

Figures []-[] depict the schematic of the beam/jet interaction arrangement and snapshots of the pressure profile along the mercury jet in a cut through the long axis. While pressures start out as positive, a result of the rapid energy deposition and the inability of the Hg to accommodate thermal expansions, they quickly turn negative at the center of the interaction zone. This is the result of the wave reflections and sign reversal from the free surface of the jet. While part of the interaction region may be destroyed, the pressure front will advance toward the nozzle through the undisturbed jet.

As expected, the pressure wave will attenuate as it travels through the undisturbed part of the jet. Figure [] depict predictions of the pressure wave

fluctuation and amplitude in the nozzle vicinity. While much lower than the initial pressures may make it to the nozzle, a large number of such impacts will accumulate during the operation of the machine that may potentially lead to fatigue failure. The latter becomes more of an issue considering the high irradiation doses the structural materials will receive because of their proximity to the target.

E951 Set-Up

A schematic of the mercury jet target chamber is shown in Figure [ ]. Also shown is the location of the array of fiber-optic strain gauges that were mounded to record strain waves arriving at the nozzle.

To record the mercury jet dispersal two camera systems were used with recording capabilities: 1) at rate of 4 kHz with shutter settings for each frame set to 25μs and 2) 16 frames at speeds up to 1 MHz and exposure time of 150 ns per frame.

Mercury Jet Experimental Results

In the E951 experiment the mercury jet trajectory overlapped with the proton beam for 19 cm. The diameter of the jet at the interaction region ranged between 0.7 cm and 1.7 cm. Achieved proton beam intensities ranged between 0.5-4.0 TP and spot sizes were of the order of 1.6 mm in x-dir and 0.9 mm in y-dir rms sigma radius.

Dispersal of the mercury was observed by viewing prominences as they left the bulk of the mercury jet. Figure [] depicts a series of frames recorded during the experiment showing the evolution of the jet dispersion. Important parameter is the time scale in which events occur. Specifically, the appearance of material emanating from the free jet surface occurs at 0.75 ms. However, a fast camera with capabilities of 1 frame/μ s revealed that the initiation of jet dispersion occurred at a time of ˜ 40 μs.

Such delay time from the onset of proton beam/jet interaction is well in line with the estimates made on the basis of volumetric expansion within the jet. Further, measured velocities of 5 to 50 m/s also tend to agree with velocities estimated from $\mathbf{U}_r = \sqrt{2}[\alpha_v \Delta T]\mathbf{c}$ in which, as observed, the bulk velocity of ejected material is proportional to the temperature rise, which in turn is directly proportional to the intensity of the impinging protons.

Jet Nozzle Results

Four fiber optic strain gauges were placed at selected locations in the mercury line (shown in Figure [ ]). Specifically, a gauge was placed on the line that supplies mercury to the jet just upstream of the nozzle. This gauge, placed along the pipe as shown, is expected to register any activity associated with a wave returning from the jet. The geometry and size of the supply pipe did not allow for the gauge to be placed with hoop orientation. Potential strains along the hoop direction in the pipe wall are expected to be much higher than the axial and thus more easily detectable. Strains in the supply pipe will be the direct result of the pressure in the contained mercury.

In addition to the nozzle gauge, one was placed at the valve outlet (furthest location in the supply pipe upstream of the nozzle) and two were installed on the nozzle mounting plate on either side of the nozzle. Strains for beam intensities ranging between 0 TP and 4 TP (0 TP being the case of jet activity alone) were recorded. While the beam intensity was much lower than anticipated, thus keeping the potential strain aggravation due to shock quite low, still some clear evidence of activity was recorded. Shown in Figure [ ] is the strain recorded by the nozzle gauge for back-to-back pulses with similar intensities (3.75 TP). The stability in the measuring system is shown to be excellent. The front part of the record is the noise from the flowing Hg in the supply pipe. The spike indicates the arrival of the proton beam and it is the effect of photons on the gauges. Beyond that there is evidence of activity induced by the proton beam interacting with the jet.

Figure [ ] quantifies the effect by comparing the strain induced by the jet alone with that of the interaction with the proton beam.

Further examination of these results is needed to make firm assessments. The difficulty stems from the fact that the proton beam intensity received during the first experimental phase was much too low to both qualify and quantify the effects at the nozzle location and draw conclusions about its survival in the actual target setting.

3.5 E951 Graphite & Carbon-Carbon Target Study

3.5.1 Background–Issues/Goals

The need for an alternative target option using a low-Z material with good yield prompted the studies on graphite as one of the candidate materials.

The experimental effort on graphite and carbon-carbon composite as target material for potential use in a high power source had as primary goals the following:

- Attempt to establish limits of material integrity of a particular form of graphite (ATJ grade) as it intercepts the high-energy undiluted proton beam. Of interest in the experimental study was to observe the behavior of the material as it approaches its mechanical strength limits that were anticipated in E951
- Assess the response of the carbon-carbon composite target and verify that its promise of very low thermal expansion coefficient holds true. Verification of the latter will imply that the generated stress conditions within the composite are also very small and thus it can maintain its integrity as a solid target material
- Enable the numerical verification of the response of the solid targets on the basis of recorded strain waves. This part of the effort is extremely useful in that it provides two crucial pieces of information, namely, the calibration of the theoretical/computational model so it can be of use in further studies of solid targets for their susceptibility to failure, and that the comparison of predicted with recorded strain data can provide an additional verification of the estimated energy deposition in the targets

3.5.2 E951 Set-Up

Figures [] and [] represent the schematic arrangement and the actual set-up of the ATJ graphite and carbon-carbon composite targets. Along the axis of one of the beam lines, two 12-inch, 1-cm diameter ATJ rods were placed, while on the other, the two 5-inch, 1-cm diameter carbon-carbon composite rods were set. All four target rods were instrumented with fiber-optic strain

gauges that were to record axial strain. Specifically, the front ATJ rod had 8 gauges (4 in the middle separated by a quadrant, two near the front at 180 degrees apart and two near the back side also at 180 degrees apart. The rear ATJ rod had 7 gauges connected to it (four, two and one respectively). On the carbon-carbon side the front rod was instrumented with 3 gauges and the rear with just two. Special fixtures secured the rods in position with minimal interference to their dynamic response.

3.5.3 Experimental Results–Discussion

Two different sets of experimental measurements provided two beam spot sizes and two intensities. Specifically, one set of data recorded are for a larger spot accompanied by a higher beam intensity, while the other set provided data for a tighter spot but less protons in the pulse. These combinations provided an excellent matrix for purposes of verification of both the numerical predictions in terms of strain and in addition evidence of how well the energy deposition, predicted by different hadronic codes, is estimated. Specifically, energy deposition/distribution in the two ATJ rods were estimated using the codes MARS, GEANT and MCNPX. Figure [ ] depicts the mars calculations for the two different beam spots. Based on comparisons with the theoretically predicted strains, it was assessed that the codes MARS and GEANT generate better correlation of the energy deposition/distribution at these proton energies (24 GeV).

Figures [ ] through [ ] depict recorded strain data along the two ATJ graphite rods. Shown is the out-of-phase strain response between gauges that are 180 degrees apart, a confirmation of the unimpeded response of the rod due to the pin support arrangement. Of importance is the confirmation of all modes of dynamic response of the target rod. Specifically, the axial mode, the bending and the radial mode are all confirmed with the analytical results. In summary,

- Experimental strains in the middle of the ATJ graphite rod show a bending frequency mode somewhere between 380-390 Hz

- Predictions of the detailed model that implemented the supporting/holding fixtures of the target as close to the real setting as possible, predicts a bending frequency of 395 Hz

- The axial "ringing" of the target in the experimental data has a period of 260-265 μs.
- The fundamental axial period T=2L/c (where L is target rod length and c is speed of sound) is approximately 261 microseconds
- The radial "ringing" (which from theory is calculated at 150 KHz or 6.625 μs period), is visible only in the strain record filtered by the 500 KHz acquisition and is in agreement with the experimental data

Figure [] depicts the same strain record for the direct analog signal of 100 KHz and the specially filtered 500 KHz signal. Except for the "radial" ringing that can only be captured well by the 500 KHz-bandwidth, the rest of the record is coincident due to the fact that the involved frequencies are within even the analog bandwidth. Clearly, the need for a system with higher bandwidth capacity is not as serious as in the beam window experimental study.

Figures [ ] through [] represent experimental and prediction data for both ATJ graphite target rods and for the different beam spot/intensity combinations. The need to maintain a very small element size in the finite element model such that the smallest wavelength strain wave induced by the beam can propagate through the rod, combined with the very small step size, allowed the completion of only a few significant cycles. It is apparent, however, that both the amplitude of the strain as well as the structure of the response are predicted quite well for both beam settings.

As expected with the carbon-carbon composite, and shown in Figures [ ] and [ ], the strain levels that are seen by the rod are much lower than those seen in the ATJ rods. However, they are not totally insignificant (as claimed by various manufactures but for slow heating) and there appears to be a "dynamic structure" in the response shown in Figure [].

For both solid target types, however, the beam intensity achieved during the experiment did not reach levels that would challenge the structural integrity of the targets, something that the experiment would have liked to see.

Bibliography

[1] M. Zisman, *Status of Neutrino Factory and Muon Collider R & D*, PAC2001, WOAB008.

[2] Osaki et al., eds., *Feasibility Study-II of a Muon-Based Neutrino Source*, http://www.cap.bnl.gov/mumu/studyii/FS2-report.html

[3] H. Kirk et al., *Target Studies with BNL E951 at AGS*, PAC2001, TPAH137

[4] K. Brown, et al., *First Beam Tests of the Muon Collider Target Test Beam Line at the AGS*, PAC2001, TPAH129

[5] N. Simos, et al., *Thermal Shock Analysis of Windows Interacting with Energetic, Focused Beam of the BNL Muon Target Experiment*, PAC2001, TPAH085

[6] R.B. Oswald, et al., *One-Dimensional Thermoelastic Response of Solids to Pulsed Energy Deposition*, Journal of Applied Physics, Vol. 42, No. 9, pp. 3463-3473, 1971

[7] D. Burgreen, *Thermoelastic Dynamics of Rods, Thin Shells and Solid Spheres*, Nucl. Sc. And Eng., 12, 203-217, 1962

[8] P. Sievers, *Elastic Stress Waves in Matter due to Rapid Heating by Intense High-Energy Particle Beam*, LAB.II/BT/74-2, CERN, 1974

[9] H. Conrad, *On Elastic Stress Waves in Targets*, Institut fur Festkorperforschung, 1994

[10] N.V. Mokhov, *The MARS Code System User Guide, Version 13 (95)*, 1995

[11] *ANSYS Engineering Analysis of Systems*, Swanson Analysis Systems Inc.

fact
Muon Collaboration

Chapter 4

Perturbative Calculations and Simulations

4.1 First Order Perturbative Calculations for a Conducting Liquid Jet in a Solenoid

4.1.1 Introduction

A mercury jet, injected at an angle with respect to the axis of the solenoidal field, is the current baseline solution for the Feasibility Study II[1]. The interaction of the liquid-metal jet with the strong 20 T target solenoid has as result a number of forces on the jet which potentially may affect the viability of this target.[2] – [6] We present here perturbative calculations which confirm and extend the findings of previous authors.

4.1.2 Analytic Treatment

Introduction

The jet is assumed to have an initial radius r_o, and initial velocity v. Changes in radius, shape, direction and velocity are all assumed to be small. The angle between the jet and solenoid axes is also assumed to be small. Furthermore, we assume the jet to be very long $r_o \ll L$, and with zero viscosity.

In the following formulae, the coordinate system is defined by the jet; z is along the direction of motion and r is the radial coordinate.

If the jet is not directed along the solenoid axis, then we also define y in the plane of that axis and the jet and in a direction perpendicular to z (the jet axis) and away from the solenoid axis; and x perpendicular to y and z. We also define a second coordinate system x' y' z', where z' is aligned along the magnet axis. Assuming a small angle $\theta^2 << 1$ then (See Fig. 4.1.2):

$$\begin{aligned} x' &= x, \\ y' &\approx y_o + y + z\theta, \qquad (4.1) \\ z' &\approx z - (y + y_o)\theta \\ r'^2 &\approx r^2 + y_o^2 + 2yy_o + 2z\theta(y + y_o) \qquad (4.2) \end{aligned}$$

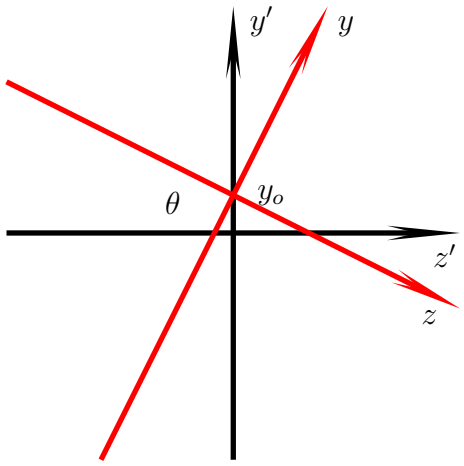

Figure 4.1: Schematic of the geometrical arrangement of solenoid and jet.

Induced azimuthal current

The magnetic flux through a circle of radius r perpendicular to the jet axis is

$$\Phi = \int_S dS\vec{n} \cdot \vec{B} \approx \pi r^2 B_z(x, y, z). \tag{4.3}$$

As a liquid metal jet passes axially down such a field at a velocity $v = dz/dt$, a circumferential potential will be generated

$$V \equiv \oint \vec{E} \cdot \vec{dl} = -\frac{d\Phi}{dt} = \pi r^2 v \frac{\partial B_z(x, y, z)}{\partial z}. \tag{4.4}$$

If the metal electrical conductivity κ is low enough so that the resulting current has a negligible effect on the field, then the azimuthal current density i_ϕ will be

$$i_\phi \approx \frac{V}{2\pi r}\kappa \approx -\frac{rv\kappa}{2}\frac{\partial B_z(0, 0, z)}{\partial z}. \tag{4.5}$$

Radial forces and hydrostatic pressure

The induced radial force per unit volume ($rdrd\phi dz$) is

$$f_r = B_z i_\phi \approx \frac{r}{2} v\kappa B_z \frac{\partial B_z}{\partial z}. \tag{4.6}$$

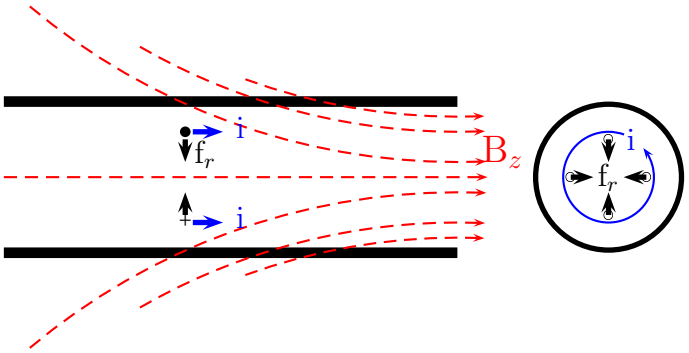

Figure 4.2: Radial pressure force produced by the axial magnetic field and the induced azimuthal current.

If we assume that the effects of the fields are small, so that the jet radius and liquid velocities do not vary by large fractions, and if we ignore radial inertia, then the hydrostatic pressures in a jet of outside radius r_o, at radius r, will be given by

$$p(r,z) = \int_{r_o}^{r} -f_r dr \approx \left(\frac{r_o^2 - r^2}{4}\right)\ v\kappa\ B_z \frac{dB_z}{dz}. \tag{4.7}$$

Axial force

The above hydrostatic pressure is a function of z, and gradients in it will exert axial pressures f_p on the liquid that must be added to the magnetic term f_z.

$$f_p(\text{hydrostatic}) = \frac{\partial p(r,z)}{\partial z} \approx \ - \ \left(\frac{r_o^2 - r^2}{4}\right)\ v\kappa\ \frac{\partial}{\partial z}\left(B_z \frac{\partial B_z}{\partial z}\right). \tag{4.8}$$

To this must be added the axial forces induced directly by the fields acting on the asimuthal currents: If the jet is aligned with the field axis ($\theta = 0$), the radial field is given by

$$B_r(\theta = 0) \approx -\frac{r}{2}\frac{\partial B_z(0,0,z)}{\partial z}. \tag{4.9}$$

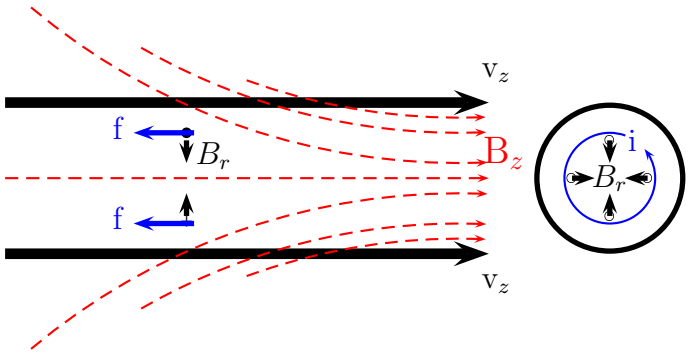

Figure 4.3: Retarding force in the axial direction

The induced axial force per unit volume ($dr\ d\phi\ dz$) is

$$f_z(\theta = 0) = f_p(r, z) - B_r i_\phi. \tag{4.10}$$

If the jet is at an angle to the magnetic axis, then there is an additional shear force:

$$f_z(\theta) = f_p(r, z) - B_y i_\phi\ \sin(\phi) \quad \text{with} \quad B_y \approx \theta B_z(0, 0, z), \tag{4.11}$$

giving, in all:

$$f_z \approx -\left(\frac{r_o^2 - r^2}{4}\right) v\kappa \frac{\partial}{\partial z}\left(B_z \frac{\partial B_z}{\partial z}\right) + \frac{r^2}{4} v\kappa \left(\frac{\partial B_z}{\partial z}\right)^2 + \frac{rv\kappa}{2} B_y \frac{\partial B_z}{\partial z} \sin\phi \tag{4.12}$$

On the jet axis:

$$f_z \approx -\left(\frac{r_o^2}{4}\right) v\kappa \frac{\partial}{\partial z}\left(B_z \frac{\partial B_z}{\partial z}\right). \tag{4.13}$$

On the outer surface, averaged over the azimuthal angle ϕ, or in the absence of B_y:

$$f_z \approx \frac{r_o^2}{4} v\kappa \left(\frac{\partial B_z}{\partial z}\right)^2. \tag{4.14}$$

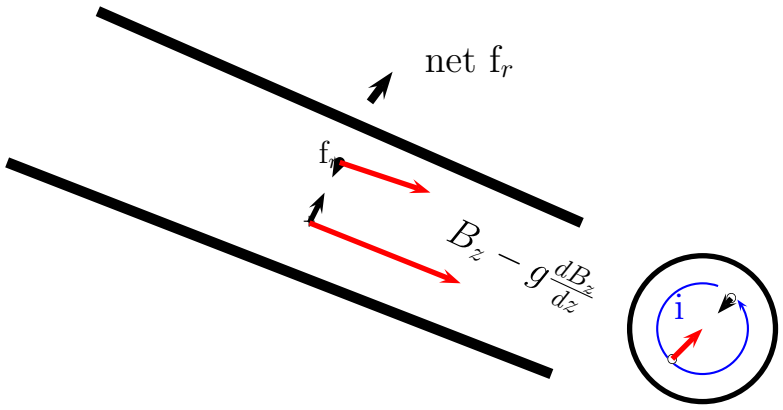

Figure 4.4: Deflection in the tilded case

On the outer surface, with a finite B_y, as in the case of a jet at an angle to the magnetic axis:

$$f_z \approx \frac{r_o^2}{4} v\kappa \left(\frac{\partial B_z}{\partial z}\right)^2 + \frac{y}{2} v\kappa\, B_y \frac{\partial B_z}{\partial z} \tag{4.15}$$

and the average force of the disk of radius r_o is given by integrating the terms

$$< f_z > \approx \frac{r_o^2}{8} v\kappa \left[\left(\frac{\partial B_z}{\partial z}\right)^2 + \frac{\partial}{\partial z}\left(B_z \frac{\partial B_z}{\partial z}\right)\right] \tag{4.16}$$

Axial accelerations

These forces will then decelerate, or accelerate layers of the fluid, thus inducing differences of liquid velocity as a function of radius

$$\frac{dv}{dz} = \frac{f}{\rho\, v} \tag{4.17}$$

where ρ is the fluid density.

$$\Delta\, v(r,z) = \int_{z_o}^{z} (f_z + f_p)\, \frac{1}{v\rho}\, dz \tag{4.18}$$

The average change in velocity is then

$$< \Delta v > (z) \;=\; \frac{\kappa}{\rho}\,\frac{r_o^2}{8}\,\left(\int_{z_o}^{z}\left(\frac{dB_z}{dz}\right)^2 \;+\; \frac{d}{dz}\left(B_z\frac{dB_z}{dz}\right)\;dz\right) \tag{4.19}$$

and the radius as a function of z is

$$r(z) \;=\; r_o\,\left(1 \;-\; \frac{< \Delta v > (z)}{v}\right) \tag{4.20}$$

Transverse forces and deflections

From Eq. 4.6, the radial force per unit volume ($dr\ r\ d\phi dz$) is $f_r = B_z i_\phi \approx \frac{r}{2}\ v\kappa\ B_z\frac{\partial B_z}{\partial z}$; if B_z varies with a transverse distance y, then the component of this radial force in the y direction is

$$f_y = f_r\ \sin\phi \tag{4.21}$$

and the net deflective force dF_y per unit length dz is

$$\frac{\partial F_y}{\partial z} \;=\; \int_0^r\ \int_0^{2\pi}\frac{r}{2}\ v\kappa\ \frac{\partial B_z}{\partial y}\ r\sin^2\phi\frac{\partial B_z}{\partial z}\ r\ dr d\phi \tag{4.22}$$

$$= \frac{v\kappa}{2}\ \frac{\partial B_z}{\partial y}\ \frac{\partial B_z}{\partial z}\ \int_0^{2\pi}\sin\phi^2 d\phi\int_0^r r^3\ dr \tag{4.23}$$

$$= \frac{\pi}{8}v\kappa\ r^4\ \frac{\partial B_z}{\partial y}\ \frac{\partial B_z}{\partial z}. \tag{4.24}$$

The change in transverse velocity is

$$\begin{aligned}\frac{\partial v_y}{\partial z} &= \frac{1}{v}\frac{\partial v_y}{dt}\\ &= \frac{\frac{dF_y}{dz}dz}{v\rho\pi r^2 dz}\\ &= \frac{\kappa r^2}{8\rho}\frac{\partial B_z}{\partial y}\frac{\partial B_z}{\partial z}.\end{aligned}$$

The inverse radius of bend is

$$\frac{d^2y}{dz^2} \;=\; \frac{d\theta}{dz} \;=\; \frac{\kappa\ r^2}{8\ v\ \rho}\ \frac{\partial B_z}{\partial y}\ \frac{\partial B_z}{\partial z}. \tag{4.25}$$

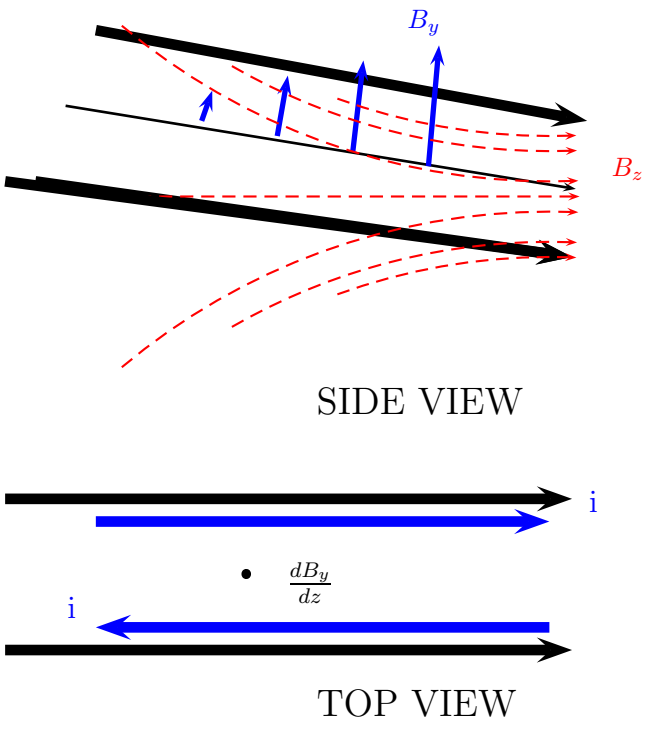

Figure 4.5: Induced axial current due to gradients in the radial field

Induced axial current

Consider a transverse field component B_y

The magnetic flux between transverse positions $-x$ to x and dz is

$$d\Phi_y = 2xdzB_y(z) \tag{4.26}$$

As a liquid metal jet passes axially down such a field at a velocity $v = dz/dt$, axial voltage gradients will be generated

$$G = -x\frac{\partial B_y}{\partial z}v \tag{4.27}$$

If the metal electrical conductivity κ is low enough so that the resulting current has a negligible effect on the field, then the axial current density i_z

will be

$$i_z = G\kappa = i_z \ = xv\kappa\frac{\partial B_y(0,0,z)}{\partial z} \tag{4.28}$$

Transverse elliptical distortion

If the jet is not on the solenoid axis, the axial induced currents interacting with the transverse fields will generate distorting forces on the jet. These transverse forces per unit volume $dx\ dy\ dz$ are

$$f_x \ = \ i_z\ B_y \ = \ x\ v\ \kappa\ B_y\ \frac{\partial B_y}{\partial z} \tag{4.29}$$

This force will distort the cross section. Assuming that the liquid is incompresible, we must find the induced pressures and motions $\Delta\vec{r}$ within the cross section that are driven by this force, with the constraint that the divergence of these motions is zero:

$$Div(\Delta\vec{r}) \ = \ 0 \tag{4.30}$$

Defining

$$F_o \ = \ v\ \kappa\ B_y\ \frac{\partial B_y}{\partial z}, \tag{4.31}$$

so that the magnet force per unit volume is

$$f_x(\text{magnetic}) \ = \ x\ F_o. \tag{4.32}$$

Magnetic Forces

The pressure on the surface of the jet will be independent of azimuthal angle ϕ

$$p(r_o)_{\text{circular}} = p_{\text{atm}} \ + \ T/r_o\ , \tag{4.33}$$

T being the surface tension. If the initial cross section is circular, we can consider pressures within the cross section:

$$p = p_o + r^2\frac{F_o}{4}, \tag{4.34}$$

where p_o is set by the constraint on the above surface pressure at $r = r_o$. This bulk pressure will induce radial pressure forces:

$$f_r(\text{pressure}) \ = \ \frac{\partial p}{\partial r} \ = \ - \ \frac{r\ F_o}{2}; \tag{4.35}$$

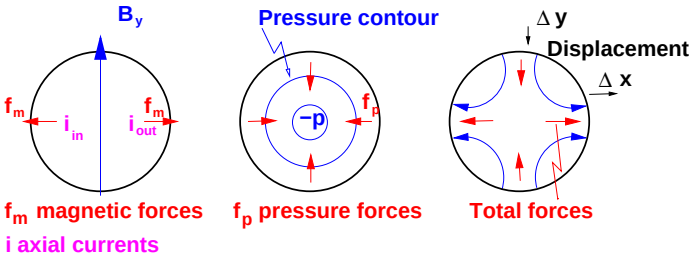

Figure 4.6: Distortion produced by the magnetic forces

so

$$f_x(\text{total}) = \frac{F_o\ r\ \cos(\phi)}{2} = \frac{x\ F_o}{2}; \tag{4.36}$$

$$f_y(\text{total}) = -\frac{F_o\ r\ \sin(\phi)}{2} = -\frac{y\ F_o}{2}. \tag{4.37}$$

The accelerations

$$\frac{d^2x,y}{dz^2} = \frac{f_{x,y}}{v^2\ \rho} \tag{4.38}$$

will give dispacements:

$$\Delta x = \int\int \frac{f_{x,y}}{v^2\ \rho}\ dz^2 = x\ \frac{\kappa}{2\ v\ \rho} \int\int B_y\ \frac{\partial B_y}{\partial z}\ dz^2, \tag{4.39}$$

$$\Delta y = \int\int \frac{f_{x,y}}{v^2\ \rho}\ dz^2 = -\ y\ \frac{\kappa}{2\ v\ \rho} \int\int B_y\ \frac{\partial B_y}{\partial z}\ dz^2. \tag{4.40}$$

Such motions are quadrupole (see Fig. 4.6) and, as required, give $Div\ (\Delta x, \Delta y) = 0$. The resulting ellipticity $\epsilon = \frac{\Delta x_o}{r_o} = -\frac{\Delta y_o}{r_o}$

$$\epsilon(z) = \frac{\kappa}{2\ v\ \rho} \int\int B_y\ \frac{\partial B_y}{\partial z}\ dz^2. \tag{4.41}$$

Surface tension forces

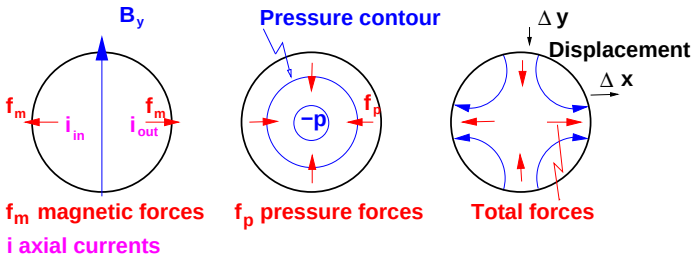

Figure 4.7: Restoring surface tension forces

Once the cross section becomes somewhat elliptical (we consider only a small ellipticity), then the pressure at the surface is no longer independent of the asimuthal angle ϕ, but is given by:

$$p(r = r_o) \;=\; p_{\rm atm} \;+\; \frac{T}{r_0}\;(1 \;-\; \epsilon\;\cos(2\;\phi))\,. \tag{4.42}$$

Consider, in addition to those given above for the circular case, pressures within the cross section:

$$p(x,y)_{\rm elliptical} = p_o + \frac{T\;\epsilon}{r_o}\left(\cos^2(\phi) \;-\; \sin^2(\phi)\right) = p_o + \frac{T\;\epsilon}{r_o^3}(x^2 \;-\; y^2), \tag{4.43}$$

which has the correct values at $r = r_o$.

Defining

$$S_o \;=\; \frac{2\;T\;\epsilon}{r_o^3}, \tag{4.44}$$

the resulting bulk forces are:

$$f_x(\text{elliptical}) \;=\; \frac{\partial p}{\partial x} \;=\; x\; S_o, \tag{4.45}$$

$$f_y(\text{elliptical}) \;=\; \frac{\partial p}{\partial y} \;=\; -\,y\; S_o. \tag{4.46}$$

Once again, these are quadrupole forces that will generate quadrupole motions with Div($\Delta\vec{r}$)=0:

$$(\Delta x, \Delta y) = \int\int \frac{(x,\; -\,y)}{v^2\;\rho}\; S_o\; dz^2, \tag{4.47}$$

Magnetic and surface tension forces

Adding these surface tension displacements to the forces derived for the circular case:

$$(\Delta x, \Delta y) = \;(x,\;\; -\,y)\; \int\int \left(\frac{\kappa}{2\;v\;\rho}\; B_y\; \frac{\partial B_y}{\partial z} \;+\; \frac{2\;T\;\epsilon}{v^2\;\rho\;r_o^3}\right)\; dz^2, \tag{4.48}$$

and the resulting ellipticity $\epsilon = \frac{\Delta x_o}{r_o} \;=\; -\,\frac{\Delta y_o}{r_o}$:

$$\epsilon(z) \;=\; \int\int \left(\frac{r_o\;\kappa}{2\;v\;\rho}\; B_y\; \frac{\partial B_y}{\partial z} \;+\; \frac{2\;T\;\epsilon}{v^2\;\rho\;r_o^2}\right)\; dz^2. \tag{4.49}$$

4.1.3 Gaussian Case

We can consider a field that varies as a Gaussian in z. The fields of the solenoid and coordinates are denoted with primes ($'$).

The fields in the magnet system are:

$$B'_z(0,z') \;\approx\; B_o e^{-\frac{z'^2}{2\sigma_z^2}} \tag{4.50}$$

$$B'_z(r',z') \;\approx\; B'_z(0,z') - \frac{1}{4}r'^2\frac{\partial^2 B'_z(0,z')}{\partial z'^2}, \tag{4.51}$$

$$B'_r(r',z') \;\approx\; -\frac{1}{2}r'\frac{\partial B'_z(0,z')}{\partial z'}. \tag{4.52}$$

In the coordinate system of the jet, see Fig. 4.1.2, assuming a very small angle θ, the fields are

$$\begin{aligned}
B_z(x,y,z) &\approx \left[B'_z(r',z') - \frac{1}{2}\theta\ y_o\ \frac{\partial B'_z(0,z')}{\partial z'}\right], \\
B_x(x,y,z) &\approx -\frac{1}{2}x\frac{\partial B'_z(0,z')}{\partial z'}, \\
B_y(x,y,z) &\approx -\left[\frac{1}{2}(y_o + z\theta)\frac{\partial B'_z(0,z')}{\partial z'} - \theta B'_z(r',z')\right], \\
\frac{\partial B_z(x,y,z)}{\partial z} &\approx \left[\frac{\partial B'_z(0,z')}{\partial z'} - \frac{1}{2}\ y_o\ \theta\frac{\partial^2 B'_z(0,z')}{\partial z'^2}\right], \\
\frac{\partial B_y(x,y,z)}{\partial z} &\approx \left[\frac{1}{2}\theta\frac{\partial B'_z(0,z')}{\partial z'} - \frac{1}{2}(\ y_o\ + z\theta)\frac{\partial^2 B'_z(0,z')}{\partial z'^2}\right]. \qquad (4.53)
\end{aligned}$$

4.1.4 Early Example

In our earlier studies we had considered a jet entering from outside the field, with the following parameters:

Table 4.1: Jet parameters for our earlier studies.

r_o (mm)	5
v_o (m/s)	20
θ (mrad)	100
σ_z (m)	0.6

Using the above fomulae we obtain the results plotted in Figs. 4.8 and summarized in Tb. 4.2,

Table 4.2: Summary of maximum and minimum values of the quantities shown in Fig. 4.8

B_z	Δp	$<\Delta v>$	Δv	Δy	Δx/r No ST	Δx/r
T	Atm.	m/s	m/s	mm	%	%
0.077	-0.245	-0.125	-5.542	-0.060	0.0	26
20.0	0.351	0.	0	0.045	423	-21

It is seen that although the deflection of the jet is small (0.04 mm) and

the average deceleration is reasonable (0.125 m/s), yet there are several unacceptable results:

- The hydrostatic pressure falls to -0.24 atmosphers, and would require a high-pressure environment to stop the jet breaking up.
- There are shear accelerations of ±5.5 m/s.
- The calculated distortion with surface tension included is 21% (without the surface tension it is 423%), indicating that the calculation is beyond its valid region, but suggesting that the jet will be badly disrupted.

Clearly these parameters are unacceptable.

4.1.5 Study II Example with $v = 30$ m/s

For Study II, several parameters were changed from the above example. The jet velocity increased, the magnetic field was kept more uniform, and the nozzle introduced inside the magnetic field.

The beam with rms radius $\sigma_r = 3$ mm intersects a mercury jet of radius r_o at an angle $\theta_{crossing}$. The forward velocity of the jet is v_o. The intervals between pulses is t, and it will be assumed here that after a pulse, all the mercury outside of the nozzle is dispersed. The nozzle is at z_{nozzle} with respect to the intersection of the beam and jet center lines. Consider the following parameters:

Table 4.3: Proton beam and jet parameters for Study II example.

σ_r (mm)	1.5
r_o (mm)	5
$\theta_{crossing}$ (mrad)	33
v_o (m/s)	30
t (ms)	20
z_{nozzle} (m)	-0.375

The geometry is shown in Fig. 4.9, with the distribution of resulting interactions as a function of z is shown above. At the time of a second, or subsequent bunch, the newly established jet will extend a distance $z_{jet} = v_o\ t = 0.6$ m from the nozzle. It is seen that only 2.5 % of the interactions

Table 4.4: Hg jet parameters.

B_o (T)	20
σ'_z (m)	0.8
θ_{jet} (mrad)	-100
κ (Ω m)	10^6
ρ (kg/m^3)	13.5 10^4
$T_{\rm surface}$ (N/m)	0.456
$p_{\rm gas} = p_{\rm atmospheric}$ (N/m^2)	10^5

would occur after this location, had the beam extended indefinitely. Thus there is a negligible loss from this limited jet extent.

Thus the total length over which the jet must propagate without serious magnetic disruption is from the nozzle to a point 0.6 m downstream. In order to minimize the field non uniformity over this length, the magnetic center (approximate point of maximum B_z is placed at the center of this length. *i.e.* the magnetic center is set at a distance $z_{magnet} = z_{jet}/2 - z_{nozzel} = \ -0.15$ m with respect to the jet-beam intersection.

The proton beam enters at an angle θ_{beam} with respect to the magnet axis. The jet is at an angle $\theta_{jet} = \theta_{beam} - \theta_{crossing}$. The vertical distance y_o from the magnet center $(z = 0, r = 0)$ to the jet axis at $z = 0$ can be chosen to minimize beam disruption. We assume a Gaussian distribution of B'_z vs z', with a maximum value of B_o, The jet conductivity κ, density ρ, and surface tension $T_{surface}$, and the other parameters are given below:

Figures 4.10 use a horizontal scale with $z = 0$ at the magnetic center. Plots are shown for

a) The axial magnetic field B_z

b) The hydrostatic pressure on the jet axis with respect to the environment outside the jet $(p_{\rm axis} - p_{\rm gas})$

c) The average deceleration of the jet Δ_v(Ave)

d) The maximum shear acceleration/deceleration of the upper/lower limits of the jet Δ_v(shear)

e) The vertical displacement of the jet due to deflecting forces y

g) The resulting elliptical distortion ($\Delta x/r = -\Delta y/r$), with and without surface tension.

We see that over the extent of the new jet (from - 0.3 to 0.3 m):

- The maximum axial field deviations are +/− 1.1 T = 5
- The axial pressure difference has a minimum of - 0.25 atmospheres. Thus if the jet is operating in a gas (He or Argon) at a pressure greater than or equal to 0.25 atmosphere, then the negative pressures will be avoided, and there will be no tendency to cavitate prior to the arrival of the beam.
- The maximum average deceleration of the jet is very small compared to the average jet velocity: 0.06/30≈0.2
- The maximum decelerations (from shear forces) are also small compared to the average jet velocity: 0.4/30≈1.3%.
- The deflections of the jet are very small: 5μm.
- The jet distortions (Δ width / ave width) are approximately 4% without surface tension, and less than 0.2% with surface tension.

Beyond the target region (z=0.3 to 1.5 m), the effects are larger, but still not sufficient to break up the jet. The maximum shear is about 5 m/sec, and the distortion 20 %. But these numbers are probably meaningless, since the jet will have been disrupted by the beam. These results are much better than in the earlier example and are considered to be acceptable.

We summarize in Tb. 4.5 these results

4.1.6 Coil Design

The coil dimensions are given in Tb. 4.6.

The axial fields are shown in Figs. 4.11. The left figure shows the components from: the use of iron (green), superconductors (blue), and the total (red). The Gaussian distribution used in the above calculations is also given in Fig. 4.11-right (black), and is seen to be a good match to the total field over the target region (-0.6 m to 0).

Table 4.5: Summary of maximum and minimum values of the quantities shown in Fig. 4.10

B_z	Δp	$< \Delta v >$	$\hat{\Delta v}$	Δy	Δx/r No ST	Δx/r
T	Atm.	m/s	m/s	mm	%	%
18.8	-0.240	0.0	-0.41	0.0	0.0	0.0
20.0	0.245	0.058	-0.019	0.005	0.37	0.18

Table 4.6: Coils used in the Study II target magnet [7]

len1 (m)	gap (m)	dl (m)	rad (m)	dr (m)	I/A (A/mm^2)	n I (A)	n I l (Am)
Fe							
0.980	0.980	0.108	0	0.313	0	0	0
1.088	0	0.312	0	0.168	0	0	0
Hollow							
1.288	-0.112	0.749	0.178	0.054	-24.37	0.98	1.26
1.288	-0.749	0.877	0.231	0.122	-19.07	2.04	3.74
1.288	-0.877	1.073	0.353	0.137	-14.87	2.18	5.78
SC							
0.747	-1.614	1.781	0.636	0.642	-23.39	26.77	160.95
2.628	0.100	0.729	0.686	0.325	-25.48	6.04	32.23
3.457	0.100	0.999	0.776	0.212	-29.73	6.29	34.86
4.556	0.100	1.550	0.776	0.107	-38.26	6.36	33.15
6.206	0.100	1.859	0.776	0.066	-49.39	6.02	30.59
8.000	-0.065	0.103	0.416	0.051	-68.32	0.36	1.00
8.275	0.172	2.728	0.422	0.029	-69.27	5.42	14.88
11.053	0.050	1.749	0.422	0.023	-75.62	3.00	8.18
12.852	0.050	1.750	0.422	0.019	-77.37	2.61	7.09
14.652	0.050	1.749	0.422	0.017	-78.78	2.30	6.22
16.451	0.050	1.750	0.422	0.015	-79.90	2.07	5.59
18.251	0.050	2.366	0.422	0.013	-80.85	2.53	6.80

4.1.7 Conclusion

- It is not acceptable to have the jet nozzle outside the magnetic field.
- With the Study II parameters, all disruptive effects are negligible up to the distance traveled by the jet since the last pulse.
- Even beyond this location, the disruptions are not unreasonable, and would not, of themselves, disrupt the jet.
- It would probably be acceptable to shorten the high field region, if this were desired for cost reasons.

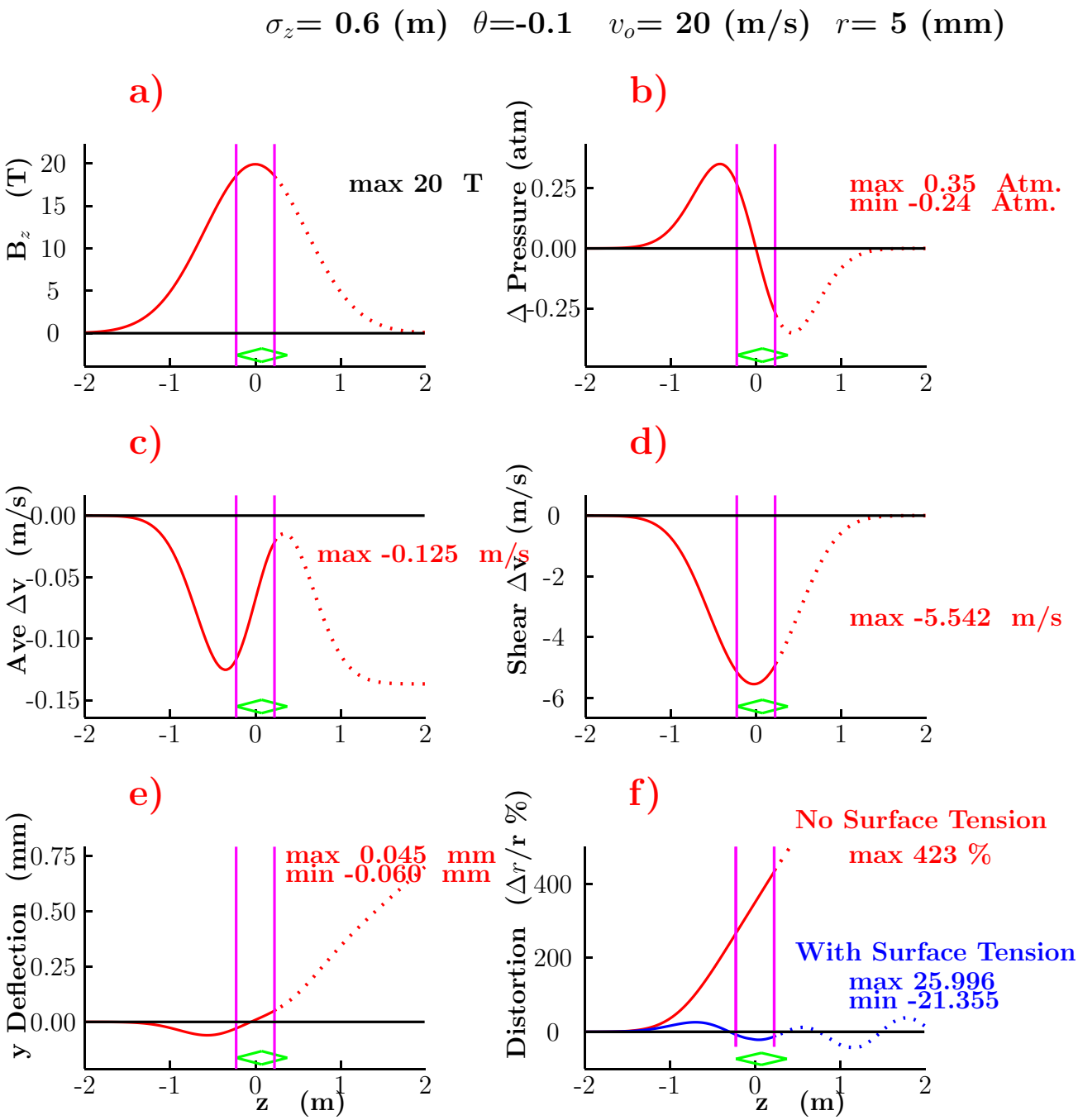

Figure 4.8: Results for the case of a jet entering a magnetic field with parameters listed in Tb. 4.1.

fact
Muon Collaboration

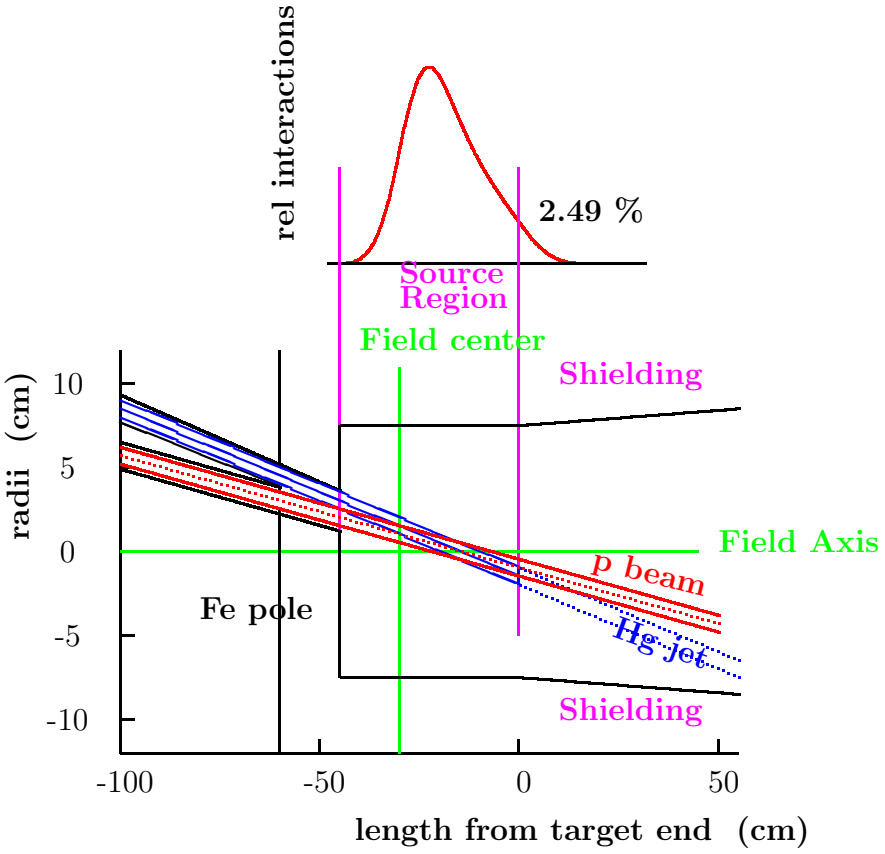

Figure 4.9: Geometry of the Hg jet, proton beam and target magnet; on top is the distribution of interactions as a function of z.

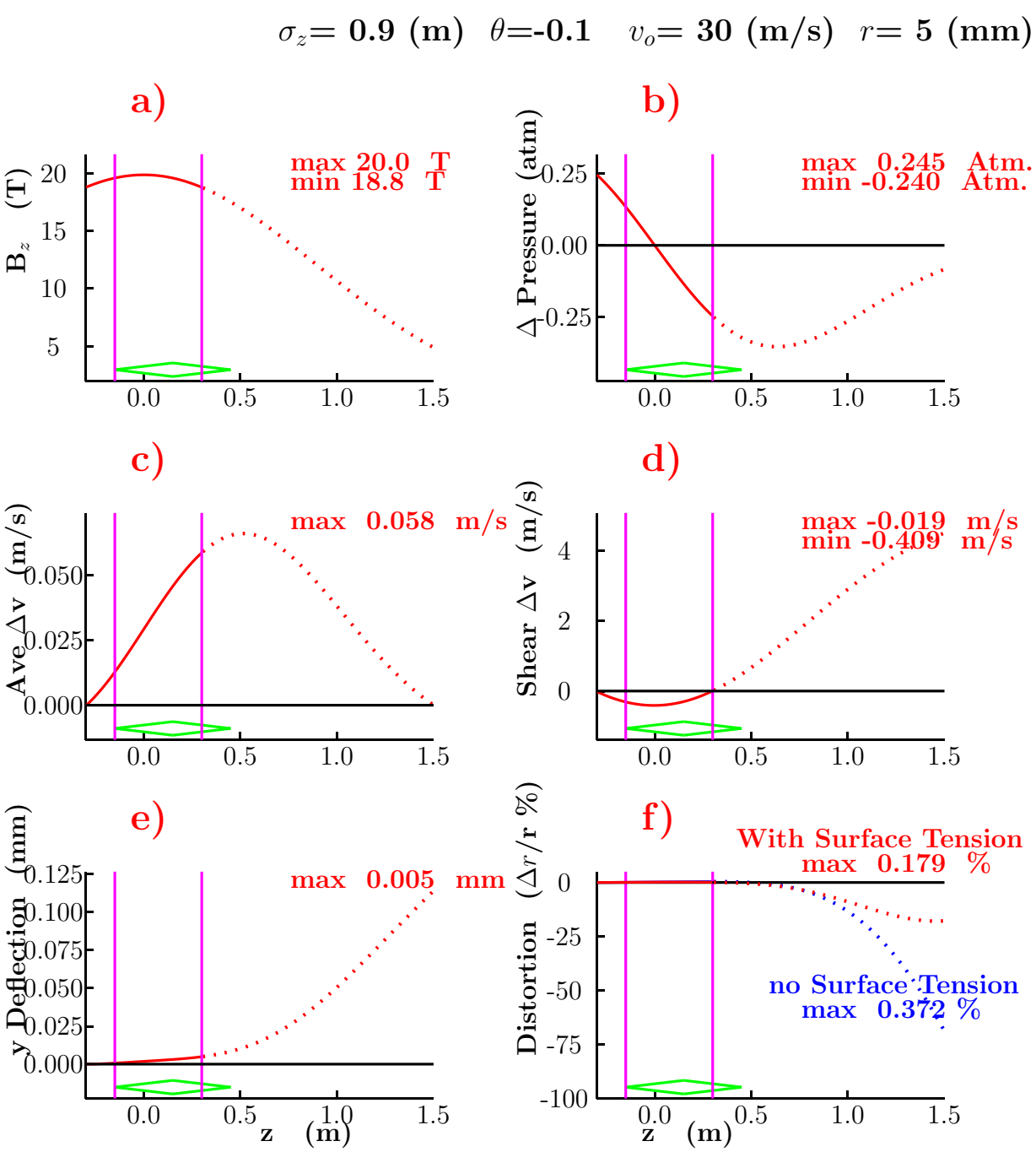

Figure 4.10: Results for the case of a jet with the noozle inside the magnetic field.

fact
Muon Collaboration

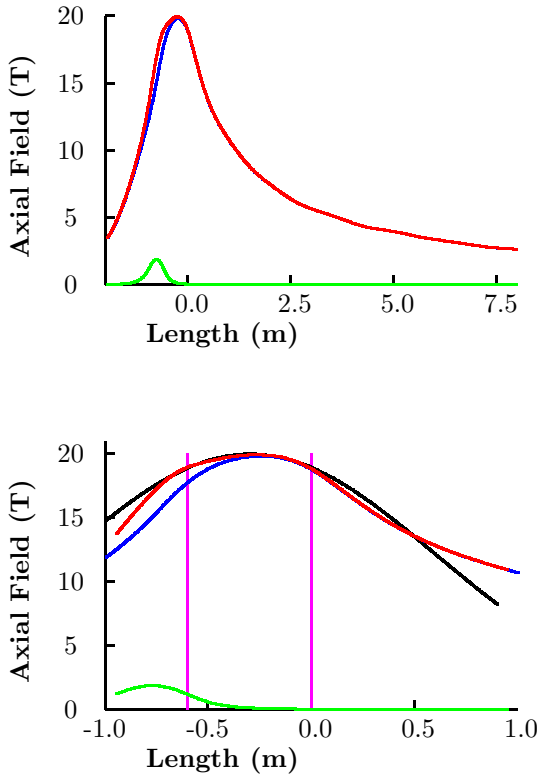

Bibliography

[1] http://www.cap.bnl.gov/mumu/studyii/

[2] K. McDonald (Ed), *An R&D Program for Targetry and Capture at a Muon-Collider Source*, Proposal to the BNL AGS Division, p.23

[3] R. Weggel, *Behavior of conducting solid or liquid jet moving in magnetic field: 1) Paraxial; 2) Transverse; 3) Oblique*, BNL report BNL-65611/CAP-220-Muon-98R

[4] **Phys. Today**, Feb 2000, p.29

[5] K. McDonald, *Damping and Radial Pinching Effects*, http://www.hep.princeton.edu/˜mcdonald/mumu/target/radialpinch.ps

[6] P. Thieberger, *Estimated perturbations of the axial motion of a liquid-metal jet entering a strong magnetic field* , MUC-NOTE-TARGET-0182, Nov. 2000.

[7] R. Weggel, *20 T Hybrid magnet for Study II*

4.2 Numerical Simulation of the Muon Collider Target

The numerical simulation of hydro- and magnetohydrodynamics processes in the Muon Collider target is needed for better understanding of the physics involved and for answering engineering design questions. The Muon Collider target will contain a series of mercury jet pulses of about 0.5 cm in radius and 60 cm in length. Each pulse will be shot at a velocity of 30-35 m/sec into a 20 Tesla magnetic field at a small angle (0.1 rad) to the axis of the field. When the jet reaches the center of the magnet, it is hit with 3 ns proton pulses arriving with 20 ms time period; each proton pulse will deposit about 100 J/g of energy in the mercury.

The main issues of the target design addressed in our numerical studies are the distortion of the jet due to eddy currents as it propagates through the magnetic coil, the deformation of the jet surface due to strong pressure waves caused by the proton pulses and the probability of the jet breakup. Studying the state of the target during its interaction with proton pulses will help to achieve the maximal proton production rate and therefore an optimal target performance.

4.2.1 Magnetohydrodynamics of Free Surface Liquid Flows

The basic set of equations describing the interaction of a compressible conducting fluid flow and a magnetic field is contained in Maxwell's equations and in the equations of fluid dynamics suitably modified [1, 11]. Namely, the systems contains the mass, momentum and energy conservation equations for the fluid which have hyperbolic nature and a parabolic equation for the evolution of the magnetic field.

$$\frac{\partial \rho}{\partial t} = -\nabla \cdot (\rho \mathbf{u}), \tag{4.54}$$

$$\rho \left(\frac{\partial}{\partial t} + \mathbf{u} \cdot \nabla \right) \mathbf{u} = -\nabla P + \rho \mathbf{X} + \frac{1}{c}(\mathbf{J} \times \mathbf{B}), \tag{4.55}$$

$$\rho \left(\frac{\partial}{\partial t} + \mathbf{u} \cdot \nabla \right) U = -P \nabla \cdot \mathbf{u} + \frac{1}{\sigma}\mathbf{J}^2 - \frac{1}{c}\mathbf{u} \cdot (\mathbf{J} \times \mathbf{B}), \tag{4.56}$$

$$\frac{\partial \mathbf{B}}{\partial t} = \nabla \times (\mathbf{u} \times \mathbf{B}) - \nabla \times (\frac{c^2}{4\pi\sigma} \nabla \times \mathbf{B}), \tag{4.57}$$

$$\nabla \cdot \mathbf{B} \quad = \quad 0, \tag{4.58}$$

Here $\mathbf{u}$, ρ and U are the velocity, density and total energy of the fluid, respectively, P is the total stress tensor, $\mathbf{X}$ includes external forces of non-magnetic origin, $\mathbf{B}$ is the magnetic field induction, $\mathbf{J}$ is the current density distribution and σ is the fluid conductivity. The magnetic field $\mathbf{H}$ and magnetic induction $\mathbf{B}$ are related by the magnetic permeability coefficient μ: $\mathbf{B} = \mu\mathbf{H}$.

The system (4.54-4.57) must be closed with an equation of state. We are especially interested in fluid behavior under extreme thermodynamics conditions. Some related equation of state models are discussed below.

The following boundary conditions must be satisfied at the jet surface:

i) the normal component of the velocity field is continuous across the material interface.

ii) the normal and tangential components of the magnetic field at the material interface are related as

$$\mathbf{n} \cdot (\mathbf{B}_2 - \mathbf{B}_1) = 0, \tag{4.59}$$

$$\mathbf{n} \times (\mathbf{H}_2 - \mathbf{H}_1) = \frac{4\pi}{c}\mathbf{K}, \tag{4.60}$$

where $\mathbf{K}$ is the surface current density. The above jump conditions define the refraction of magnetic lines on the material interface. We can assume $\mu = 1$ for most fluids. Notice that the surface current density $\mathbf{K}$ corresponds to a current localized in a thin fluid boundary layer (δ-functional current) which is non-zero only for superconducting materials. The current density in fluids at normal conditions is distributed in the 3D volume and $\mathbf{K} = 0$. Therefore, the equations (4.59,4.60) simply require the continuity of the normal and tangential components of the magnetic field.

The behavior of a fluid in the presence of electromagnetic fields is governed to a large extent by the magnitude of the conductivity. For fluid at rest (4.57) reduces to the diffusion equation

$$\frac{\partial \mathbf{B}}{\partial t} = \frac{c^2}{4\pi\mu\sigma}\Delta\mathbf{B} \tag{4.61}$$

This means that an initial configuration of magnetic field will decay with typical diffusion time

$$\tau = \frac{4\pi\mu\sigma L^2}{c^2},$$

where L is a characteristic length of the spatial variation of $\mathbf{B}$. Despite being good enough conductors, most of liquid metals including mercury are characterized by small diffusion times (33 microseconds for a mercury droplet of 1 cm radius) compared to some solid conductors (1 sec for a copper sphere of 1 cm radius). Therefore the magnetic field penetration in such liquid conductors can be considered as an instantaneous process.

Another crucial phenomena for MHD flows of compressible conducting fluids is the propagation of Alfven waves. For mercury at room temperature the Alfven velocity

$$\mathbf{v}_A = \frac{\mathbf{B}_0}{\sqrt{4\pi\rho_0}},$$

where $\mathbf{B}_0$ and ρ_0 are unperturbed (mean) values of the magnetic induction and density of the fluid, respectively, is $[B_0(\text{Gauss})/13.1]$ cm/sec. This is a small number compared with the speed of sound of 1.45×10^5 cm/sec even for the magnetic field of 20 T. In many cases, however, it is not desirable to compute Alfven waves explicitly in the system. If, in addition, both the magnetic field diffusion time and the eddy current induced magnetic field are small, an assumption of the constant in time magnetic field can be made. The current density distribution can be obtained in this case using Ohm's law

$$\mathbf{J} = \sigma\left(-\text{grad}\phi + \frac{1}{c}\mathbf{u}\times\mathbf{B}\right). \tag{4.62}$$

Here ϕ is the electric field potential. The potential ϕ satisfies the following Poisson equation

$$\Delta\phi = \frac{1}{c}\text{div}(\mathbf{u}\times\mathbf{B}), \tag{4.63}$$

and the Neumann boundary conditions

$$\left.\frac{\partial\phi}{\partial\mathbf{n}}\right|_\Gamma = \frac{1}{c}(\mathbf{u}\times\mathbf{B})\cdot\mathbf{n},$$

where $\mathbf{n}$ is a normal vector at the fluid boundary Γ. This approach is applicable for the study of a liquid metal jet moving in a magnetic field.

We shall use also the following simplification for the modeling of a thin jet moving along the solenoid axis. Let us consider a ring of liquid metal of radius r that is inside a thin jet moving with velocity u_z along the axis of a solenoid magnet. The magnetic flux $\Phi = \pi r^2 B_z$ through the ring varies with time because the ring is moving through the spatially varying magnetic field,

and because the radius of the ring is varying at rate $u_r = dr/dt$. Therefore, an azimuthal electric field is induced around the ring:

$$2\pi r E_\phi = -\frac{1}{c}\frac{d\Phi}{dt} = -\frac{\pi r^2}{c}\frac{dB_z}{dt} - \frac{2\pi r u_r B_z}{c} = -\frac{\pi r^2 u_z}{c}\frac{\partial B_z}{\partial z} - \frac{2\pi r u_r B_z}{c}.$$

This electric field leads to an azimuthal current density

$$J_\phi = \sigma E_\phi = -\frac{\sigma r u_z}{2c}\frac{\partial B_z}{\partial z} - \frac{\sigma u_r B_z}{c}, \tag{4.64}$$

which defines the Lorentz force in the momentum equation (4.55) and leads to the distortion of the jet moving in a non-uniform magnetic field.

The linear stability analysis of thin conducting liquid jets moving along the axis of a uniform magnetic field [1] and the corresponding analysis for the Muon Collider target [7] show that an axial uniform field tends to stabilize the jet surface. The influence of a strong nonuniform field must be studied by means of the numerical simulation.

4.2.2 Numerical Implementation

In this section, we shall describe numerical ideas implemented in the FronTier MHD code. FronTier represents interfaces as lower dimensional meshes moving through a volume filling grid [5]. The traditional volume filling finite difference grid supports smooth solutions located in the region between interfaces. The location of the discontinuity and the jump in the solution variables are defined on the lower dimensional grid or interface. The dynamics of the interface comes from the mathematical theory of Riemann solutions, which is an idealized solution of a single jump discontinuity for a conservation law. Where surfaces intersect in lower dimensional objects (curves in three dimensions), the dynamics is defined by a theory of higher dimensional Riemann problems such as the theory of shock polars in gas dynamics. Nonlocal correlations to these idealized Riemann solutions provide the coupling between the values on these two grid systems.

The computation of a dynamically evolving interface requires the ability to detect and resolve changes in the topology of the moving front. A valid interface is one where each surface and curve is connected, surfaces only intersect along curves and curves only intersect at points. We say that such

an interface is untangled. Two independent numerical algorithms, grid-based tracking and grid-free tracking, were developed [5, 6] to resolve the untangling problem for the moving interface. The advantages and deficiencies of the two methods are complementary and an improved algorithm combining them into a single hybrid method was implemented in the FronTier code and described in [6].

We solve the hyperbolic subsystem of the MHD equations, namely the equations (4.54-4.56), on a finite difference grid in both domains separated by the free surface using FronTier's interface tracking numerical techniques. Some features of the FronTier hyperbolic solvers include the use of high resolution methods such as MUSCL, Godunov and Lax-Wendroff with a large selection of Riemann solvers such as the exact Riemann solver, the Colella-Glaz approximate Riemann solver, the linear US/UP fit (Dukowich) Riemann solver, and the Gamma law fit. We use realistic models for the equation of state such as the polytropic and stiffened polytropic equation of state, the Gruneisen equation of state, and the SESAME tabular equation of state.

The evolution of the free fluid surface is obtained through the solution of the Riemann problem for compressible fluids [5, 13]. Notice that since we are primarily interested in the contact discontinuity propagation, we do not consider the Riemann problem for the MHD system and therefore neglect elementary waves typical for MHD Riemann solutions.

We have developed the following numerical approaches for solving the equation (4.57) for the magnetic field evolution and the Poisson equation (4.63):

Finite difference solvers based on regular grids. We have developed a parallel elliptic solver for the current density distribution equation (refeq10) based on finite difference technique on rectangular grid in regular domains. We have performed smoothening of discontinuities of physics fields and applied the cubic spline interpolation of the fields within several grid blocks. The corresponding parallel iterative solvers for linear systems of equations explore different Krylov subspace and preconditioning methods and are based on PETSC libraries [14]. The solver is very effective for modeling multifluid MHD phenomena for fluids with smooth interfaces without small length scale perturbations. For MHD flows with unstable interfaces, we use FE solvers on meshes dynamically conforming to evolving interfaces.

Finite element solvers. Finite element solvers are based on grids dynamically conforming to the moving interface. The grid generation method is based on the point-shifted grid technique of McBryan [12]. For the elliptic

and parabolic systems considered here we favor the mixed-hybrid finite element formulation of Chavent and Jaffre [2]. We utilize Glowinski-Wheeler domain decomposition [8]. The linear systems obtained for the subdomain "interior problems" are solved using direct methods which preconditioned conjugate gradients for the global "wire basket" problem. Preconditioners such as vector probing and balancing are used.

4.2.3 Modeling Thermodynamics Properties of Fluids

Material properties strongly influence the structure and dynamics of waves in any continuous mechanical system. In particular, elementary waves in compressible fluids defined by Riemann problems depend both quantitatively and qualitatively on the property of an EOS.

SESAME equation of state for mercury. To model accurately the interaction of the mercury target with proton pulses, we created a tabulated equation of state for mercury in a wide temperature - pressure domain which includes the liquid-vapor phase transition and the critical point. The FronTier code uses SESAME Equation-of-Setate Library [9], developed at Los Alamos National Laboratory, to work with such tabulated EOS format. Necessary data describing thermodynamic properties of mercury were obtained courtesy of T. Trucano of Sandia National Laboratory. The behavior of isotherms of the specific internal energy, pressure and entropy of mercury obtained using this equation of state are shown in Figures 4.12 - 4.14. The computational domain included the two phase region for mercury and the critical point.

Isentropic EOS for cavitation flows. The tabulated EOS model allows an accurate description of equilibrium thermodynamic processes in mercury. However processes which occur in the mercury jet interacting with proton pulses go beyond the assumptions of equilibrium thermodynamics. Namely a regions of negative pressure (liquid tension) appear during the interaction which lead to the formation of cavities. To resolve such problem of negative pressures, we have developed an analytic two phase EOS model for an isentropic regime of the flow. The model is based on the polytropic EOS for the gas phase, the stiffened polytropic EOS for the liquid phase [13] and the following EOS type model (pressure - density relation):

$$P = P_l^{sat} + P_{gl} \log \left[\frac{\rho_g a_g^2 (\rho_l + \alpha(\rho_g - \rho_l))}{\rho_l (\rho_g a_g^2 - \alpha(\rho_g a_g^2 - \rho_l a_l^2))} \right], \tag{4.65}$$

fact
Muon Collaboration

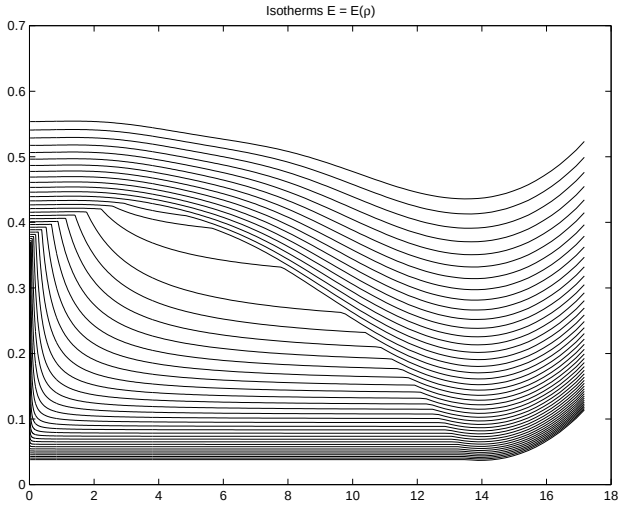

Figure 4.12:]
Isotherms of mercury specific internal energy as a function of density in the mixed liquid - vapor domain.

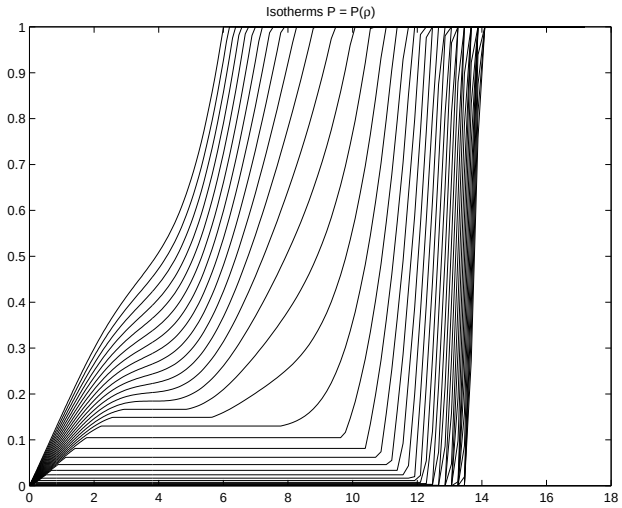

Figure 4.13: Isotherms of mercury pressure as a function of density in the mixed liquid - vapor domain.

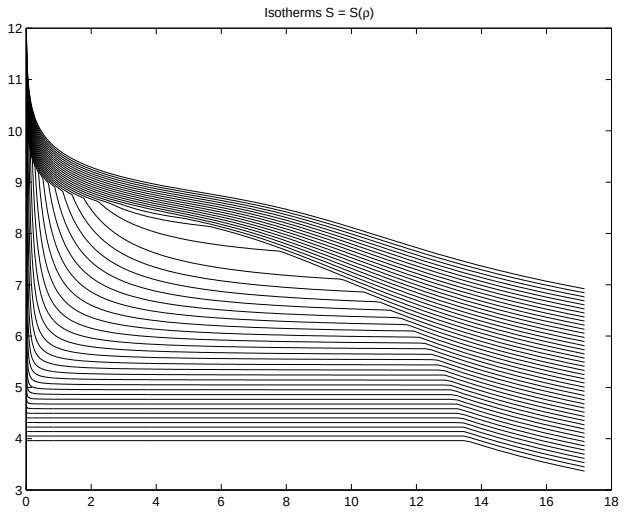

Figure 4.14: Isotherms of mercury entropy as a function of density in the mixed liquid - vapor domain.

where

$$P_{gl} = \frac{\rho_g a_g^2 \rho_l a_l^2 (\rho_g - \rho_l)}{\rho_g^2 a_g^2 - \rho_l^2 a_l^2},$$

Here ρ_g, p_g, a_g, ρ_l, p_l, a_l are the density, pressure, and sound speed of the saturated gas and liquid respectively, and the void fraction α is

$$\alpha = \frac{\rho - \rho_l}{\rho_g - \rho_l}.$$

We have developed the corresponding software library for FronTier.

4.2.4 Numerical Simulation Results

MHD studies of the Muon Collider target We shall present here numerical simulation results of thin jets of conducting fluid moving in highly nonuniform magnetic fields. In this numerical experiment, a 1 cm radius liquid jet is sent into a 20 T solenoid with the velocity 90 m/sec along the solenoid axis. The density of the liquid is $1\,g/cm^3$, the electric conductivity is 10^{16} in Gaussian units, and the initial pressure in the liquid is 1 atm. The electrically and magnetically neutral gas outside the jet has density 0.01 g/cm and the same initial pressure. The thermodynamic properties of the ambient gas were

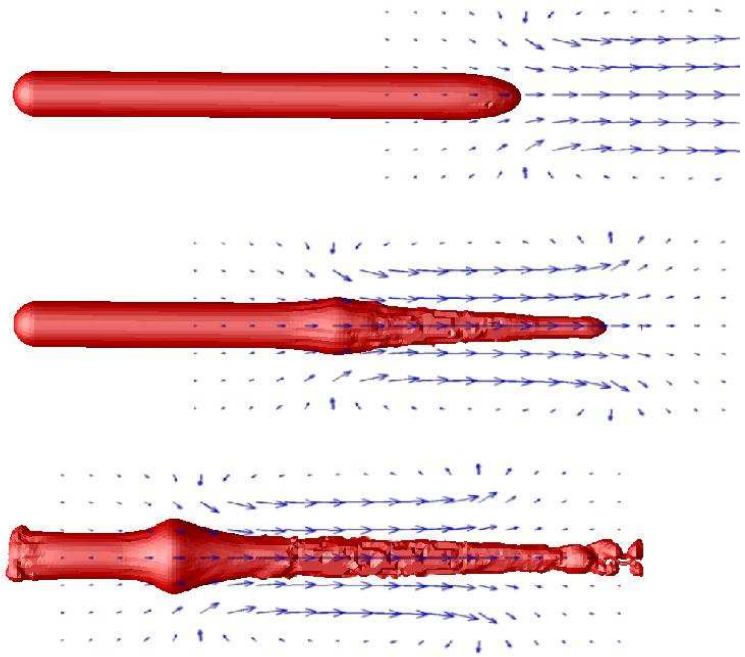

Figure 4.15: Liquid metal jet in a 20 T solenoid.

modeled using the polytropic equation of state [4] with the ratio of specific heat $\gamma = 1.4$ and the ideal gas constant $R = 1$. The properties of the liquid jet were modeled using the stiffened polytropic equation of state with the Gruneisen exponent = 5 and the stiffened gas constant $P_\infty = 3{\cdot}10^9 g/(cm{\cdot}sec^2)$. The field of a magnetic coil of rectangular profile and $8 \times 8 \times 20$ cm size was calculated using exact analytical expressions.

A set of images describing the evolution of the liquid jet as it enters and leaves the solenoid is depicted in Figure 4.15. The strong nonuniform magnetic field near the solenoid entrance squeezes and distorts the jet. The magnetic field outside the solenoid stretches the jet which results in the jet breakup. Notice that these simulations use the expression for the current density distribution (4.64) which looses the quantitative accuracy when the jet is close to the breakup. Numerical results obtained using accurate numerical solutions of equation (4.63) are given below.

The numerical simulation demonstrates the influence of strong magnetic field gradients on the jet distortion. To avoid such instabilities of the mercury

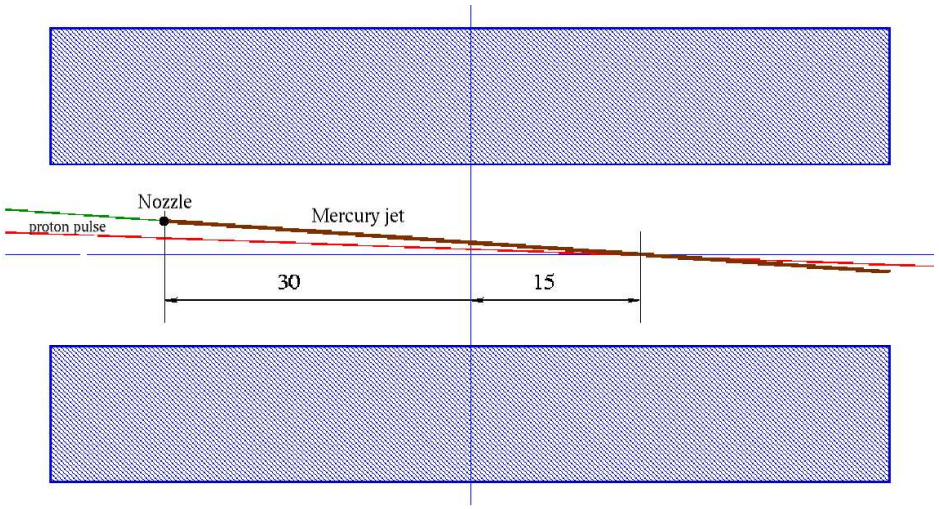

Figure 4.16: Schematic of the Muon Collider magnet.

target during its propagation in a 20 T magnetic field, the nozzle of the mercury target was placed inside the main 20 T resistive magnetic coil (see Figure 4.16). Therefore the jet will not meet strong magnetic field gradients before the interaction with the proton pulses.

We have performed numerical simulations of an off-axial mercury jet moving in 20T, 15T, and 10T solenoids using accurate numerical solution for the current density distribution (see Figures 4.18 – 4.20). Our results show that the magnetic field influence will not lead to significant jet deformations. Currently, the jet is not modeled as coming form the nozzle but is initialized as a long cylinder (see Figure 4.17). The perturbation of the tail part of the jet (Figure 4.18) is caused by the nonuniform field behind the solenoid.

Interaction of mercury jet with proton pulses

Numerical simulations presented in this section aid in understanding the behavior of the target under the influence of the proton pulse, and in estimating the evolution of the pressure waves and surface instabilities. We have neglected the influence of the external magnetic field on the hydrodynamic processes driven by the proton energy deposition.

The influence of the proton pulse was modeled by adding the proton energy density distribution to the internal energy density of mercury at a single time step. The value and spatial distribution of the proton energy was calculated using the MARS code [15]. The stiffened polytropic EOS

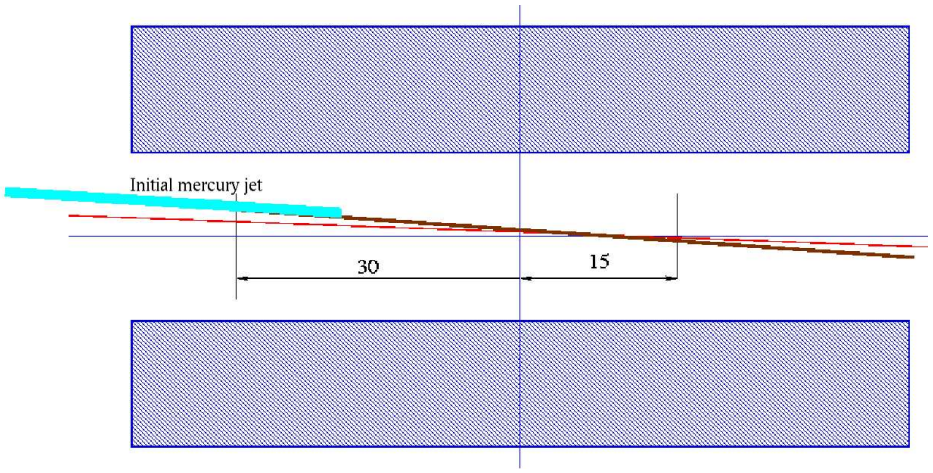

Figure 4.17: Initialization of the mercury jet.

Figure 4.18: Evolution of the mercury target in 20T solenoid

Figure 4.19: Evolution of the mercury target in 15T solenoid

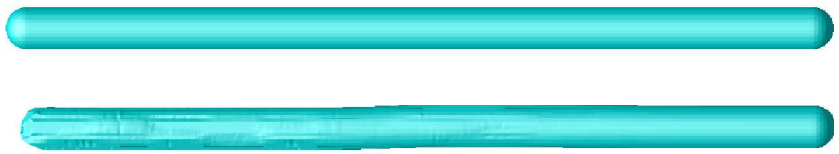

Figure 4.20: Evolution of the mercury target in 10T solenoid

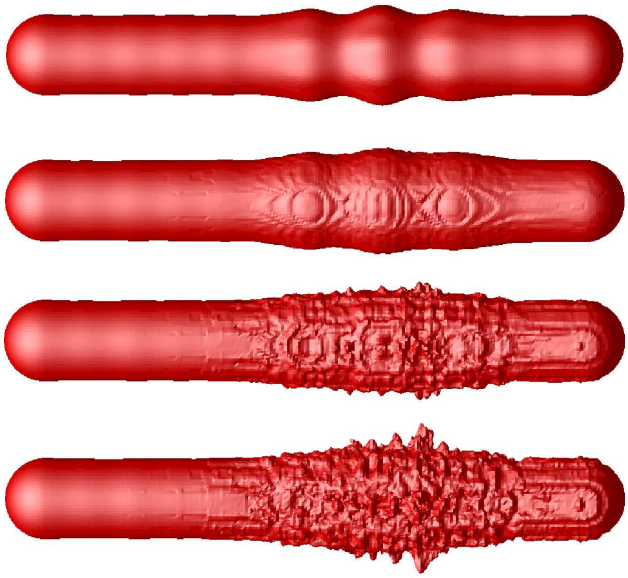

Figure 4.21: Evolution of the target driven by the proton energy deposition. Snapshots are shown at the initial time and at 27 mksec, 78 mksec, and 120 mksec.

model was used for these calculations with coefficients calculated using the tabulated EOS for mercury.

The evolution of the mercury target during 120 mks due to the interaction with a proton pulse is shown in Figure 4.21. Simulations show that velocities of surface instabilities are in the range 20 - 60 m/sec. The pressure field inside the jet developed small regions of negative pressure which indicates a possibility for the formation of cavities. Detailed studies of the cavitation phenomena in such a target will be done using the developed two-phase equation of state for mercury.

4.3 Proposed Research

In the future, we propose the following research:

- Improve the robustness of the dynamic grid generator and implement new elliptic/hyperbolic solvers.
- Develop a general analytic EOS for cavitation flows.
- Numerical simulation of nozzle effects.

- Further studies of liquid metal jets in magnetic fields.

- Numerical simulation of the mercury target interacting with a high energy proton beam in the presence of a strong magnetic field.

- Numerical simulation of turbulent jets.

Bibliography

[1] Chandrasekhar, S.: Hydrodynamics and Hydrodynamic stability. Clarendon Press, Oxford (1961)

[2] G. Chavent and J. Jaffre, Mathematical Models and Finite Elements for Reservoir Simulation. North Holland, 1986.

[3] Chern, I.R., Glimm, J., McBryan, O., Plohr, B., Yaniv, S.: Front tracking for Gas Dynamics. J. Comp. Phys. **62** (1986) 83-110

[4] Courant, R., Friedrichs, K.: Supersonic Flows and Shock Waves. Interscience, New York (1948)

[5] Glimm, J., Grove, J.W., Li, X.L., Shyue, K.M., Zhang, Q., Zeng, Y.: Three dimensional front tracking. SIAM J. Sci. Comp. **19** (1998) 703-727

[6] Glimm, J., Grove, J.W., Li, X.L., Tan, D.: Robust computational algorithms for dynamic interface tracking in three dimensions. Los Alamos National Laboratory Report LA-UR-99-1780

[7] Glimm, J., Kirk, H., Li, X.L., Pinezich, J., Samulyak, R., Simos, N.: Simulation of 3D fluid jets with application to the Muon Collider target design. Advances in Fluid Mechanics III (Editors: Rahman, M., Brebbia, C.), WIT Press, Southampton Boston (2000) 191 - 200

[8] Glowinski and M. Wheeler, Domain Decomposition and Mixed Finite Element Methods for Elliptic Problems. In R. Glowinski, G. Golub, G. Meurant, and J. Periaux, Eds., Proceedings of the First International Symposium on Domain Decomposition Methods for Partial Differential Equations, pp. 144-172. SIAM, Philadelphia, 1988.

[9] K. S. Holian, T-4 handbook of material properties data bases, Vol. 1c: Equations of state, Los Alamos Report LA-10160-MS, 1984.

[10] Kirk, H., et al.: Target studies with BNL E951 at the AGS. Particles and Accelerators 2001, June 18-22 (2001) Chicago IL

[11] Landau, L.D., Lifshitz, E.M.: Electrodynamics of Continuous Media. Addison - Wesley Publishing Co., Reading Massachusetts (1960)

[12] O. McBryan, Fluids, Discontinuities and Renormalization Group Methods. In Brittin, Gustafson, and Wyss, Eds., Mathematical Physics VII, pp. 481-494. North-Holland Publishing Company, Amsterdam, 1984.

[13] Menikoff, R., Plohr, B.: The Riemann problem for fluid flow of real materials. Rev. Mod. Phys. **61** (1989) 75-130

[14] S. Balay, W. Gropp, L. McInnes and B. Smith", PETSc Users Manual, ANL-95/11 - Revision 2.1.1, Argonne National Laboratory, 2001.

[15] Ozaki, S., Palmer, R., Zisman, M., Gallardo, J. (editors) Feasibility Study- II of a Muon-Based Neutrino Source. BNL-52623 June 2001; available at http://www.cap.bnl.gov/mumu/studyii/FS2-report.html

Chapter 5

Pulse Solenoid Concept

5.1 General Description of Magnet System

This report documents the conceptual design of a cryogenic pulse magnet to generate up to 14.5 T in a room temperature bore of 15 cm. The winding I.D., O.D. and length are 20 cm, 80 cm and 100 cm, respectively; the conductor is 3.6 metric tons (1,800 turns) of high-purity copper. Cooling of the magnet prior to each pulse is by helium gas or liquid nitrogen forced through axial channels in the magnet; recooling of the helium gas is by either liquid nitrogen or liquid hydrogen in a heat exchanger inherited from the SSC. To hasten cooldown of the magnet, it includes coolant channels not only at its inner and outer radius, but also at two intermediate radii.

At the outer of these radii (30 cm) is an additional current lead, to allow operation with the outermost coil omitted from the electrical circuit. The remaining magnet, of 60 cm O.D. and 1,200 turns, is appropriate for liquid-nitrogen operation; the full magnet has too high a resistance to reach full current unless cooled to less than 34 K. The option to energize just the 1,200-turn magnet enables a staged approach to the full-field mode of operation. One can postpone fabrication of the outermost coil until needed by the last of the three stages that we propose.

5.2 Three Proposed Stages: 5 T, 10 T & 14.5 T

Figure 5.2 graphs the field versus time for the three proposed modes of operation. Stage 1 employs the 1,200-turn magnet cooled to 87 K or less by liquid nitrogen at barely above atmospheric pressure (77-78 K). The power supply is one of many at BNL that is rated at 3.6 kiloamperes and 150 volts (540 kVA). At this voltage, the magnet takes about seven seconds to reach its full field of 5 T, which one holds for up to a second. Discharge at full negative voltage, -150 V, takes an additional three seconds.

Stage 2 employs the same 1,200-turn magnet, but energized by four BNL power supplies in series/parallel: 7.2 kA x 300 V = 2.16 MVA. The pulse is about 10% shorter than for Stage 1. Simultaneously doubling both the current and the voltage calls for a magnet of the same resistance at peak current as Stage 1. However, because of the fourfold increase in peak power, the magnet heats up nearly four times as much during each pulse; therefore, it must start from a lower temperature–no more than 75 K. To reach this

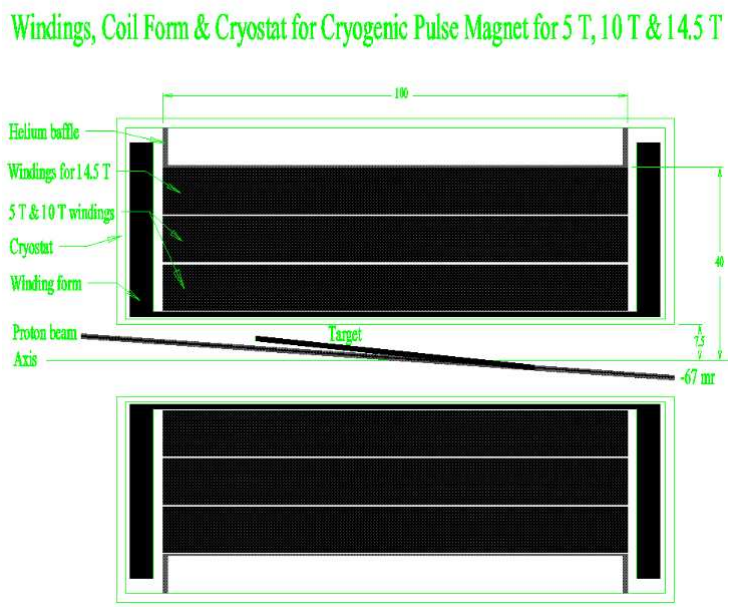

Figure 5.1: Cross section of Targetry magnet system: cryostat, magnet windings, target (mercury jet), and proton beam. The bore is 15 cm. The winding pack is of 100 cm length, 20 cm I.D., and 80 cm O.D. Channels for coolant separate the three subcoils, each of 10 cm radial depth.

temperature, one can employ evaporative cooling at reduced pressure to subcool the nitrogen to within a few degrees of its 64 K freezing point. BNL has roughing pumps ample to accomplish this. Cryogenic investments will be in hardware and engineering associated with the SSC heat exchanger and cryogen delivery systems. Investments in the power supply will be hardware and

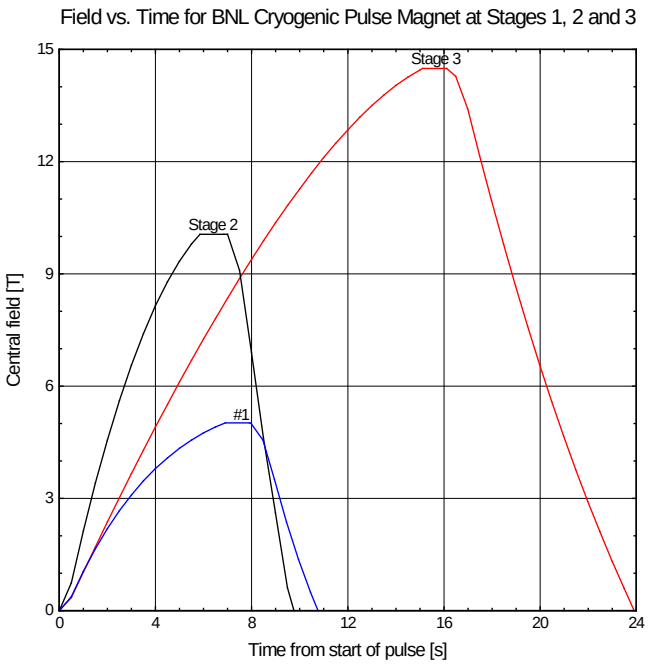

Figure 5.2: Field vs. time for cryogenic pulse magnet for BNL Targetry Experiment upon completion of each of three stages culminating in 14.5-tesla operation. Stage 1: 1,200 turns, 0.54 MVA; Stage 2: 1,200 turns, 2.16 MVA; Stage 3: 1,800 turns, 2.16 MVA.

software to ensure that its four 0.54 MVA modules share the load equally.

Stage 3 employs the same 2.16 MVA power supply as Stage 2, but now energizing all 1,800 turns. In order for the same 300 volts to suffice to drive full current through the much greater length of conductor, one must reduce its electrical resistivity by cooling it to 30 K with helium gas whose temperature

may be as low as 22 K. The heat sink is liquid hydrogen trucked to BNL from an industrial liquefaction plant. With $1\frac{1}{2}$ as many turns as Stage 2, Stage 3 generates 14.5 T instead of 10 T. The pulse is much longer than for the previous cases: 15 seconds to full field, a flat top of about a second, and eight seconds to return to zero, when driven down at -300 V.

Table I tabulates parameters of Stages 1, 2 and 3. The last two rows give the temperature rise and cumulative heating for a typical pulse, in which, after a one second flat top, the power supply ("two-quadrant," or "bipolar") discharges the coil with negative voltage of the same magnitude used to charge the magnet.

Table 5.1: Pulse Magnet Systems for E951 Targetry Experiment

	Stage 1	Stage 2	Stage 3
Peak on-axis field (T)	5.0	10.0	14.5
No. of 0.54 MVA power supplies	1	4	4
Mode of ganging supplies	None	2 x 2	2 x 2
Initial temperature (K)	84	74	30
Number of turns utilized	1200	1200	1800
Charge time (s)	7.2	6.2	15.2
Temperature rise at end of pulse (K)	6	21	48
Cumulative heating at end of pulse (MJ)	2.4	7.9	13.5

The remainder of this report supports the choice of magnet parameters of Table I. Each choice is to some extent subjective, involving judgment calls on the relative importance of costs and benefits. Of interest is the rate of change of each cost and benefit with a change in each magnet parameter. The following nine sections look at perturbations from a base-case design for each of the three stages of operation, examining the effects of just one or two parameters at a time.

5.2.1 How Long Should the Magnet Be?

An easy parameter to fix is that of magnet length, because the Targetry Experiment has a requirement for field homogeneity, which depends very strongly on magnet length and much less strongly on anything else. The field homogeneity is to limit the magnetohydrodynamic forces on the mercury jet target traversing the field; the field should be uniform to 10% over a length of 60 cm. Figure 5.3 reveals that the magnet should be about 100 cm long.

fact
Muon Collaboration

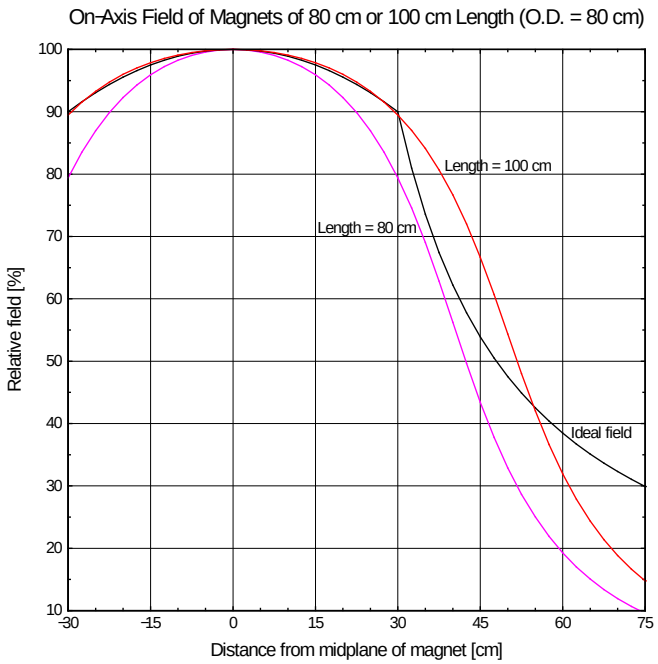

Figure 5.3: On-axis field profile of magnets of 80 cm outer diameter either 80 cm or 100 cm long. The longer magnet achieves the desired profile very well over the target, from -30 cm to +30 cm; the shorter magnet does not.

The *ideal field* in Fig. 5.3 is that which would retain quite well most of the pions captured in the 60 cm long target region, while transitioning to its much lower value in downstream components of a neutrino factory or muon collider. The field ramps downward by a factor of sixteen over a length of three meters from the end of the target region, while the magnet bore increases by a factor of four. This field profile would allow one to test downstream components,

such a radio-frequency cavity, in the intense shower of particles emanating from the target. Unfortunately, given the present budgetary climate, the Targetry Experiment cannot afford to build these downstream components, nor the more elaborate, expensive, and power-consumptive magnet in which to test them. Therefore, it is irrelevant that beyond the target region neither of the above field profiles matches very well the ideal field.

5.2.2 How much does electrical conductivity improve at low temperature?

The motivation to cryogenically cool any magnet, pulsed or not, is to improve the electrical conductivity of its conductor. Figure 5.4 shows that the resistivity of high-purity copper declines greatly from room temperature down to 30 K. The incentive to operate at cryogenic temperatures is great indeed. Cooling to 80 K (with liquid nitrogen at atmospheric pressure) improves the electrical conductivity by a factor of nearly seven. Cooling to 66 K (with liquid nitrogen subcooled to nearly its freezing point of 64 K) gives a ratio of about ten. Cooling to 30 K (with liquid hydrogen as the heat sink, for example) can achieve a ratio of about 30.

There is very little motivation to cool the conductor still further; one has entered a regime of diminishing returns. Figure 5.5 illustrates two of the reasons for this. One reason is that electrical resistivity improves rather little. This is true even for copper that is exceedingly pure, unless it is so completely annealed as to be too weak for a very high field magnet. The other reason is that, if the copper is uncooled, with only its heat capacity to limit its temperature rise, it will heat up very rapidly, because its heat capacity plummets, approximately as T3, below 30 K. The heating rate, proportional to r/C_p, is three times worse at 20 K than at 30 K.

5.2.3 How Beneficial is Cryogenic Operation?

With the maximum magnet power, 2.16 MVA, deliverable at the targetry site, a Stage 3 targetry magnet could generate only about 4 T if operated at room temperature. Figure 5.6 shows that even precooling to the magnet to 80 K fails to deliver sufficient field intensity to duplicate the 14-15 T desirable for a neutrino factory of muon collider. To achieve this field, one needs to precool the targetry magnet to about 30 K.

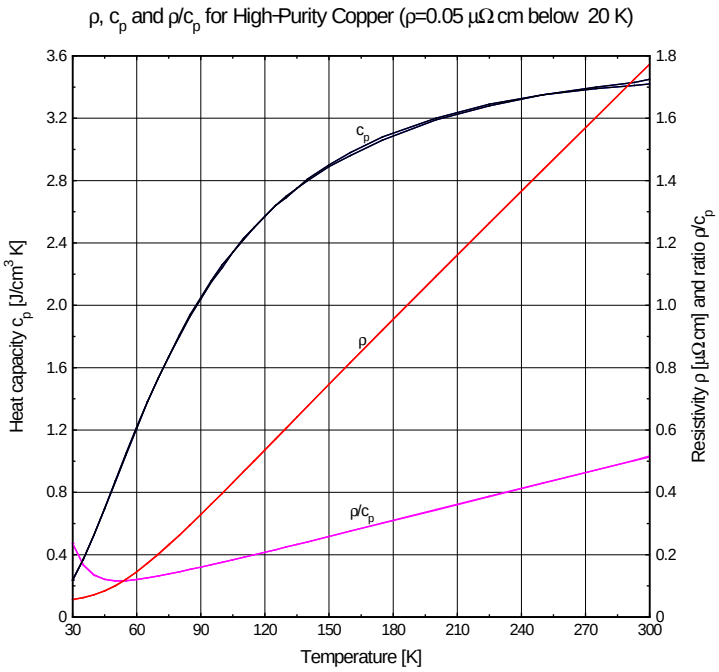

Figure 5.4: Electrical resistivity ρ, heat capacity C_p, and ratio ρ/C_p between room temperature and 30 K, for copper with a residual resistivity of 0.05 $\mu\Omega$cm below 20 K.

The field-versus-temperature predictions of Fig. 5.6 (and all the other relevant figures in this report) acknowledge that electrical resistivity depends not only on temperature, as shown in Fig. 5.5, but also on magnetic field. This magnetoresistance can significantly degrade electrical conductivity at very low temperatures.

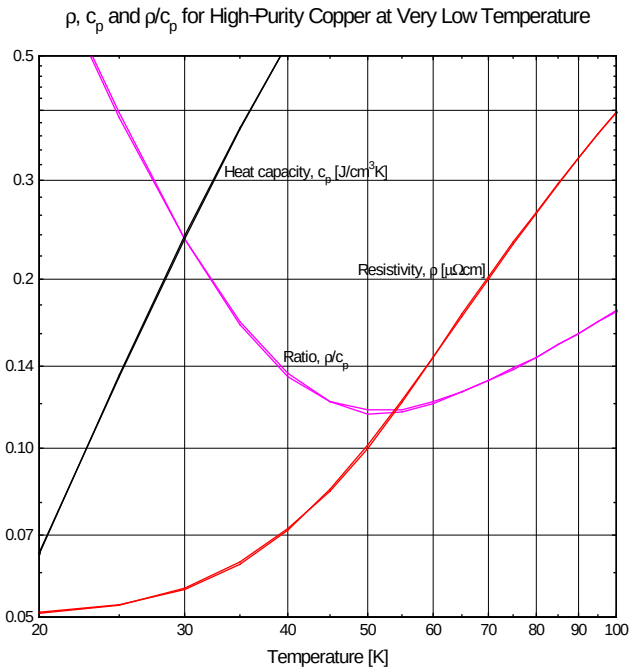

Figure 5.5: Low-temperature electrical resistivity ρ (in zero magnetic field), heat capacity C_p, and ratio ρ/C_p for copper with a residual resistivity of 0.05 $\mu\Omega$cm below 20 K.

5.2.4 How detrimental is magnetoresistance?

Magnetoresistance can be severe at low temperatures and high fields. It becomes ever more significant at low temperature. Figure 5.7 graphs, as a function of temperature and magnetic field, the electrical resistivity of copper with a residual resistivity of 0.05 $\mu\Omega$cm. Note that at 20 K the magnetoresistance at 20 T nearly triples the resistivity at zero field. Even at fields that

fact
Muon Collaboration

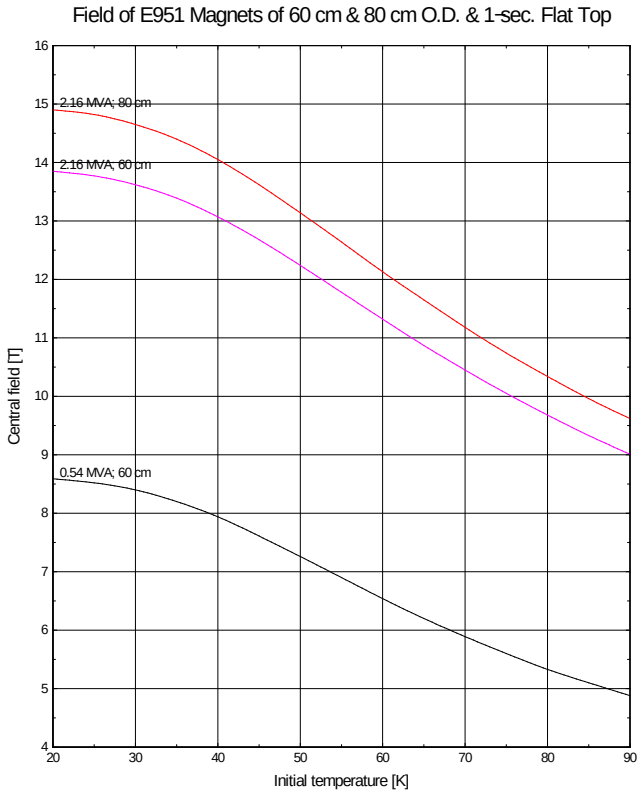

Figure 5.6: Field vs. initial temperature of cryogenic pulse magnets of 100 cm length, 20 cm I.D. and either 60 cm or 80 cm O.D.

are more modest and temperatures that are less frigid, magnetoresistance is non-negligible. At 10 T and 100 K, the effect is about 13%.

5.2.5 What does a typical pulse look like?

Figure 5.8 graphs the time dependence of some of the more important parameters of the highest field (Stage 3) pulse magnet for the Targetry Experiment.

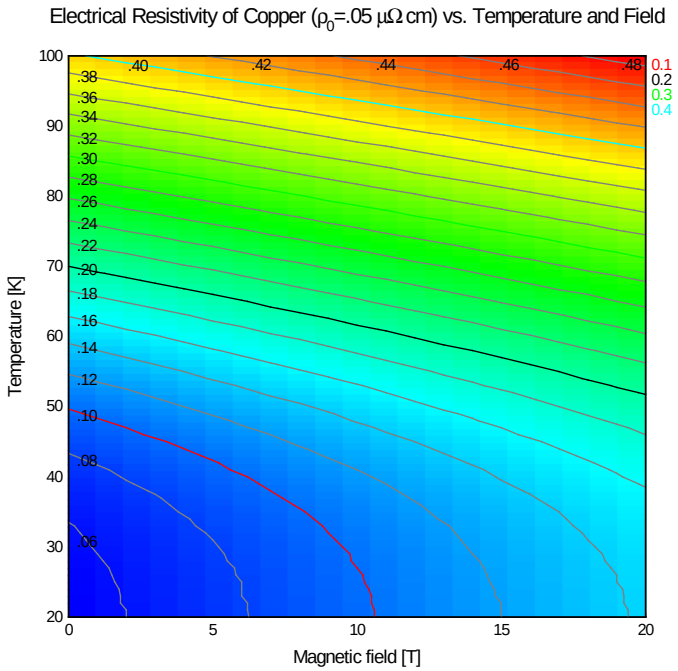

Figure 5.7: Electrical resistivity versus temperature from 20 K to 100 K and magnetic fields from zero to 20 T.

Note that the resistance increases by a factor of about $3\frac{1}{2}$ during the pulse. The slight decline in resistance during the last several seconds of the pulse is because the magnetoresistance is decreasing faster with the decreasing field than the zero-field resistance is increasing from the still-increasing temperature.

Note also that the peak resistive voltage of the magnet, when pulsed from this temperature, is about 240 V–*i.e.*, about 80% of the full voltage available

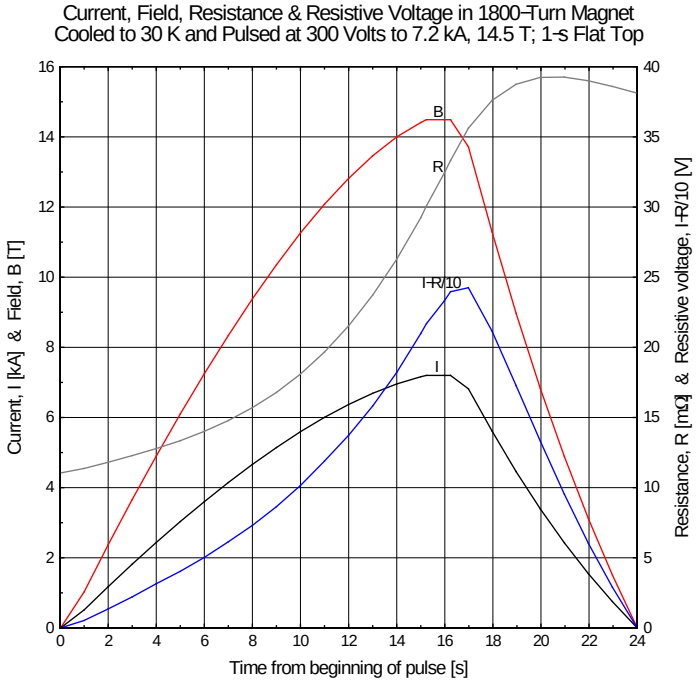

Figure 5.8: Current, magnet resistance and power supply voltage of Stage 3 pulse magnet for targetry experiment.

from the power supply. To obtain the flat top to the field requires the power supply voltage instantly to drop to 240 V from 300 V, because the inductive back voltage abruptly has dropped to zero. Then, for the duration of the flat top (shown here as one second), the voltage must increase several percent to track the increase in resistance as the windings heat up. Full negative voltage drives the current to zero.

5.2.6 How should one discharge the magnet?

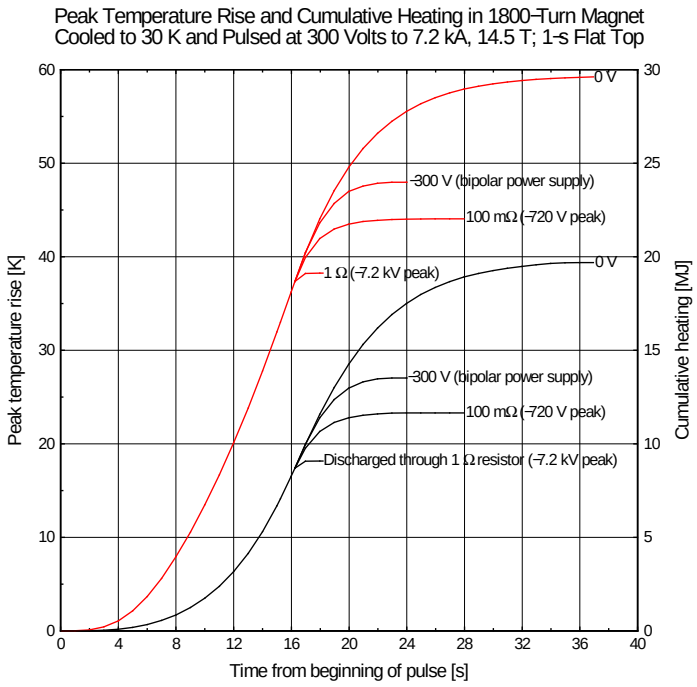

Figure 5.9: Peak temperature rise and cumulative heating in cryogenic pulse magnets of 20 cm I.D., 80 cm O.D., and 100 cm length. Left-hand curves: peak temperature rise; right-hand curves: cumulative heating.

Figure 5.9 graphs, as a function of time, the temperature rise and cumulative heating at the end of each field pulse of the Stage 3 magnet when discharged in any of four ways. One way is that of a typical pulse, in which one drives the current down with reverse voltage of the same magnitude used to charge the coil. Driving the current down, from a flat top of one second,

limits the peak temperature rise to 48 K and the heating to 13 MJ. Another way is with the current coasting down, dissipating in the magnet all of the magnetic energy that it stored. This would occur if the power supply tripped out at the end of the flat top, and therefore did not deliver the reverse voltage expected from it. The windings must absorb all, instead of just a part of, the magnetic energy stored in the coil. The additional 6 MJ leads to a total temperature rise of nearly 60 K. This is still a very comfortable value from the standpoint of thermal stresses, but the magnet will take longer to recool.

The other two modes of discharge employ an external resistor. A 100 mΩ resistor, implying a peak discharge voltage of -720 V, gives an energy dissipation and temperature rise roughly equivalent to that when discharged through the power supply at a constant voltage of -300. With a 1 Ω resistor (-7.2 kV peak discharge voltage), the energy dissipation and temperature rise are about 9 MJ and 38 K, respectively. At such a high discharge voltage, the external resistor absorbs nearly all the magnetic energy stored in the magnet.

5.2.7 How big in diameter should the magnet be?

Figure 5.9 reveals that to generate the very most field with a fixed power supply calls for a targetry magnet with an outer diameter of about one meter, irrespective of the power level or initial temperature. Note, however, that the maximum of each curve is very broad. Well before one has reached a diameter as large as a meter, the increase in field becomes too gradual to justify the rapid increase in conductor mass and cost. Already at an outer diameter of 80 cm, the conductor mass has risen to 3.6 metric tons. Increasing the outer diameter to one meter would require 60% more conductor, for less than a 3% increase in field.

An additional reason for limiting the outer diameter of the targetry magnet is to limit the heat that one must remove after each pulse. Figure 5.12 shows that the cumulative heating increases rapidly with diameter. For example, doubling the diameter approximately triples the cumulative heating, tripling the recool time in any system that is limited by the mass flow of coolant. This consideration, like the one concerning conductor mass and cost, favors magnets no larger than 80 cm in diameter.

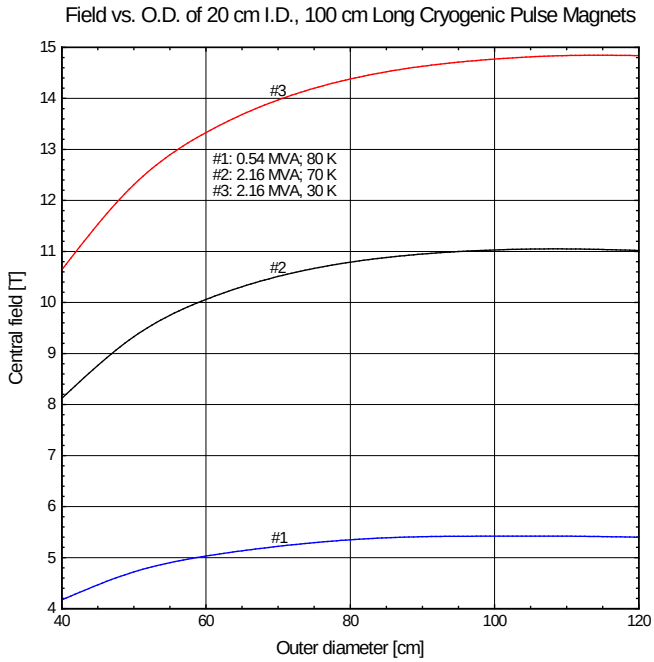

Figure 5.10: Central field vs. outer diameter of cryogenic pulse magnets of 20 cm inner diameter and 100 cm length.

5.2.8 How warm does the conductor get?

Figure 5.12 plots temperature contours for the Stage 3 magnet pulsed to full field (with a flat top of $\frac{1}{2}$ s.) from a uniform initial temperature of 30 K. The resulting temperature is highest, 76 K, at the inner radius of the magnet midplane (r = 10 cm, z = 0), where magnetoresistance adds most to the resistivity, and therefore the heating rate. Near the kernel, where the field and magnetoresistance are zero, the maximum temperature is only 62 K.

fact
Muon Collaboration

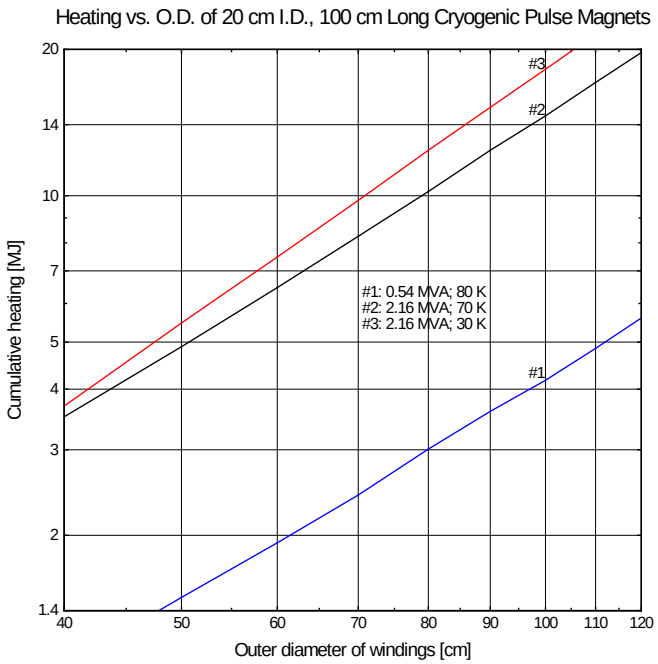

Figure 5.11: Cumulative heating vs. outer diameter of cryogenic pulse magnet of 20 cm inner diameter and 100 cm length.

For comparison, Fig. 5.13 plots temperature contours for the Stage 3 magnet pulsed to full field (again with a flat top of $\frac{1}{2}$ s.)from an initial temperature with the same average as before, 30 K, but with a distribution suggestive of that in a magnet pulsed to full field and then recooled too briefly for temperatures to equilibrate. The peak temperature, coincidentally, is the same, 76 K, as when energized from a uniform temperature, but occurs at a different radius, 14 cm, where the initial temperature was high. At r = 10

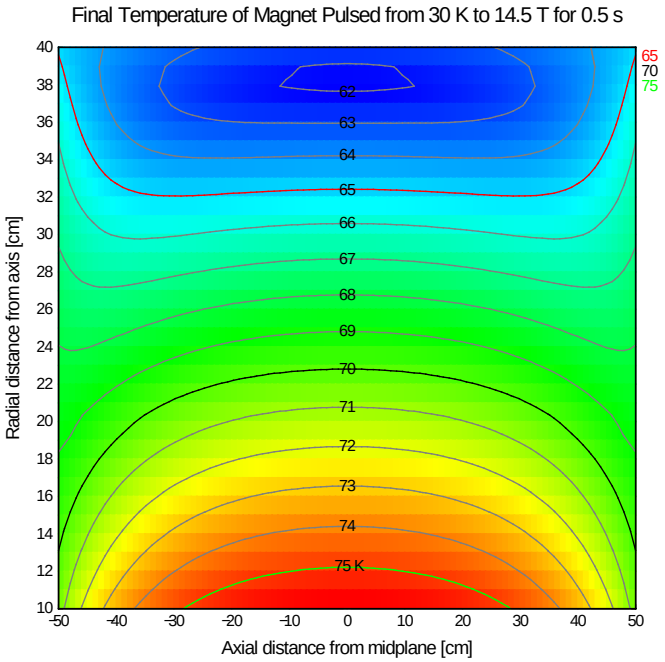

Figure 5.12: Temperature at end of pulse of Stage 3 magnet energized to 7,200 A, 14.5 T (with a half-second flat top) from an initial uniform temperature of 30 K.

cm the peak temperature is less than 75 K, despite the magnetoresistance being greatest there, because the initial temperature was only 22 K.

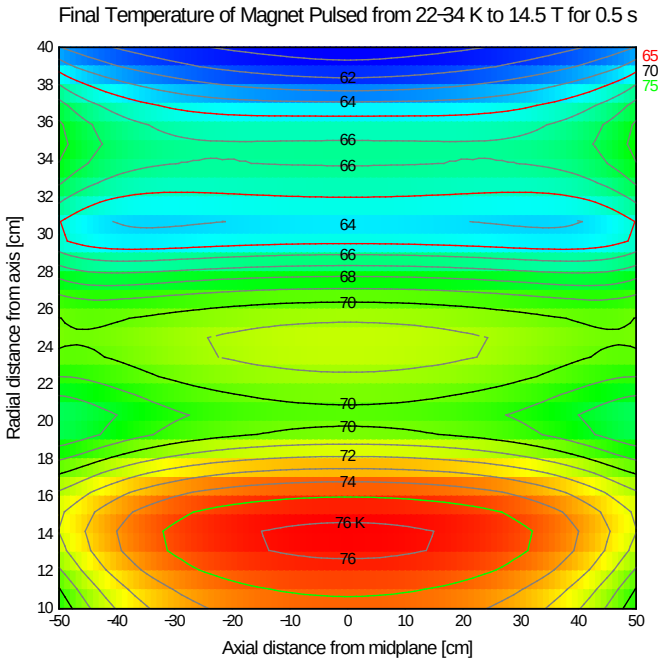

Figure 5.13: Temperature distribution in Stage 3 magnet if energized from an illustrative non-uniform temperature: 34 K at radii of 15 cm, 25 cm and 35 cm, falling parabolically to 22 K at radii of 10 cm, 20 cm, 30 cm and 40 cm.

5.2.9 How do field and heating depend on initial temperature?

If one pulses a cryogenic magnet from too high a temperature, it will fail to reach its design current and, hence, its design field. Figure 5.14 shows that for the Stage 3 magnet, the critical temperature is 35 K. A magnet pulsed

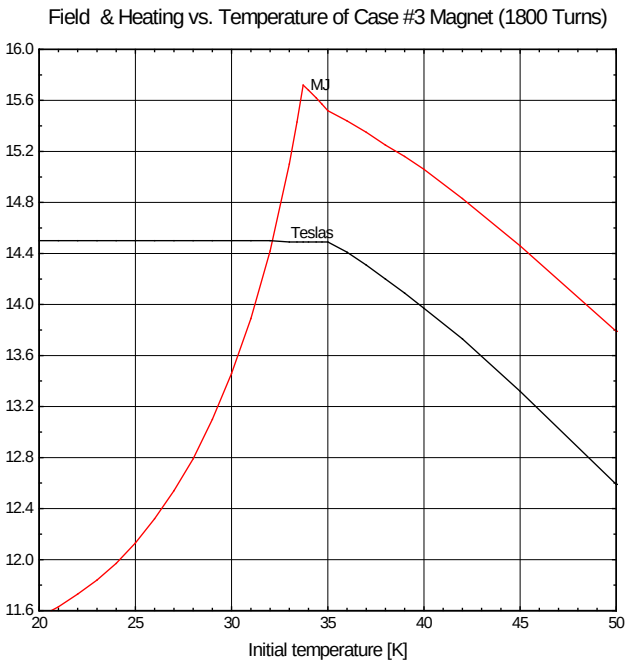

Figure 5.14: Field and cumulative heating in Stage 3 magnets of 100 cm length, 20 cm I.D., 80 cm O.D. and 1,800 turns, pulsed from an initial temperature of 20 K to 50 K.

from 40 K, for example, can generate only 14 T, instead of 14.5 T. Pulsing the magnet from any temperature lower than 35 K will not increase its field, because one runs out of current. However, one now has spare voltage with which to shape the pulse. For example, a magnet pulsed from 33.7 K not only can reach full field, but also can hold it for the desired one second. A further benefit is the reduction in dissipation, thereby improving the rep

rate of the magnet. Pulsing from 25 K instead of 30 K decreases by 10% the heat that one must remove. Relative to a magnet pulsed from 33.7 K, the improvement is 23%.

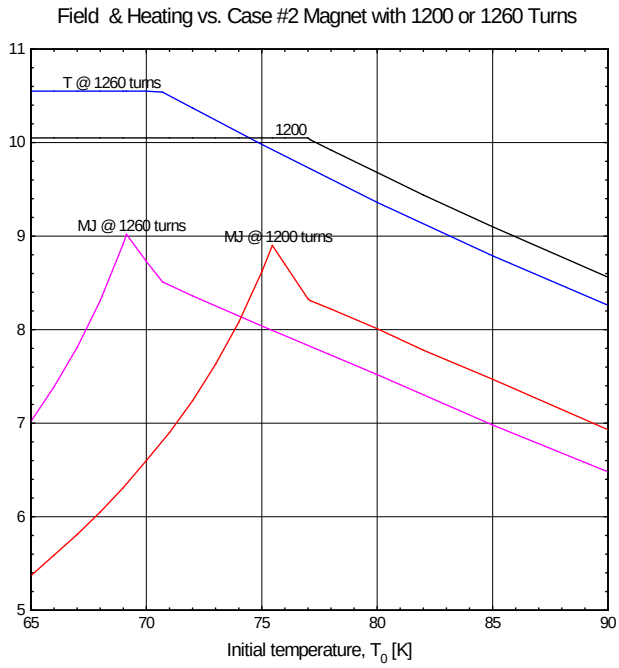

Figure 5.15: Central field and cumulative heating of Stage 2 magnet of 100 cm length, 20 cm I.D., 60 cm O.D. and 1,200 turns, pulsed from an initial temperature of 65 K to 90 K. Comparative magnet is of same dimensions but has 5% more turns.

Figure 5.15 plots data similar to that of Fig. 5.14, but now for the Stage 2 magnet, whose intended coolant is subcooled nitrogen. 75.5 K is the max-

imum temperature at which the magnet will generate full field with a flat top of one second. Cooled to 80 K (as with nitrogen that is not subcooled) limits the field to 9.6 T instead of 10 T and with no flat top field. Cooled to 66 K, the minimum likely with subcooled nitrogen, reduces the cumulative dissipation to 5.6 MJ, an improvement of 37% relative to 75.5 K operation. The comparison magnet, with 5% more turns, will generate 5% more field at any temperature below 69 K, but at the price of significantly more heating. For example, at 66 K its cumulative heating is 7.4 MJ, one third more than for the magnet with 1,200 turns.

Figure 5.16 presents data as in the previous two graphs, but now for variants on the Stage 1 magnet, whose intended coolant is liquid nitrogen at atmospheric pressure. A magnet with 1,200 turns generates full field, complete with a flat top of one second, at all temperatures below 87.4 K. This temperature is so far above that of liquid nitrogen that cooldown should be rapid, if governed by heat transfer to the coolant. However, if cooldown is limited by mass flow through the coolant channels, then operation from a lower temperature may be superior. Pulsed from 80 K, the magnet dissipates 37% less heat–only 1.94 instead of 3.08 MJ. One may even wish to subcool the nitrogen. Cooled to 66 K, the magnet dissipates only 1.13 MJ, 42% less than at 80 K. The two comparison magnets, with 5% and 10% more turns, respectively, generate correspondingly more field, but with substantially narrower temperature ranges of operation and higher dissipations at any given temperature. These considerations, plus the convenience of making a single magnet suffice for both Stages 1 and 2, make the 1,200 turn magnet the compelling choice.

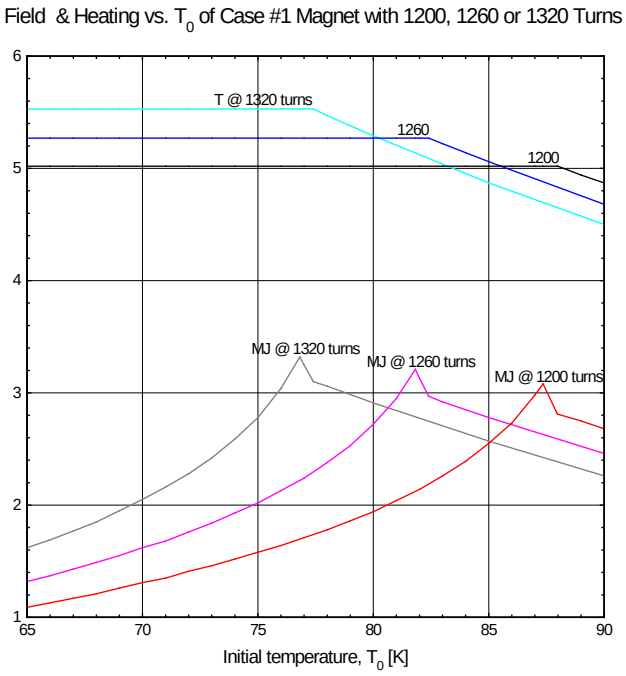

Figure 5.16: Central field and cumulative heating for Stage 1 magnet and comparative magnets with 5% and 10% more turns, each pulsed from an initial temperature of 65 K to 90 K.

Chapter 6

Engineering

6.1 Mechanical Design

A three segment, layer wound solenoid is proposed for the pulsed magnet. The conductor is half inch square, cold worked OFHC copper. The coil is inertially cooled with options for liquid nitrogen or gaseous helium cooling between shots. Coolant flows through axial channels in the coil. The coil will be epoxy impregnated. Wound coils of this small radius, using cold worked conductor, retain internal elastic stresses from the winding process, and if not impregnated, require elaborate clamping mechanisms to have the coil retain it's shape.

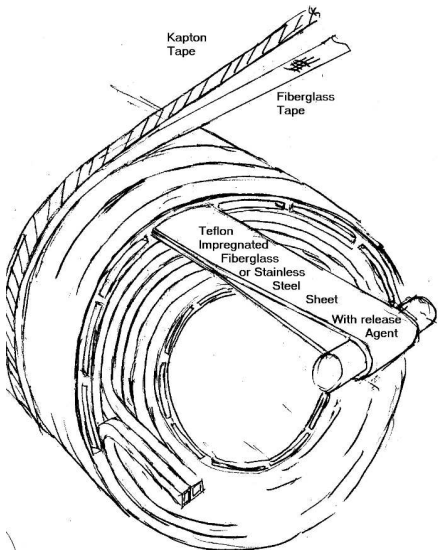

Figure 6.1: need caption here

Dual operational modes require special design of the cryostat/helium can. This is discussed in the section on cooldown behavior. Insulation design impacts the conduction cooling behavior:

- Kapton is the limiting element in the thermal conduction through the coil.
- Kapton initially was expected to be wound around the conductor. This produced the equivalent of 5 mils of Kapton between layers.

Table 6.1: Proposed Operational Scenarios

Case No.	Peak Field (T)	Coolant	T after pulse (K)	T coolant (K)	Start Bulk Temp (K)
1	5	Helium Gas	90	66	84
1a	5	LN2	90	66	84
2	10	Helium Gas	96	66	74
2a	10	LN2	96	66	74
3	15	Helium Gas	78	22	30

- To improve conduction, Kapton is used only between the layers. Turn to turn voltage is lower than layer to layer. The turn to turn voltage is less than the rule of thumb for He breakdown voltage (1 volt/mil at 1 atmosphere) for the insulation thickness proposed. Note that the He operating pressure is expected to be 15 atmospheres, the pressures inside the epoxy winding pack may be substantially lower, depending on Helium diffusion, making the 1 atm breakdown voltage for the conductor, reasonable.

- The layer to layer voltage exceeds this rule of thumb, however, and would need the Kapton if there was an imperfection in the epoxy/glass insulation. Half laps of kapton and fiberglass, similar to the CS model coil will retain some structural integrity.

- Once a layer of conductor is wound, a layer of Kapton/glass would be wound on the completed layer of conductor. This produces the equivalent of 3 mils of Kapton rather than 5 if the conductor were wrapped individually. Every 6 to 8th layer some sort of preformed channel array would be layed on, then wrapped with glass/Kapton to hold it in place, and as the layer insulation for the next layer of conductors.

Experience with Alcator C-Mod indicates that for final magnet temperatures at or below 100K, the channels will not need "turbulators" or surface trips to break-up the film boiling layer. This will have to be reviewed during the design phase. If some form of surface roughness will be required in the 2mm channels, then the method of forming the channels with removable strips will have to be re-visited.

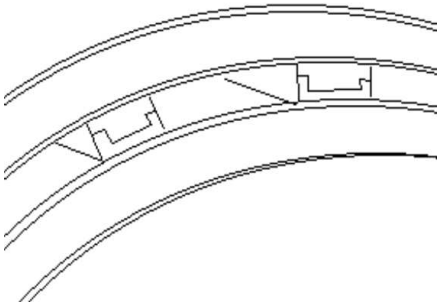

Figure 6.2: Ribs that form the channels may need to have sliding parting planes to allow axial and radial motion between coil segments.

6.2 Engineering Tasks

While the magnet has been conceptualized, with some analytic basis, detailed engineering will require additional work after the construction of the magnet is approved. These tasks are outlined below.

- Identify Voltages for All Operating Scenarios - Choose insulation systems. Determine where Kapton is used.
- Stress Analysis, Assess radial load on channel ligaments, consider operation with inner modules energized, and no current in outer module
- Confirm cooldown and pressure drop calculations
- Analyze thermal contraction/shock of channel - Avoid separation and loss of conduction
- Design He can for 15 atm. and vacuum operation.
- Design mandrel and flow plenums
- Cryostat Design. Is this a Vacuum Cryostat with LN2 Shield, or a Gaseous N2?

- Break-outs and Leads Penetration design - Design the required support to resist loads and torques that result from principally the end radial Field.
- Determine if Eddy Currents in He Can represent a significant load.
- Design Cryogenic Electrical Breaks
- Design Supports, Break-outs, He can and Cryostat to Allow Phased Construction

Some of the analytic work in support of the present design is now described:

6.3 Stress Analysis

The coil is stress analyzed using ANSYS. Fields and forces are computed using elliptic integrals in a code external to ANSYS. The model is axisymmetric. Figures 6.3 - 6.7 show a 3D representation from a symmetry expansion.

Table 6.2: Coil Build used in the Stress Analysis

Seg No.	r	z	dr	dz	nx	ny
1	0.15	0	0.098	1.0	16	16
channel	0.2	0	0.002	1.0	1	16
2	0.25	0	0.098	1.0	16	16
channel	0.3	0	0.002	1.0	1	16
3	0.35	0	0.098	1.0	16	16

For Fusion magnets the inner skin of the solenoid is allowed to reach the yield - Treating this stress as a bending stress with a 1.5*Sm allowable with Sm based on 2/3 Yield.

Table 6.3: Interpolated values:, Work hardened copper-, OFHC c10100 60% red

temp deg K	77	90	100	125	150	200	250	275	292
yield	374	369.	365.	356.	347.	328.	317.	312.	308.
ultimate	476.	466.	458.	439.	420.	383.	365.	356.	350.

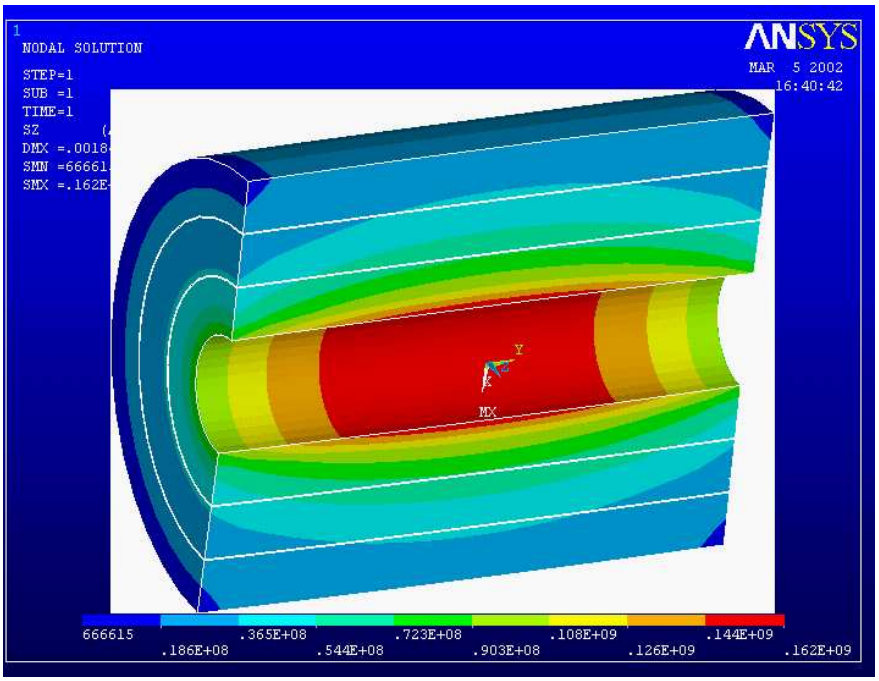

Figure 6.3: Hoop stress, all coil segments fully energized. The Von Mises stress plot is similar with a peak of 165 MPa, Tresca is 166 MPa.

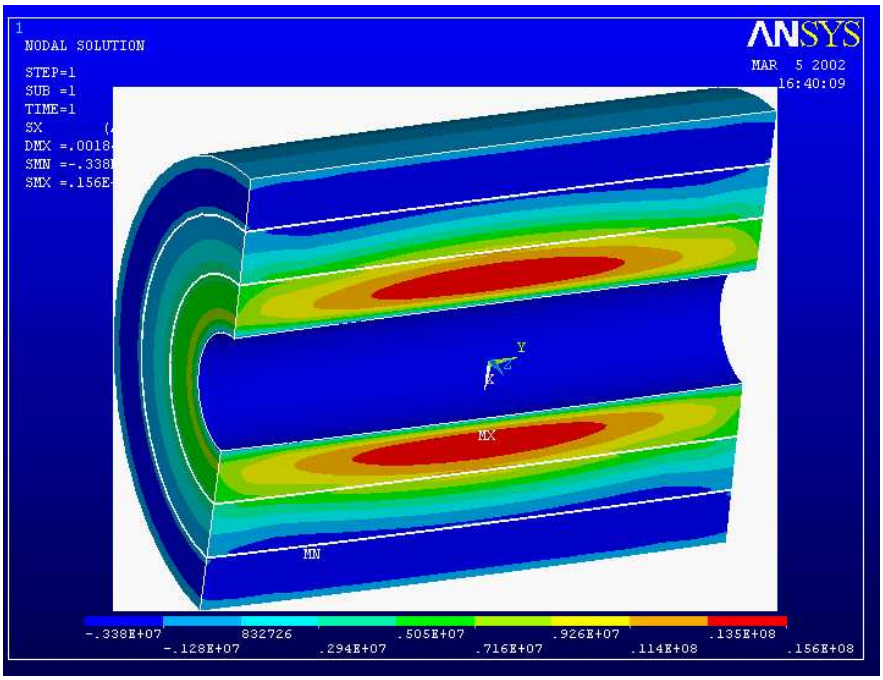

Figure 6.4: Radial tension stress, all coils fully energized. There is about an MPa of tension at the boundary between the first and second module. To avoid damage to the channel ligaments, a parting plane will be incorporated in the channel detail. This needs to occur in the ligament to retain thermal connection with the coolant in the channel.

If the highly cold-worked copper is chosen for the winding, the conductor allowable near the inside radius of the coil would be 365 MPa. The max stress in the three segment coil is 166 MPa. With this stress level, it is expected that half hard copper could be used, simplifying the winding process.

The three segment coil has three operational modes, two of which are structurally significant. The full performance configuration is limiting in terms of hoop stress and equivalent stress. It also has some radial stresses that will have to be mitigated with parting planes at the segment boundaries, or within the winding.

In the initial operating mode the outer coil segment is not energized. This induces some differential Lorentz forces and differential temperatures, that cause shear stresses between segments.

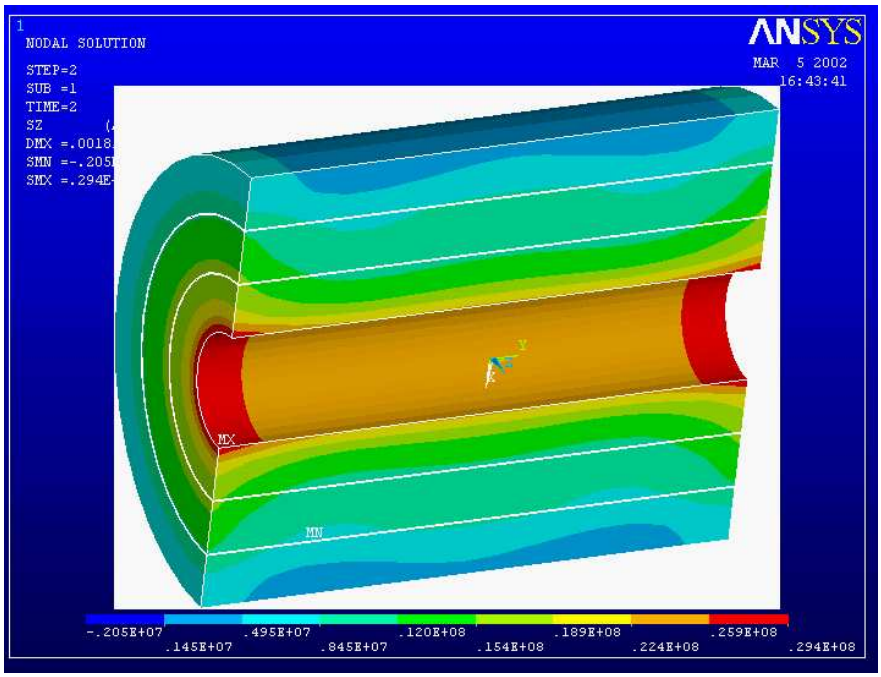

Figure 6.5: Hoop stress with only the inner two segments energized.

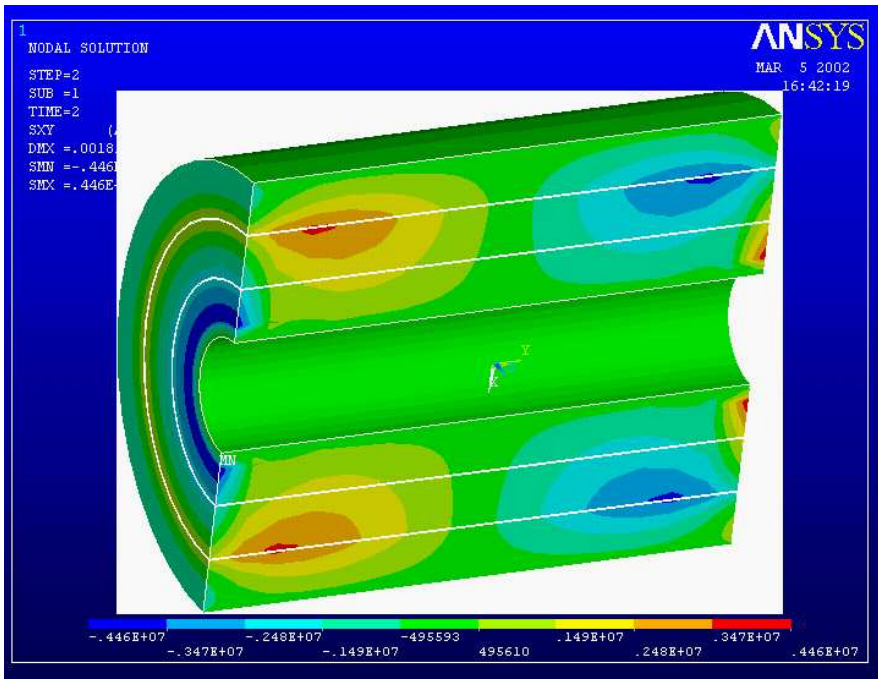

Figure 6.6: Smeared radial-axial stress with the inner two segments energized. This is a peak at the interface between the second and third modules. It must be carried across the thin ligaments between the channels, or relieved via a slip plane.

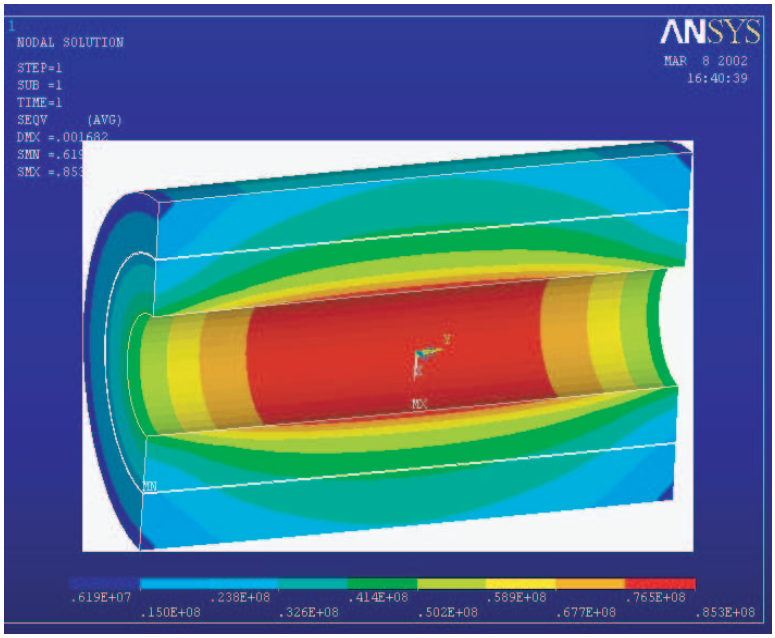

Figure 6.7: write caption

It may be desirable to build only the initial two inner segments and add the outer segment at a later time. The coil was analyzed with the outer segment removed, and the same current density in the other two segments. The max stress for this case is 85.3 MPa, which is a bit more than with the outer segment in place, but less than for the fully energized three segment coil. In all cases the stresses are lower than the expected allowable for the conductor. It is expected that the degree of cold work can be relaxed from the full hard condition. The final choice of the degree of cold work for the conductor will be determined during detailed design.

6.4 Cooldown Between Shots

Phased implementation of cooling systems is expected for the project. Within the coil, two cooldown methods are being investigated: and option using liquid nitrogen and an option which uses helium gas. It is expected that design of the magnet and cooling channels will allow either working fluid. Use of liquid nitrogen as the only coolant is contemplated for the initial operation

of the magnet. It is possible to use the container around the magnet as a vacuum vessel, and sub-cool liquid nitrogen to 66 K. Helium gas operation uses liquid nitrogen to cool the helium gas in a heat exchanger, and later allows use of liquid hydrogen to cool the helium and obtain improved fields and/or pulse lengths. The heat transfer characteristics of liquid nitrogen operation have only been conceptualized. Heat transfer calculations using gaseous helium will be presented here.

In the LN2 sub-cooling mode, about 50 cubic meter of nitrogen gas at standard temperature and pressure must be drawn off by the vacuum pump to lower both the magnet and the liquid nitrogen to the desired 66 K temperature.

6.5 Cooling Time with Helium Gas as a Working Fluid

The solenoid has groups of 6 to 8 layers of 1/2 inch square conductors separated by set of annular cooling channels. This could model any linear stack of .5 inch square conductors cooled from the ends of the stack whether layer wound - then there would be a layer of channels every sixth layer of conductor, - or pancake wound, where there would be radial channels every sixth pancake. The solution is a simple finite difference transient analysis. The ground wrap or cracked conductor/Kapton tape interfaces have not been modeled.

The insulation layer is modeled with five, and as a second option, three, 0.001" thicknesses of Kapton tape. The thermal conductivity of the tape is about 0.14 W/(m-K) at 100 K [1].

The surface heat transfer coefficient at the channels was taken as 170 W/m^2 for nitrogen gas at 100 K flowing at 40 m/s in a channel with a 2 cm hydraulic diameter [2]. The helium gas coefficient has been calculated from the Nusselt, Reynolds, and Prandle Numbers using the relation quoted in the Oak Ridge document [3], and will be verified during detailed design.

Typical results for 66 K He cooling, 0.1 kg/sec, 100 K end of pulse temperature 85 K target magnet start temperature. The cooldown time is 600 s to reach 85 K bulk temp, but not thermal equilibrium.

From $\dot{m} \times C_p \times \Delta T$ for a 20 deg inlet-outlet difference the cooldown time is about 950 s. The simulation with a finer time step ($\delta time = 0.0001$ rather

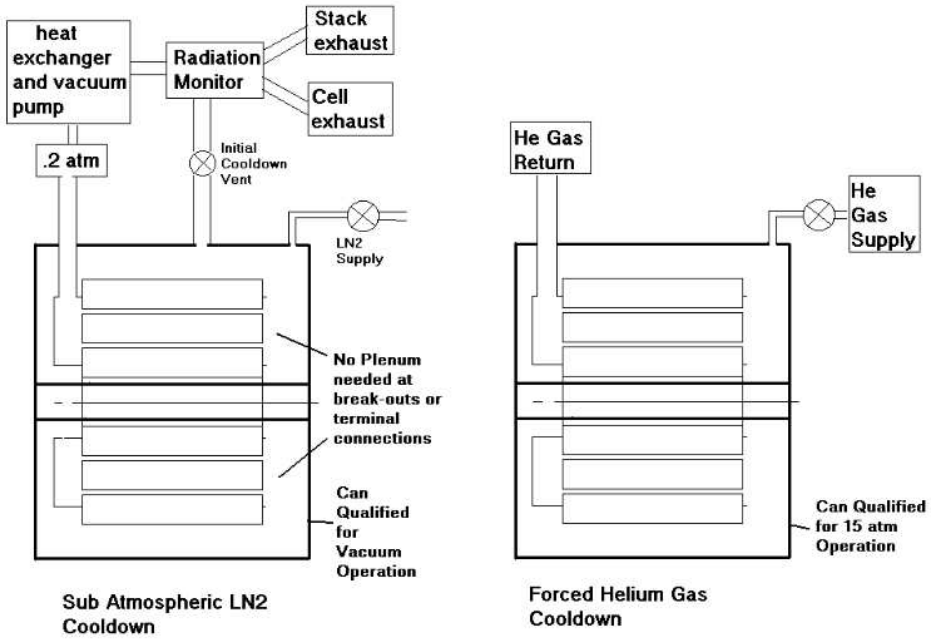

Figure 6.8: Proposed operational modes. The coil and can are designed for either cooling mode.

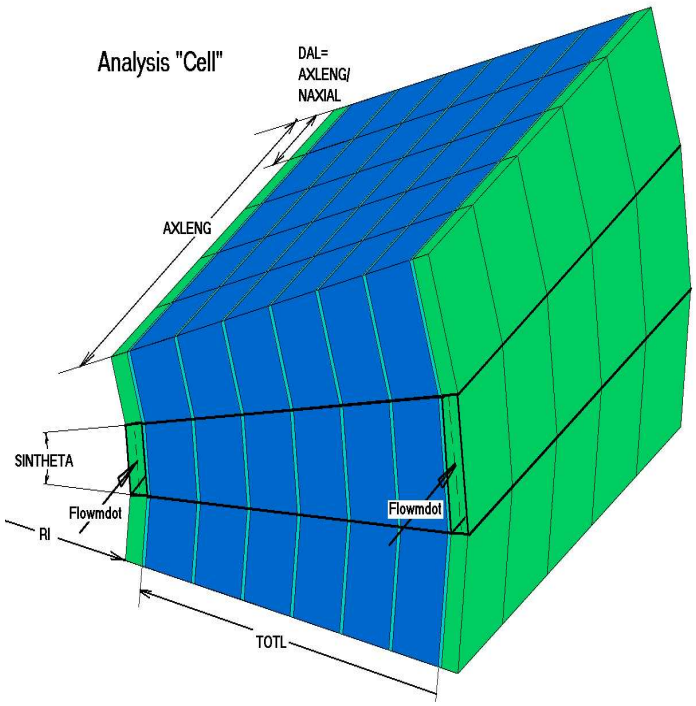

Figure 6.9: write caption

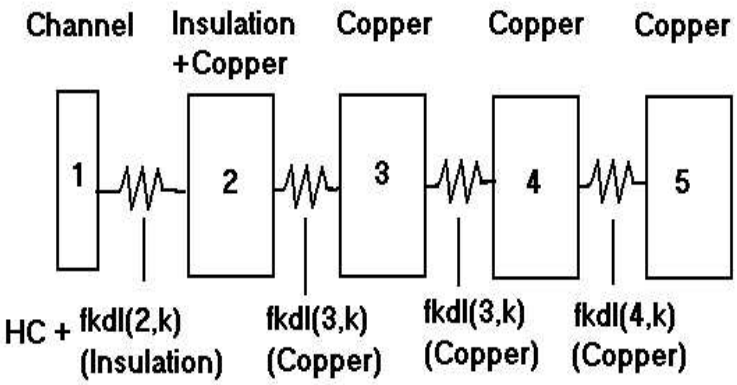

Figure 6.10: write caption

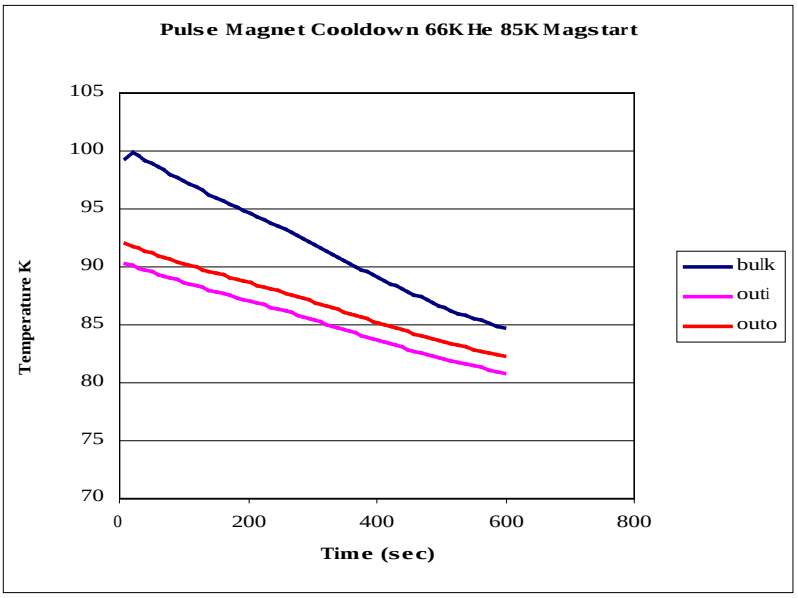

Figure 6.11: Temperature *vs.* time in seconds.

fact Muon Collaboration

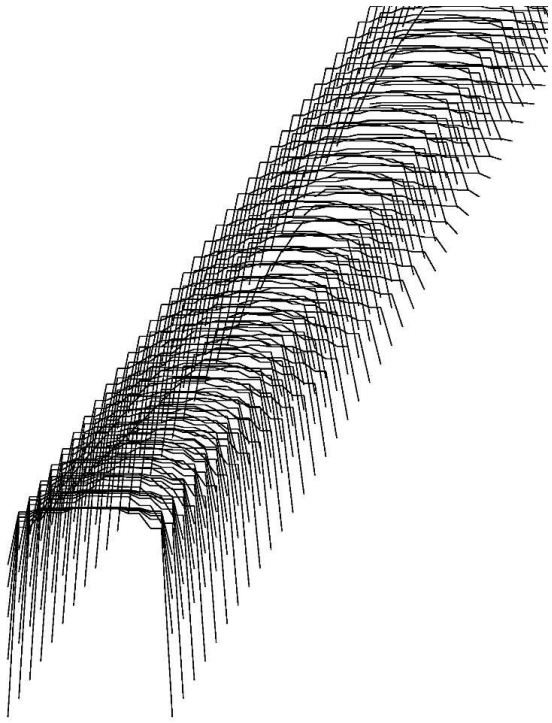

Figure 6.12: *Cell* temperature profiles. Time progresses towards the upper right. The groups of plots are temperature profiles for the five axial stations for which the temperature are calculated.

Table 6.4: Present Operational Scenarios

Case No.	Peak Field	T after pulse	T coolant	Start Bulk Temp	Guesstimated Time
1	5T	90K	66K	84K	200 s
2	10T	96K	66K	74K	800 s
3	15T	78K	22K	30K	1500 s

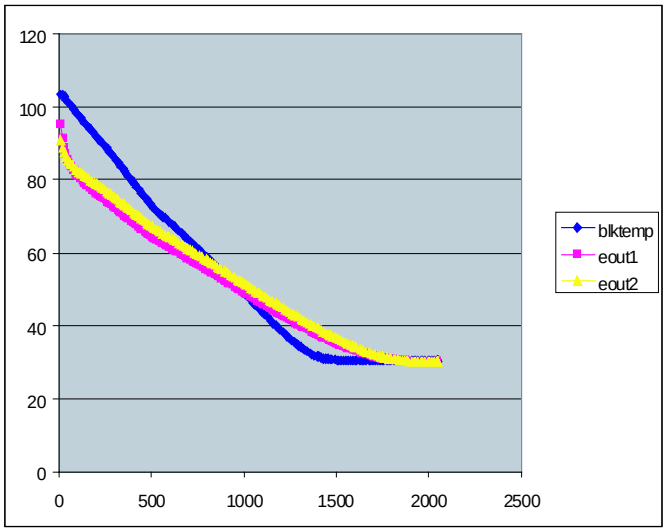

Figure 6.13: Temperature *vs.* time in seconds. Tout1 and Tout2 are outlet temperatures.

than 0.001) yields a 600 s cooldown . The inlet outlet ΔT ranges from 26 K to 16 K. The energy balance or difference between the conduction heat flux and the channel heat flux is good at the finer time step.

6.6 30 K Coolant, Cooldown from 100 K

Bulk temp is computed as the average temperature at mid axial build. It bottoms out before the down stream end. In the plot above, the channel outlet temperatures are better indicators of when the magnet reaches 30 K

Table 6.5: Parameters

Number of Atmospheres Operating Pressure	10
Enter Channel Height (mm)	2
$R_{i_{inner}}$	0.1000000
radial build	7.6200157×10^{-2}
inner coil start temp	100.0000
outer coil start temp	100.0000
inner coil radius	0.1000000
model cell energy (J)	1644.685 (100 to 85 K bulk)
model cell volume	5.5099601×10^{-5}
volume cpp	1989954.0
nlength	120
naxial	5
Mass flow rate	4.1666666×10^{-5} kg/s
Volume flow rate	5.5507730×10^{-6}
flow velocity	2.120239
Hydraulic Diameter	2.8944151×10^{-3} m
Velocity Head	1.721665 Pascal
Pressure Drop	31.46283 Pascal
Pressure Drop	3.1041747×10^{-4} Atmospheres
Helium density	7.506462 kg/m^3
Helium viscosity	2.6448268×10^{-7}
Prandl #	4.0756337×10^{-2}
Reynolds #	174174.1
Heat transfer coefficient	115984. 9

Table 6.6: Analysis to date: Time to target bulk temp from 100 K. $\frac{1}{2}$ inch Copper Conductor.

	T after pulse K	T coolant K	Cond. Layers	Time to 85 K s	Time to 30 K s
Equiv 5 Kapton 0.001 in wrap	100	66	6 layers	600	xxx
Equiv 5 Kapton 0.001 in wrap	100	66	8 layers	850	xxx
Equiv 3 Kapton 0.001 in wrap	100	66	8 layers	450	xxx
Equiv 5 kapton 0.0001 in wrap	100	30	6 Layers	2000	xxx

Bibliography

[1] Rule, Smith, and Sparks, *Thermal Conductivity of Polymide Film between 4.2 and 300K with and without Alumina Particles as Filler*, NISTIR #3948. August 1990.

[2] Oak Ridge CIT report # ORNL/FEDC-85-10 Dist. Category UC20 c,d October 1986.

[3] Excerpts from reference [2]

2.1.3 Convective Heat Transfer

It is important to estimate how much heat the superheated nitrogen gas ($T > 77\ K$) could absorb before exiting the cooling channel. The convective heat transfer coefficient, h, could be obtained from

$$h = \frac{KNu}{D_e} = \frac{0.023 R_e^{0.8} P_r^{0.4} K}{D_e}.$$

This coefficient is about 21×10^{-3} W/cm^{2}K at a vapor temperature of 200 K, vapor velocity of 40 m/s, and hydraulic diameter of 2 cm. It drops to 17×10^{-3} W/cm^{2}K at a vapor temperature of 100 K, keeping the mass flow rate constant. It is interesting to note that the heat transfer coefficient for film boiling at 200 K from Fig. 4 is about 12×10^{-3} W/cm^{2}K, which partially justifies the third assumption in Sec. 2.1.

6.7 Coil Package

6.8 Cryogenic System

6.9 Power Supply System

6.9.1 Experiment E951 Power Supply to Pulse a 14.5 T Solenoid Magnet

Introduction

The project goal is to pulse a magnet with 20 cm diameter bore, capable of a peak field near 15 T and a repetition rate of about 30 minutes.

Funding realities make it prudent to consider a stageable design with the following 3 cases

- The magnet achieves peak field of 5 T 84 K
- The magnet achieves peak field of 10 T 74 K
- The magnet achieves peak field of 14.5 T 30 K

Table 6.7: Parameters of Pulse Magnet System with 1 sec flat top

	Case 1	Case 2	Case 3
Outer radius (cm)	30.0	30.0	40.0
Copper mass (kg)	1943	1943	3644
Voltage (V)	150	300	300
Peak current (A)	3600	7200	7200
Field (T)	5.0	10.0	14.5
Inductance (mH)	138	138	436
Initial temperature (K)	84	74	30
Time t1, to end of flat tap (s)	8.2	7.3	16.3
Pulse length at tp (s)	11.1	10.1	24.1
Initial Resistance (mOhms)	30.2	23.5	11.0
Resistance at t1 (mOhms)	34.1	35.3	33.0
Resistance at tp (mOhms)	34.1	37.2	38.2
Dissipation at tp (mJ)	2.70	9.1	15.2

Cases 2 and 3 require the same power supply, but differ in the magnet cooling scheme.

From the power supply point of view, we will start with a 540 KVA power supply rated at 3600 A, ±150 V (Case 1)

To support case 1, and for cases 2 and 3 we will have four 540 KVA in series/parallel to generate 7200 A, ±300 V (Cases 2-3).

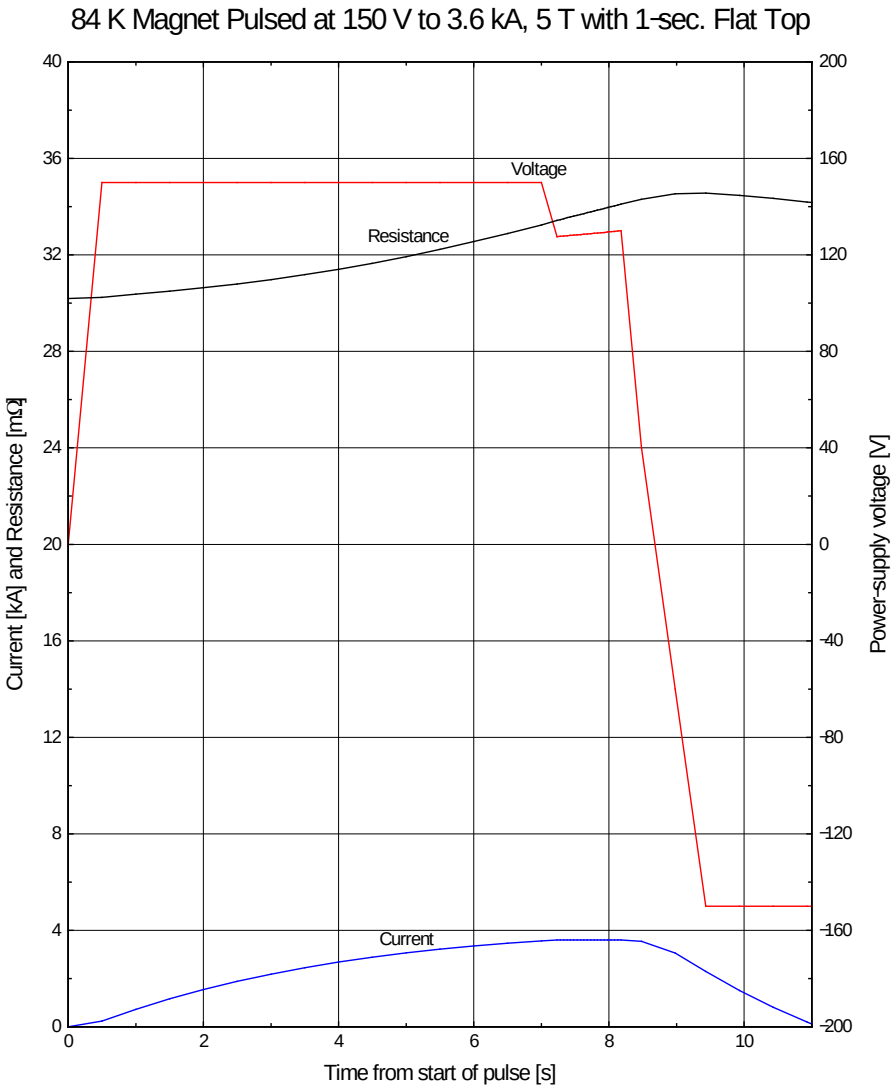

Figure 6.14: Performance of the 5 T magnet with the Case 1 power supply

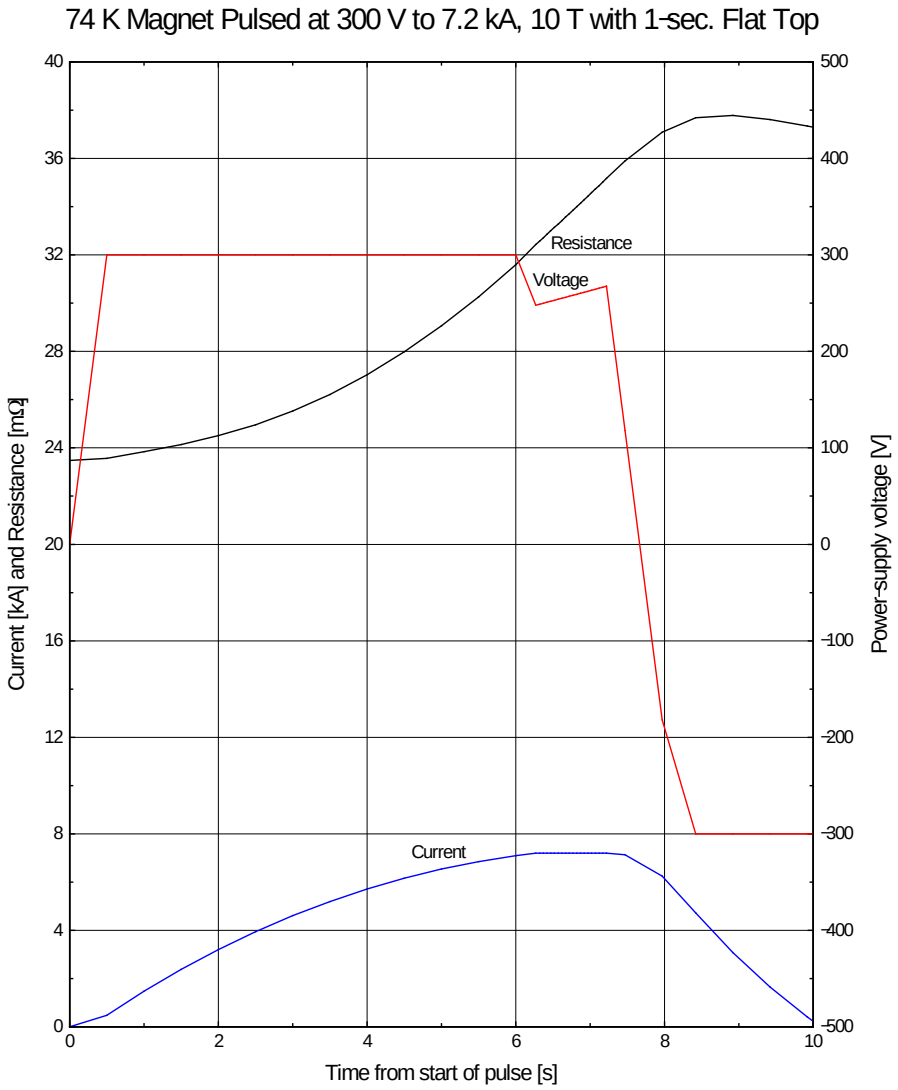

Figure 6.15: Performance of the 10 T magnet with the Case 2 power supply

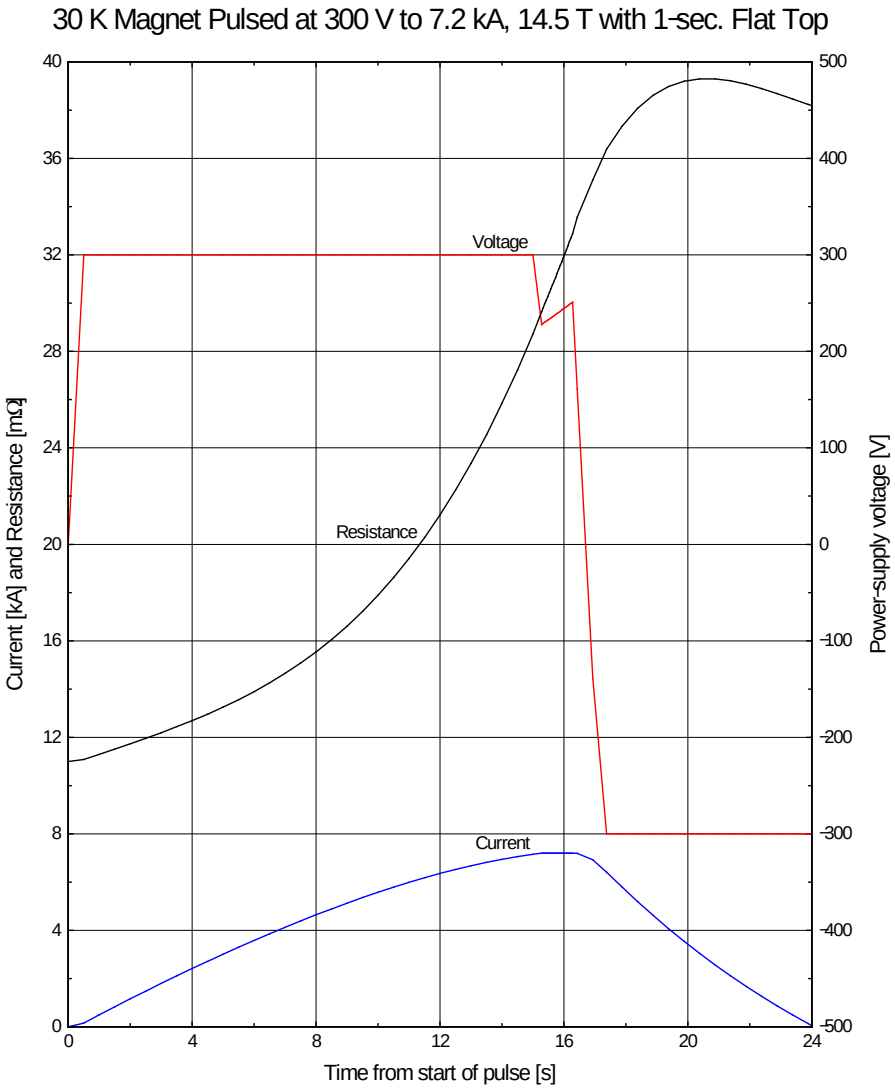

Figure 6.16: Performance of the 14.5 T magnet with the Case 3 power supply

The 540 KVA power supplies are thyristor-control six-pulse rectifiers, available at BNL from previous experiments.

These power supplies are presently configured as DC power supplies.

We need to modify their regulators to be able to pulse them.

The controls and interlocks of these power supplies must be updated.

Similar upgrades have been made during the Booster project with great success.

Case 1 power supply (5 T magnet)

This power supply will be a thyristor phase control power supply rated at 3600 A, ±150 V.

This power supply exists at Brookhaven from previous experiments.

The 3-phase, 480 V input power will be fed from an existing disconnect switch.

The power supply will have an AC circuit breaker.

A new regulator will be implemented based on the existing design for the AGS Main magnet power supply.

The power supply will be fully programmable from 0 to 3600 A.

It will have a voltage regulator as the inner loop and a current regulator as the outer loop.

Both voltage reference and the current reference will be generated from a high-level computer algorithm for a given magnetic field pulse and a given function of the load resistance as a function of current and time.

We need to replace the voltage feedback sensor with a LEM DCPT (DC potential transformer).

We need to replace the existing current sensor (shunt) with a LEM DCCT (DC current transformer).

These sensors have been successfully used in the past in various power supply systems.

All the old interlocks will be updated using an Allen Bradley Programmable Logic Controller (PLC).

This PLC will be programmed to make decisions on the interlocks and safely turn of the power supply if an interlock occurs.

The power supply will have the following interlocks:

- DC Over-current
- RMS magnet current interlock

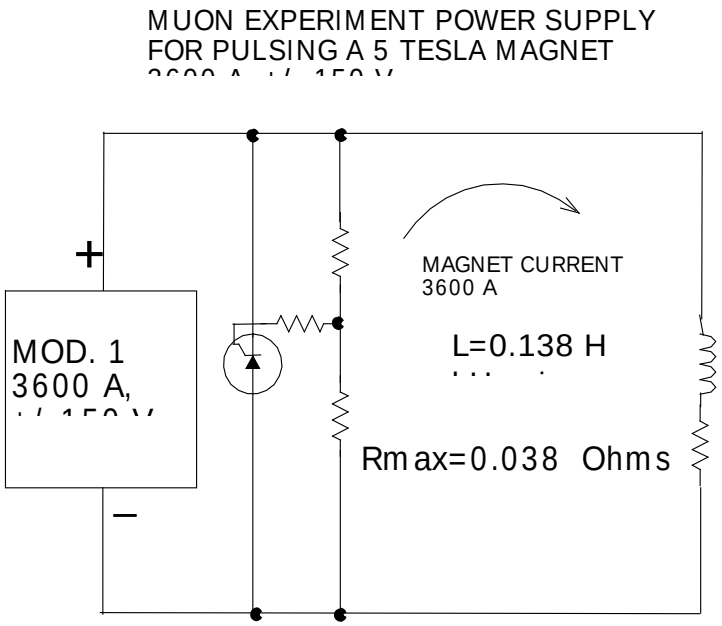

Figure 6.17: Need caption

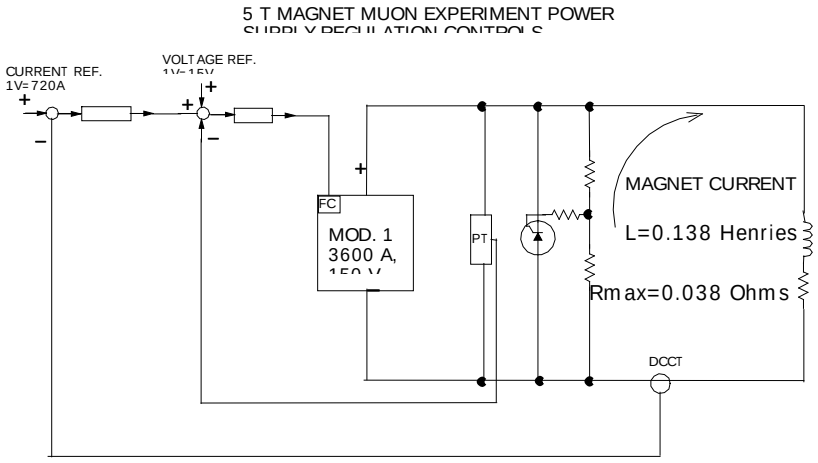

Figure 6.18: Need caption

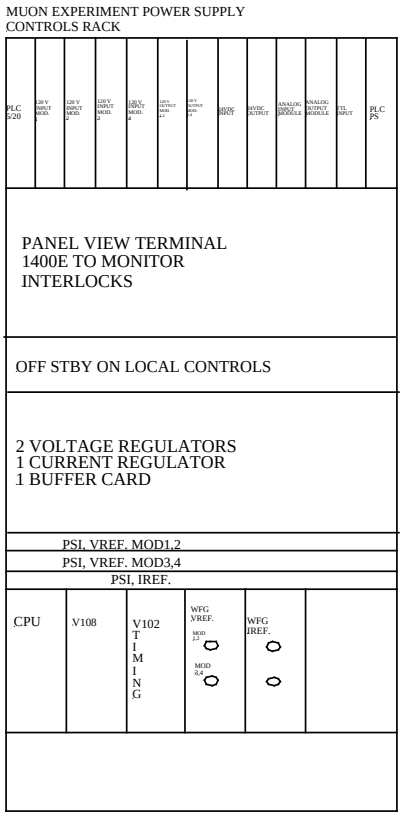

Figure 6.19: Need caption

- AC Over current
- Blower failure
- Ground Fault
- Magnet faults
- Magnet resistance interlock
- Cryo-interlocks

In case of any interlock failure, the power supply will be phased to 150 degrees in 100 ms.

This means the power supply voltage will be -150 V, the current then will go to zero in 3 s maximum time, depending where the interlock occurs in the cycle.

Then the AC circuit breaker will be commanded to open by the PLC regardless whether the magnet current is at zero or not.

A crowbar circuit based on self-triggering silicon control rectifiers (SCR's) will be implemented to short the magnet if the magnet voltage becomes greater than 350 V.

In this case, the magnet current will decay to zero with the L/R magnet time constant which is typically 3.6 s.

Note: L = 138 mH, $R_{\mathrm{max}} = 38\ m\Omega$. Minimum repetition rate is 5 minutes

Case 2-3 power supply (10, 14.5 T magnet)

This power supply will be a thyristor phase control power supply composed of 4 series/parallel Case-1 power supplies. It will be rated at 7200 A, ±300 V.

These power supplies exists at Brookhaven from previous experiments and will be modified as described in Case 1.

The 3-phase, 480 V input power will be fed from existing disconnect switches.

The power supply will have four AC circuit breakers, one per power supply.

Two parallel power supplies (MOD 1 and MOD 2) will be fed from the same existing substation and the other two (MOD 3 and MOD 4) from a different existing substation. This will not require any modifications to our existing substations regarding power supply input power requirements.

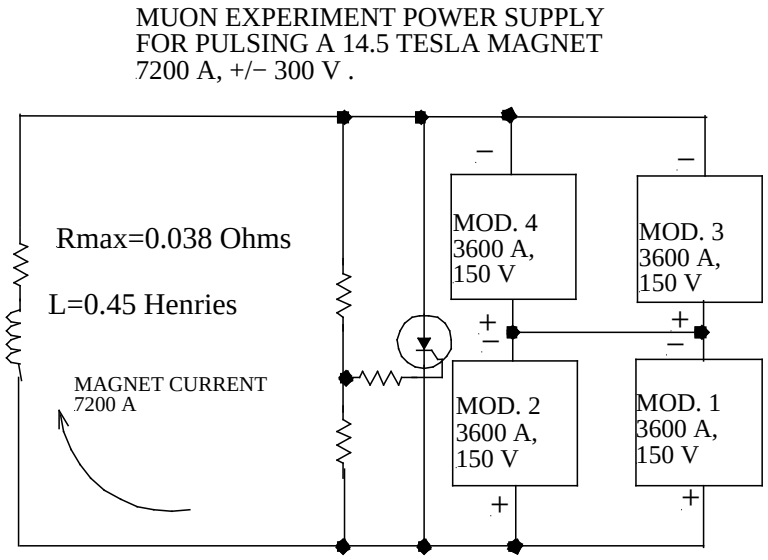

Figure 6.20: Case 2-3 power supply (10, 14.5 T magnet)

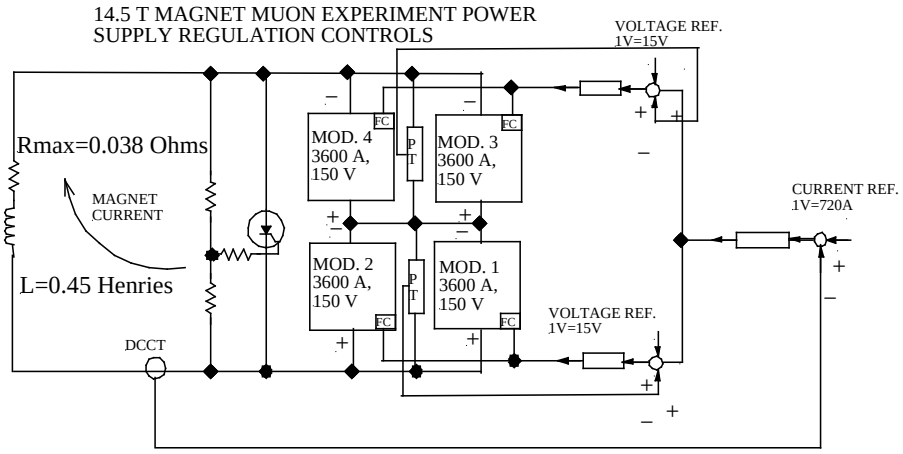

Figure 6.21: Case 2-3 power supply (10, 14.5 T magnet)

The power supply will be fully programmable from 0 to 7200 A.

It will have two voltage regulators as the inner loops and a current regulator as the outer loop.

Note: For Case 2, L = 0.138 H, $R_{\max} = 38\ m\Omega$, for Case 3, $L = 0.436\ H$, $R_{\max} = 37\ m\Omega$.

In order to share current properly between parallel power supplies, we intend to run 2-in water-cooled busses from the + terminal of MOD 2 to the magnet and from the + terminal of MOD 1 to the magnet. The same is true for the - terminal of MOD 4 and MOD 3.

The anticipated overall bus resistance should not exceed 2 $m\Omega$.

A crowbar circuit based on self-triggering silicon control rectifiers (SCR's) will be implemented to short the magnet if the magnet voltage becomes greater than 350 V.

In this case, the magnet current will decay to 0 A with the L/R magnet time constant which is typically 3.6 s for Case 2 magnet, 12 s for Case 3 magnet.

All the old interlocks will be the same as Case 1 power supply and will be updated using an Allen Bradley Programmable Logic Controller (PLC).

Minimum repetition rate for case 2 magnet is 20 minutes, for case 3 magnet 30 minutes.

Table 6.8: Schedule

Muon Power Supply Schedule (1-29-02)			
Quarters	Design & Development	Fabrication	Installation/Commissioning
1	Design for Case 1	Procurement	
2		Fabrication of Case 1	
3			Installation of Case 1
4			Commissioning of Case 1
5	Design for Case 2,3		
6		Fabrication of Case 2,3	
7			Installation of Case 2,3
8			Commissioning of Case 2,3

The Case 1 power supply should be compete by the end of the 4rd quarter, middle of FY03.

The Case 2-3 power supply should be complete by the end of the 8th quarter, middle of FY04.

This schedule is spread apart over 2 years, taking into account other projects of the C-AD Power Supply Group.

All the parts purchased should be bought at the same time for the following reasons:

- We need almost all the parts for the controls rack for Case-1 power supply.
- The DC bus should be bought at the same time to save money.

Cost estimate

Table 6.9 includes burden of 87% on labor and burden of 47% on materials.

fact Muon Collaboration

Table 6.9: Cost Estimate

Muon Power Supplies				Duration (man days)			
Description	$ Labor	$ DTS	$ Purch	Engr	Dsgn	Tech	$ DTS
MUON PS - 1 Design & Development	33469						
Case 1 PS 3600 A, ±150 V	19461	0	0	13	8	4	0
Case 2,3 PS 7200 A, ±300 V	14008	0	0	8	8	3	0
Muon PS - 2 Fabrication	82353	145383					
Case 1 PS 3600 A, ±150 V	45369		145383	31	0	25	0
Case 2,3 PS 7200 A, ±300 V	36983		0	15	0	33	0
Muon PS - 3 Installation	84116	4034					
Case 1 PS 3600 A, ±150 V	29557	1008	0	10	0	29	1.5
Case 2,3 PS 7200 A, ±300 V	54558	3026	0	15	0	57	5
AMOUNT FOR CASE 1	94388	1008	145383				
TOTAL CASE 1	240780						
TOTAL WITH 20% CONTINGENCY	288936						
AMOUNT FOR CASES 2,3	105550	3026	0				
TOTAL CASES 2,3	108575						
TOTAL WITH 20% CONTINGENCY	130290						
TOTAL AMOUNT	199938	4034	145383				
TOTAL NO CONTINGENCY	349355						
TOTAL WITH 20% CONTINGENCY	419226						

6.10 Environment, Safety and Health Considerations

fact
Muon Collaboration

Chapter 7

Cost and Schedule

fact
Muon Collaboration

Chapter 8

R & D Plans